Title
Investigating the Ground State of Organic Frustrated Magnets using Nuclear Magnetic Resonance

Author
Le, Teresa H.

Publication Date
2023

Peer reviewed|Thesis/dissertation

UNIVERSITY OF CALIFORNIA
Los Angeles

Investigating the Ground State of Organic Frustrated Magnets using Nuclear Magnetic Resonance

A dissertation submitted in partial satisfaction
of the requirements for the degree
Doctor of Philosophy in Physics

by

Teresa H. Le

2023

ABSTRACT OF THE DISSERTATION

Investigating the Ground State of Organic Frustrated Magnets using Nuclear Magnetic Resonance

by

Teresa H. Le
Doctor of Philosophy in Physics
University of California, Los Angeles, 2023
Professor Stuart Brown, Chair

Quantum Spin Liquids (QSLs) are novel, exotic states of matter that have been proposed to be the key to topological quantum computing and high temperature superconductivity. The QSL is defined, in theory, to be a nonmagnetic insulator with quantum disordered, highly entangled spins. Unfortunately, the connection between theory and experiment in this field is still incomplete. While lack of magnetic order is easy to detect experimentally, quantum disorder and long range entanglement are more difficult to prove. Consequently, there are many candidate QSL materials, but there are no undisputed QSLs to date. This dissertation investigates the first quasi-2D QSL candidate ever to be discovered, κ-(BEDT-TTF)$_2$Cu$_2$(CN)$_3$, and its cousins, κ-(BEDT-TTF)$_2$Hg(SCN)$_2$Cl, and κ-(BEDT-TTF)$_2$Hg(SCN)$_2$Br, through the lens of Nuclear Magnetic Resonance (NMR) in an attempt to answer some of the outstanding questions still present almost 20 years after the discovery of κ-(BEDT-TTF)$_2$Cu$_2$(CN)$_3$. First, the effects of charge degrees of freedom on the ground state of κ-(BEDT-TTF)$_2X$ materials are examined via the study of κ-(BEDT-TTF)$_2$Hg(SCN)$_2$Cl and κ-(BEDT-TTF)$_2$Hg(SCN)$_2$Br, both of which are more likely to be charge ordered than κ-(BEDT-TTF)$_2$Cu$_2$(CN)$_3$. Then, the question of whether or not the NMR signature of κ-(BEDT-TTF)$_2$Cu$_2$(CN)$_3$ is compatible with a spinon fermi surface and the nature of the "6 K anomaly" in κ-(BEDT-TTF)$_2$Cu$_2$(CN)$_3$ is revisited via low tem-

perature, high field NMR. In the case of κ-(BEDT-TTF)$_2$Hg(SCN)$_2$Cl, it is found that impurity spins dominate the low temperature NMR relaxation signature masking the intrinsic behavior. The $1/T_1$ relaxation of κ-(BEDT-TTF)$_2$Hg(SCN)$_2$Cl is very similar to that of κ-(BEDT-TTF)$_2$Cu$_2$(CN)$_3$, and it is reasonable to believe the same "masking" may apply in the latter case. κ-(BEDT-TTF)$_2$Hg(SCN)$_2$Br, on the other hand, behaves quite differently from the other two. While none of the materials studied exhibit any signs of long range magnetic order, signatures for short range magnetic order were detected in κ-(BEDT-TTF)$_2$Hg(SCN)$_2$Br. κ-(BEDT-TTF)$_2$Cu$_2$(CN)$_3$ is revisited at high fields in order to test the theory that impurity spins mask intrinsic relaxation behavior, as NMR signatures from impurities should be frozen out at sufficiently high fields. The relaxation signature of κ-(BEDT-TTF)$_2$Cu$_2$(CN)$_3$ is found to be gapped, inconsistent with a spinon fermi surface. The nature of this gap remains unclear. Some exploration into the Inverse Laplace Transform (ILT) method as a tool for analyzing the stretched exponential in the context of κ-(BEDT-TTF)$_2$Cu$_2$(CN)$_3$ is discussed as well.

The dissertation of Teresa H. Le is approved.

Hong-Wen Jiang

Karoly Holczer

Christopher Gutierrez

Stuart Brown, Committee Chair

University of California, Los Angeles

2023

To my boyfriend and my therapist ...

who both pushed me to continue forward

and who recognized my talents

when I, myself, could not.

And to my advisor ...

for his patience and understanding.

TABLE OF CONTENTS

List of Figures . . . . . **ix**

List of Tables . . . . . **xv**

Acknowledgments . . . . . **xvi**

Vita . . . . . **xvii**

1 Motivation and Background **1**

1.1 Motivation 1

1.2 Quantum Spin Liquid Theory 2

1.2.1 What is a Quantum Spin Liquid? 2

1.2.2 Relevant Hamiltonians 4

1.2.3 Classification of QSLs 6

1.2.4 QSL Models on a Triangular Lattice 9

1.3 Properties of κ-(BEDT-TTF)$_2X$ 13

1.3.1 Crystal Structure 13

1.3.2 Band Structure 14

1.3.3 The ET Molecule and its HOMO 16

1.3.4 The Effects of Disorder 18

1.3.5 Comparison of X = CuCN, HgCl, HgBr 19

2 Experimental Methods **24**

2.1 Theory of Spin Dynamics 24

2.1.1 Uniform Magnetic Fields and Larmor Precession 24

2.1.2 Macroscopic Spin Picture and Thermal Equilibrium 26
2.1.3 Rotating Field and Rabi Oscillations 27
2.1.4 The Bloch Equations and Relaxation 28
2.2 Dominant Interactions 29
2.2.1 Dipolar Coupling 30
2.2.2 Hyperfine Coupling 31
2.3 Pulsed NMR Spectroscopy 32
2.3.1 Technique 32
2.3.2 NMR Spectrum 32
2.3.3 T_1 Measurements 33
2.3.4 T_2 Measurements 34
2.4 Experimental Setup 34

3 Effects of Impurity Spins on Low-T Behavior of κ-HgCl 37
3.1 Methods 38
3.2 NMR Spectra 39
3.3 Spin-Lattice Relaxation 40
3.3.1 $1/T_1T$ vs T 40
3.3.2 $1/T_1$ vs T 41
3.4 Comparison with other κ-$(ET)_2X$ 43
3.5 Conclusion 47

4 Slowing Spin Dynamics in κ-HgBr 48
4.1 Methods 49
4.2 Spin-Lattice Relaxation 50

4.3 NMR Spectra . . . 51
4.4 Spin-Spin Relaxation . . . 53
4.5 On the NMR Collective Behavior . . . 53
4.6 Discussion . . . 56
4.7 Conclusion . . . 57

5 Searching for a Gap in κ-CuCN . . . 59
5.1 Methods . . . 61
5.2 Results . . . 62
5.3 Analysis of T_1 Distributions . . . 66
5.3.1 Comparison of ILT and Johnston Distributions . . . 67
5.3.2 Analysis of ILT Distributions . . . 68
5.4 Discussion/Conclusion . . . 72

A Examination of ILT Method . . . 74
A.1 Method . . . 74
A.2 Choosing Alpha . . . 76
A.3 Effectiveness at Finding Distributions . . . 77
A.3.1 Complete Recovery . . . 77
A.3.2 Incomplete Recovery and Late Acquisitions . . . 79
A.3.3 Incomplete Saturation . . . 80
A.3.4 The Effect of Noise . . . 81
A.3.5 Conclusion . . . 82

LIST OF FIGURES

1.1 (a) Illustration of a Valence Bond Solid state. (b) The QSL is a superposition of all possible valence bond pairings in a lattice. Adapted from Reference [14]. . . 4

1.2 (a) Triangular lattice with 120^o Néel state ordering. (b) Kagome lattice with the same order. Adapted from Reference [14]. 5

1.3 Intra-chain interaction J_1 vs Inter-chain interaction J_1'. 9

1.4 Four-site rhombus plaquette on a triangular lattice with arrows indicating the direction in which spins would be swapped by the P_{1234} operator. 11

1.5 (a) Layered structure of κ-(BEDT-TTF)$_2X$ salts. (b) Within the conduction layer, dimers sit on a triangular lattice with varying degrees of dimerization. (c) Molecular structure of ET molecule with central carbons replaced by ^{13}C. . . . 14

1.6 (a) Generic quasi-2D band structure of a κ-(ET)$_2X$ crystal in the metallic phase, calculated via tight binding methods. (b) Fermi surface associated with energy dispersion in (a). Figure adapted from Ref [36]. 15

1.7 (a) Generic band structure of a κ-(ET)$_2X$ crystal in the insulating phase, calculated via tight binding methods. Figure from Ref [36]. 16

1.8 Molecular structure of BEDT-TTF, reused to show the important parts of the molecule. Red box is the center tetrathiafulvalene (TTF) while the blue boxes are the ethylenedithio (EDT) molecules. 17

1.9 (a) Highest occupied molecular orbital (HOMO) of a neutral ET atom. Figure taken from Ref [40]. 18

1.10 Comparison of eclipsed vs. staggered ET molecules. Figure from [43]. 18

1.11 Examples of 6K anomaly in measurements of κ-CuCN with red arrow pointing at anomaly. (a) ^{13}C $1/T_1$ [51]. (b) Susceptiility [11]. (c) Thermal conductivity [50] 21

2.1 Larmor Precession of spin magnetic moment about a field. 25

2.2 Random orientation of spins in a solid. 26

2.3 Trajectory of magnetization after perturbation. 29

2.4 (a) Schematic of a Pulsed NMR Experiment. Figure from [64]. 35

3.1 (a) Illustration of layered structure along the a axis of κ-(BEDT-TTF)$_2$Hg(SCN)$_2$Cl. Alternating layers of (BEDT-TTF)$_2^+$ molecules (grayscale) stacked side by side and [Hg(SCN)$_2$Cl]$^-$ anion sheets (blue). (b) Along the b/c conducting plane, BEDT-TTF molecules form a triangular lattice. Important transfer integrals, t, are marked for reference. 38

3.2 (a) Temperature dependence of ^{1}H NMR spectra for sample 1. Spectra above 2 K were obtained in a ^{4}He cryostat while temperatures below 2 K were obtained in the dilution refrigerator. A small difference in crystal orientation between setups is expected. (b) The frequency of the four resolved peaks (colored open shapes) is tracked across different angles. 39

3.3 Temperature dependence of ^{1} H NMR spectra for κ-(BEDT-TTF)$_2$Cu[N(CN)$_2$]Cl. Very obvious splitting of the lineshape upon transition into an AFM state is seen between 27 K and 25 K. Figure borrowed from [65]. 40

3.4 $1/T_1T$ measurements for sample 1 vs. temperature. 41

3.5 (a) $1/T_1$ measurements for sample 1 vs. temperature plotted on a log-log scale. Inlet, as well as red distribution map, plots the stretched exponential constant, α, across temperature. (b) $1/T_1$ plotted against $1/T$ on a log-lin scale to show partial Arrhenius behavior below 5 K. (c) Field dependence of $1/T_1$ in the temperature range about the peak. Field dependent measurements were performed on sample 2. 42

3.6 The absolute values of the spin susceptibility of κ-(BEDT-TTF)$_2$Cu[N(CN)$_2$]Cl (determined by EPR measurements in Ref. [58]) was approximated by χ_{mol} of κ-(BEDT-TTF)$_2$Cu$_2$(CN)$_3$ [11]. 44

3.7 (a) ^{1}H $1/T_1$ data in the insulating state of κ-HgCl plotted alongside paradigmatic QSL candidates κ-CuCN and κ-AgCN. Here, $1/T_1$ in the shaded region follows a field-independent approximately linear T dependence suggesting that this is the intrinsic response with $J/k_B \approx 200$ K. (b)–(d) While peaked at different $T_{\max}$, the low-temperature contribution exhibits a similar suppression with higher B_o for all three compounds; ^{13}C data (scaled by γ_n) match well with the ^{1}H results acquired at the same B_o [11, 51, 67]. A similar field-dependent contribution is observed in high-frequency susceptibility data plotted as χT (inset of (b) at 9.37 GHz [58]; inset of (c) at 16.5 GHz [68]). 45

4.1 (a) Layered structure of κ-HgBr, identical to that of κ-HgCl. (b) Intralayer arrangement of cations in the bc plane with the respective transfer integrals, as indicated. While the left side depicts a strongly dimerized structure ($t_d \gg t, t'$), giving rise to Mott-insulating behavior, weakly bound dimers (right) pronounce intersite Coulomb interaction, with a tendency to charge order. Charge-rich and -poor molecules are distinguished by light and dark colors, respectively. (c) The two central carbon atoms of BEDT-TTF have been spin labeled by ^{13}C for NMR investigations. 50

4.2 (a) The spin lattice relaxation rate, acquired at 6.5 T and 9.5 T, as a function of temperature. At higher temperatures, the pulse excitations are non-selective. However, a result of large inhomogeneous line widths and a fixed spectrometer bandwidth, the results below 40 K correspond only to the center of the spectrum. (b) The maximum in T_1^{-1} is highlighted on a logarithmic scale. (c) $(T_1T)^{-1}$ emphasizes the metal-insulator transition at $T_{\rm MI} = 90$ K. 51

4.3 (a) Temperature-dependent evolution of ^{13}C NMR spectra at 9.5 T (101.660 MHz). (b) Due to excessive line broadening, the spectra below 39 K were acquired via magnetic field sweeps. The 39 K spectrum from single field acquisition is included for comparison. (c) Full width half maximum (FWHM) of the 9.5 T spectra as a function of temperature. FWHM were obtained from the entire, broad spectrum. Inset: Field dependence at 2 K of FWHM. 52

4.4 $1/T_2$ between 2.5 K and 110 K. $1/T_2$ was determined by a measure of the echo decau on varying the pulse separation. At higher temperatures, the pulse excitations are nonselective. However, as a result of large inhomogenous line widths and a fixed spectrometer bandwidth, the results below 40 K corrrespond only to the center of the spectrum. 53

4.5 Chart of the proposed charge, spin, and structural degrees of freedom for κ-HgBr versus temperature upon cooling. 55

5.1 (a) Spin susceptibility extracted from the EPR spectra by Miksch *et al.* [54] shows one gapped component and a defect component which creeps in at the lower temperatures. 60

5.2 BEDT-TTF pair with the inner and outer ^{13}C atoms labeled. 62

5.3 Temperature dependence of NMR spectra across four different fields. Asterisk implies spectrum obtained via frequency sweep. Sudden shifts at frequency swept temperatures likely systematic error due to field discrepancies. 6 T Inset: Spectral intensity * T vs T. 30 T Inset: Comparison of field swept spectrum and single acquisition at 4 K. 63

5.4 Standard deviation (STD, σ) of NMR spectra calculated from square root of the second moment. 64

5.5 (a) $1/T_1$ vs. T from stretched exponential fits to saturation-recovery curves plotted alongside results from Shimizu *et al.* [51]. For temperatures above $\sim$ 4.5 K, T_1 is unbiased, otherwise T_1 is measured from center of spectra due to excess linewidth. (b) Variation of the stretching exponent, β, across temperature. (c) A closer look around the peaks in $1/T_1$ that appear right before a significant fall off. 65

5.6 Distribution of $1/T_1$ in the ^{13}C NMR relaxation determined via ILT (solid lines) and the Johnston model (dashed lines) plotted across 6.7 T, 12 T, 20 T, and 30 T. $P(1/T_1)$ has been normalized so that $\sum P(1/T_1) = 1$. 67

5.7 Distribution of $1/T_1$ in the ^{13}C NMR relaxation determined via ILT (solid lines) and the Gaussian fit of its compnents (dashed lines) plotted across 6.7 T, 12 T, 20 T, and 30 T. $P(1/T_1)$ has been normalized so that $\sum P(1/T_1)\Delta(1/T_1) = 1$. . 69

5.8 $1/T_1$ as determined by an ILT fit to saturation-recovery curves. Solid circles represent the faster relaxing component while squares represent the slower one. For comparison, the stretched exponential fits are plotted as dashed lines. An Arrhenius fit over all fields estimates a gap size of 16.7 K. Inset: 20 T relaxation is plotted to highlight the general behavior, per field, of the two components. . . 70

5.9 ILT fits of simulated pure stretched recoveries, which normally do not have any bumps or kinks. The parameters of the recovery curves are $\beta = 0.5$, $1/T_1 = 1$, $S/N = 35$, and $\alpha = 3$ was used in the ILT fit. 71

A.1 ILT fits for a simulated recovery curve with $T_1 = 1$, Signal to Noise = 100, $\alpha = 0.5$ (blue) and $\alpha = 5$ (orange). 76

A.2 (a) ILT fit of κ-CuCN 12 T relaxation using optimal α values (b) Optimal alpha values for 12 T. 77

A.3 (a) ILT fit to several stretched exponential recoveries with varying $1/T_1$ and β values. (b) The simulated stretched exponential (open circles) plotted alongside the calculated recovery curve from the ILT fit (solid line). 78

A.4 ILT fit to several two-component recoveries with varying $1/T_1$ and amplitudes. . 78

A.5 (a) Generated stretched exponential curves with $\beta = 1$ and $1/T_1 = 1$. Blue is a complete recovery, orange is slightly incomplete at the top, and yellow is extremely incomplete. (b) ILT fit results on generated stretched exponentials. The fit for the incomplete recovery shows a tail which is not present when the ILT is given the full curve, and a greatly overestimated $1/T_1$ in the extreme case. 79

A.6 (a) Generated stretched exponential curves with $\beta = 1$ and $1/T_1 = 1$. Blue is a complete recovery, orange is incomplete at the bottom, and yellow is extremely incomplete (b) ILT fit results on generated stretched exponentials. The fit for the incomplete recovery shows a constant artifact on the right only in the extreme case. 80

A.7 (a) A recovery curve with incomplete saturation (orange) and the same curve shifted and normalized so that the first point starts at 0 and the last point ends at 1 (blue). (b) ILT fit for the two recoveries in plotted (a). 81

A.8 (a) Generated stretched exponentials with $\beta = 0.3$ and $T_1 = 1$ with varying levels of signal to noise. (b) ILT fit to the stretched exponentials in (a) using the calculated α_{opt} as the smoothing factor. 82

LIST OF TABLES

3.1 Impurity spin densities for $\kappa-$(BEDT-TTF)$_2$Hg(SCN)$_2$, κ-(BEDT-TTF)$_2$Cu(CN)$_3$ [31], and κ-(BEDT-TTF)$_2$Ag$_2$(CN)$_3$. 46

4.1 Comparison of ^{13}C NMR quantities for κ-HgBr, κ-CuCN and κ-AgCN [51, 67]. $1/T_2$ and FWHM are the $T \to 0$ saturated values for $B \simeq 8$ T for κ-CuCN and κ-AgCN. 57

ACKNOWLEDGMENTS

I could not have earned this achievement without the kind support of the brilliant individuals I met along my Ph.D. journey. First, I want to thank my parents for doing what they had to do to get to the United States. Without them, I would not have had the privilege of being born American and receiving the education that I did. I recognize that, and will forever be grateful. I thank my sister for being my struggle buddy as we simultaneously scrambled through our respective disciplines. I thank the Physics and Astronomy staff members, Ernie, Cameron, and Brad, for being my friends in an environment where friends are difficult to come by. In the same regard, I am grateful to my past labmates, Aaron, Austin, and Andrej for the fun conversations we had over the years and Prof. Holczer for the patio watermelons. Although this list is getting too long, I have to thank my boyfriend and therapist for encouraging me to push forward when it was clear the only thing stopping me was myself. The biggest thank you of them all, however, goes to my PI, Stuart Brown. I know you did everything you could to support me and enable me to succeed. When all 24 hours of the day were booked, you created a 25th. Thank you for making time for me. Thank you everyone for the memories, experiences, and lessons learned over the past several years. I will take all of it with me as I enter the next chapter of my life and career. Oh, and because I'm required to do this: chapters 3 and 4 are versions of [1] and [2], respectively.

VITA

2015	B.S. (Physics), University of California, Davis.
2017	M.S. (Physics), UCLA, Los Angeles, California.
2016-2022	Teaching Assistant, UCLA, Los Angeles California

PUBLICATIONS

T. Le, A. Pustogow, J. Wang, A. Henderson, T. Siegrist, J. A. Schlueter, and S. E. Brown (2020). Disorder and slowing magnetic dynamics in κ-(BEDT-TTF)$_2$Hg(SCN)$_2$Br. Phys. Rev. B 102, 184417

A. Pustogow, T. Le, H.-H. Wang, Yongkang Luo, E. Gati, H. Schubert, M. Lang, and S. E. Brown (2019). Impurity moments conceal low-energy relaxation of quantum spin liquids. Phys. Rev. B 101, 140401(R).

CHAPTER 1

Motivation and Background

1.1 Motivation

Low dimensional magnetism remains an active field of study in condensed matter physics due to its complexity and the promise of novel quantum phenomena such as the fractional quantum hall effect and Kondo effect. However, solving for the ground state of a system of interacting, near-neighbor (NN) antiferromagnetic (AFM) spins is surprisingly difficult. While the AFM Ising and Heisenberg Hamiltonians (to be discussed in section 1.2.2) were solved exactly for 1D chains in the early 1900s [3, 4], for a very long time, theorists were unable to solve for the ground states of 2D systems, as many solutions required the help of numerical methods which were not available at the time. The 2D, isotropic triangular lattice was one of those systems. The NN AFM Ising model was solved by Wannier in 1950, who determined that there is no Néel temperature below which AFM order is expected, and the system remains disordered even at 0 K [5]. However, no exact, analytical solution exists for the AFM Heisenberg on a triangular lattice (AFMHTL) or any other lattice in d>1, and theorists have relied on rough approximations to predict the ground state. Before numerical computation methods were available, Philip W. Anderson's 1973 Quantum Spin Liquid (QSL) theory was among the most influential. Motivated by the geometrical frustration of the triangular lattice, which makes it impossible for all spins to anti-align with their NNs, he argued that the ground state of the AFMHTL is a fluctuating singlet state called a QSL and later proposed that QSLs in a square lattice have ties to high temperature superconductivity [6, 7]. Despite growing scientific consensus that the ground state of the AFMHTL is, in fact, a 120^o long range ordered (LRO) Néel state [8–10], the potential utility of a QSL motivated

many to continue searching for suitable models. The search for QSL states on a triangular lattice eventually led to the experimental study of κ-(BEDT-TTF)$_2X$ charge transfer salts.

In this dissertation, I present research on the group of materials responsible for spearheading the experimental study of QSLs in 2D triangular lattices, κ-(BEDT-TTF)$_2X$, using Nuclear Magnetic Resonance. Within this group of materials, κ-(BEDT-TTF)$_2$Cu$_2$(CN)$_3$ (κ-CuCN) emerged in 2003 as the first 2D triangular QSL candidate [11]. Despite having an exchange interaction, J, of approximately 250 K, ^{1}H NMR experiments detected no magnetic order, long range or short range, down to temperatures of 32 mK. However, lack of magnetic order is not definitive evidence for a QSL state. In fact, it has not yet been clarified what exact set of experimental evidence is needed to qualify a QSL [12, 13]. Bridging the gap between theory and experiment remains an ongoing problem. The work in this dissertation involving κ-CuCN and its cousin compounds, κ-(BEDT-TTF)$_2$Hg(SCN)$_2$Cl (κ-HgCl) and κ-(BEDT-TTF)$_2$Hg(SCN)$_2$Br (κ-HgBr), serves two primary aims: first, to investigate the role of charge degrees of freedom in promoting or limiting QSL manifestation in κ-(BEDT-TTF)$_2X$ materials, and second, to investigate the nature of the low energy excitations in κ-CuCN in order to determine its ground state.

1.2 Quantum Spin Liquid Theory

1.2.1 What is a Quantum Spin Liquid?

Despite continued excitement about this novel state and its potential applications, the QSL is not well understood, even among many within the condensed matter community. I will first provide an overview of the definitive properties of the QSL state that distinguishes it from other states of matter. Despite some attempts to experimentally investigate QSL properties, theoretical treatments are still quite varied, with many models in existence describing QSLs with distinct characteristics. In this chapter, I will focus on triangular models – a full discussion of models is outside the scope of this work, but see [13–16] for some excellent reviews.

All of the models agree on one thing: a QSL is a state of matter with quantum disordered, highly entangled spins. The cartoon picture of a QSL is best described by Anderson's Resonating Valence Bond (RVB) description. To start, we define a Valence Bond Solid (VBS) state which has every spin on the lattice form a singlet pair, or a Valence Bond, with a nearest-neighbor spin (see Fig. 1.1(a)). Because singlets don't have any spin, the VBS state is nonmagnetic. The biggest distinction between a VBS and a QSL is that the singlet pairs in a VBS are restricted to nearest-neighbors and form along a fixed direction. Therefore, a transition into a VBS state, at the very least, breaks translational or rotational symmetry. In contrast, spins in a QSL do not have any preference which spin they form bonds with, and are not restricted to pair only with nearest neighbors. Thus, the QSL is the superposition of all possible microstates of valence bond pairings, including long distance pairings that are restricted in the VBS, and allows fluctuation between these states without any cost in energy. The QSL remains nonmagnetic like the VBS, but its singlet pairs are constantly fluctuating or "resonating" even at 0 K, thus the name "Resonating Valence Bond." This resonating nature is the "quantum disorder" in QSLs.

The most important property of the high level entanglement in QSLs is the ability to support non-local and fractionalized excitations. In fact, the low-energy effective theory of QSLs is currently a deconfined gauge theory [15]. Since transition into a QSL state does not require any symmetry breaking, one instead needs to prove the presence of non-local, deconfined excitations in the ground state along with nonmagnetic, insulating properties. One of the most frequently encountered quasiparticles mentioned in QSL theory is the fermionic spinon which carries half-odd integer spin, usually spin 1/2. However, there are models which support anyons, photons, and other types of quasiparticle excitations.

The original theory, proposed by P.W. Anderson in 1973, suggested looking for such a state in an isotropic triangular lattice with AFM interactions [6]. Supposedly, the "frustration," arising from the fact that there is no spin orientation that can anti-align all nearest neighbors simultaneously, can suppress magnetic order and enable the quantum fluctuations that define a QSL state. Although this original formulation has fallen out of favor, different

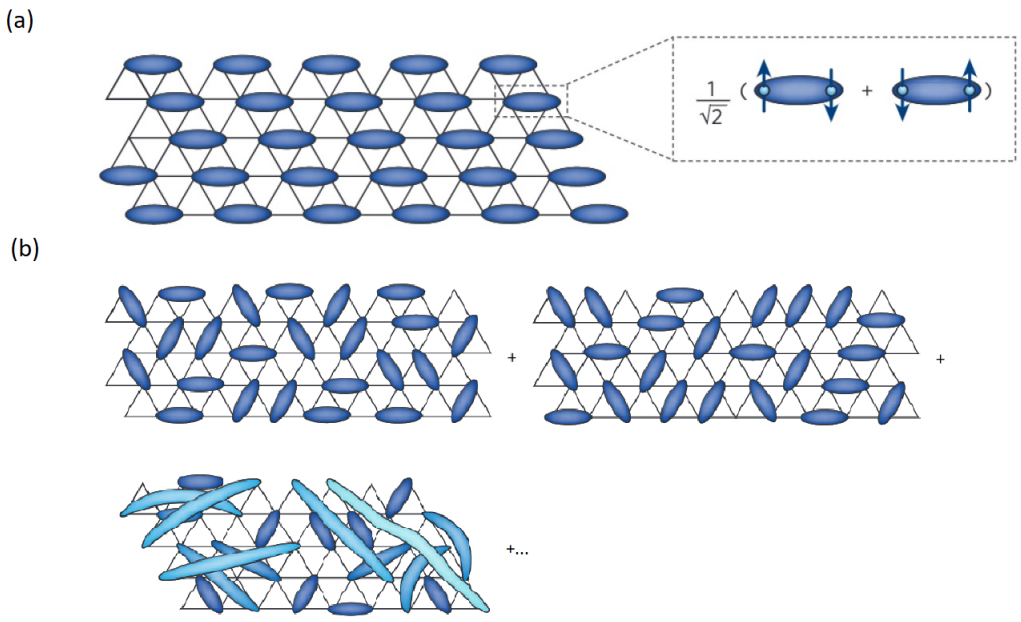

Figure 1.1: (a) Illustration of a Valence Bond Solid state. (b) The QSL is a superposition of all possible valence bond pairings in a lattice. Adapted from Reference [14].

models which include frustrated lattices like the *distorted* triangular and Kagome lattices (Fig. 1.2) have been found to host QSL-like ground states.

Because this dissertation is focused on organic conductors with triangular lattices, I will focus my discussion on a subset of triangular lattice models most relevant to the work, although this discussion is not exhaustive.

1.2.2 Relevant Hamiltonians

Before discussing the details of each model, I will briefly describe the most frequently encountered Hamiltonians, the meanings of the variables in them, and their physical implications.

1.2.2.1 The Hubbard Model

One of the earliest models encountered in condensed matter that includes electron correlations is the Hubbard Model. In the simplest picture, electrons with kinetic energy hop on a

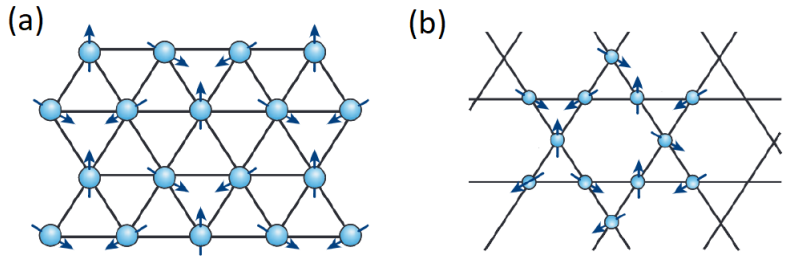

Figure 1.2: (a) Triangular lattice with 120^o Néel state ordering. (b) Kagome lattice with the same order. Adapted from Reference [14].

lattice from one site to another while being repelled by the Coulomb force of other electrons. It is written as:

$$\mathcal{H} = -\sum_{\langle \boldsymbol{i},\boldsymbol{j}\rangle\sigma} t_{ij}\left(\hat{c}^{\dagger}_{\boldsymbol{i},\sigma}\hat{c}_{\boldsymbol{j},\sigma} + \hat{c}^{\dagger}_{\boldsymbol{j},\sigma}\hat{c}_{\boldsymbol{i},\sigma}\right) + U\sum_{\boldsymbol{i}} \hat{n}_{\boldsymbol{i}\uparrow}\hat{n}_{\boldsymbol{i}\downarrow} \tag{1.1}$$

In the first term, t_{ij} is the "hopping term" and is a measurement of how much overlap there is between ionic wave functions centered at lattice sites, $\boldsymbol{i}$ and $\boldsymbol{j}$. Greater overlap means higher chance of electrons hopping between the two sites. $\hat{c}^{\dagger}$ and $\hat{c}$ are electron/spin creation and annihilation operators, respectively. The subscripts of the operator indicate which lattice site a spin, σ, is being created/annihilated at. The second term in the Hamiltonian adds a Coulomb energy cost, U, should two electrons, required to obey the Fermi-Exclusion Principle, sit on the same site.

Sometimes, it is necessary to use the extended Hubbard model which includes the Coulomb interaction between next-nearest-neighbor (NNN) spins:

$$\mathcal{H}_{NN} = V\sum_{\langle \boldsymbol{i},\boldsymbol{j}\rangle} \hat{n}_{\boldsymbol{i}}\hat{n}_{\boldsymbol{j}} \tag{1.2}$$

Inclusion of this term allows for charge order in a lattice, which becomes relevant for certain materials, such as κ-(BEDT-TTF)$_2$Hg(SCN)$_2$Cl and κ-(BEDT-TTF)$_2$Hg(SCN)$_2$Br.

1.2.2.2 The Heiseinberg Model

For half-filled lattices in the limit of $U \gg t$, the tight binding model would normally predict conducting properties. However, the Hubbard Model predicts that when the cost of placing two electrons on one site is significantly large, the system prefers a state where electrons are localized, despite being in a half-filled band. The result is a special type of insulator called a "Mott Insulator". In the Mott Insulator limit, it is assumed that no electron hopping occurs, and the Hubbard Hamiltonian, after some algebra, is transformed into the Heisenberg Hamiltonian:

$$\mathcal{H} = \sum_{\langle \boldsymbol{i},\boldsymbol{j} \rangle} \frac{4t_{ij}^2}{U} \boldsymbol{S_i} \cdot \boldsymbol{S_j} = \sum_{\langle \boldsymbol{i},\boldsymbol{j} \rangle} J_{ij} \boldsymbol{S_i} \cdot \boldsymbol{S_j} \tag{1.3}$$

where $J_{ij} > 0$ is the AFM exchange interaction between neighboring spins, $\boldsymbol{S_i}$ and $\boldsymbol{S_j}$.

1.2.2.3 The Ising Model

Eliminating exchange terms $S_{ix}S_{jx}$ and $S_{iy}S_{jy}$ leads to the Ising Hamiltonian:

$$\mathcal{H} = \sum_{\langle \boldsymbol{i},\boldsymbol{j} \rangle} J_{ij} \sigma_{\boldsymbol{i}} \sigma_{\boldsymbol{j}} \tag{1.4}$$

In the Ising Model, the spin vectors are dropped and replaced with scalars, σ, which are restricted to the values of + or - 1, representing alignment or anti-alignment, respectively, along the $\hat{z}$ axis.

1.2.3 Classification of QSLs

If an approach to estimating the ground state of any of these Hamiltonians on a lattice results in a QSL-like state, some attempt at classifying the state is made. There is no general convention for the classification of QSLs, but most follow this pattern: [*Spectrum of Low-Energy Excitations*] + [*Lattice Gauge Symmetry*]. In an effort to make the terminology more familiar for the reader, I shall summarize the meanings of those classifications here.

1.2.3.1 Energy Spectrum

A QSL is first classified by the spectrum of its low-energy excitations. The energy spectrum may be continuous, having excitations very close to 0 K, in which case it is considered *gapless*. It may also contain a gap between the ground state and the lowest energy excitation, which would classify at as activated, or *gapped*. Gapped spectra typically have exponentially decaying thermodynamic observables with respect to temperature while gapless spectra exhibit power law behaviors. In general, gapped QSLs can have topological origins while gapless QSLs require more involved approaches, for example a combination of parton theory and gauge theory, to explain.

1.2.3.2 Lattice Gauge Theory

The QSLs in each of these models are subject to a certain lattice gauge theory, meaning the system is defined by a *field* with which a certain set of operations leaves the measurable *observables* invariant, or unchanged. The conditions for the deconfined phase(s), its quasiparticles, and the associated excitation spectrum follow closely from the gauge theory. Therefore, it is important that QSLs are identified according to the lattice gauge theory with which they are subject to. A full discussion of gauge theory is outside the scope of this dissertation. Instead, I will summarize the main properties of the symmetry groups most frequently mentioned in the models of section 1.2.4: U(1) and Z_2. SU(2) is also common in QSL literature, but does not show up in any of the models discussed in this dissertation. The interested reader should refer to the review by Zhou, Kanoda, and Ng for a detailed explanation as to what it means to be a SU(2) QSL [16].

U(1) QSLs are easy to explain due to the fact that they share the same gauge theory as electromagnetism (EM), except applied to a discretized spacetime. The gauge field is the vector field A_{mn}. However, unlike in EM, A_{mn} lives on the edges of a lattice, effectively quantizing the lattice, and is named by the vertices of the edge it sits on. It is also conventional to use the compact U(1) gauge theory which restricts $0 \leq A_{mn} \leq 2\pi$. The vector field repre-

sents two important observables, the "electric" and "magnetic" flux, given by $E_{mn} = -\dot{A}_{mn}$ and $\Phi_{mnpq} = A_{mn} + A_{np} + A_{pq} + A_{qn}$, respectively. Whereas the electric flux is defined by a single edge, the magnetic flux is defined by a "plaquette" which is a closed loop of four edges in counter-clockwise order. The resulting deconfined phase or the "Coulomb Phase" is defined by four different types of quasiparticles. First, there exist gapless photon modes at the lowest end of the spectrum. Then, at energies greater than the gap, "electric charges" and "magnetic monopoles" carry energy and interact with 'like' charges via a "Coulomb" $1/r$ potential. Lastly, there are gapped combinations of the electric and magnetic charges called "dyons." The first three quasiparticles are considered bosons while the dyons are fermions. To produce gapless fermionic spinon excitations, one must go beyond pure gauge theory and couple U(1) gauge theory with parton theory [17].

If the U(1) QSL observables, which take on integer values, are instead restricted to binary (± 1) values, the theory becomes Z_2 gauge theory, often called the Ising Gauge. The observables in this gauge are defined by the Pauli operators, $\sigma^x \cong (-1)^E$ and $\sigma^z \cong e^{\pm iA}$, where $\prod_{plaquette} \sigma^z \cong e^{i\Phi}$. Despite being different from U(1) theory, the quasiparticles that come from Z_2 gauge theory are very similar. Pure Z_2 gauge theory does not produce gapless excitations, therefore there are no photon modes in this model. However, there are gapped *anyonic* excitations. The three different types of anyons bear a striking resemblance to the U(1) particles. They are the "electric" particles (e), "magnetic" particles (m), and fused/bound e and m particles (ϵ). As in U(1) theory, e and m are bosons while the ϵs are fermions. Unlike their U(1) counterparts, however, these excitations carry binary units of energy (as is required by Z_2 gauge theory). Pure Z_2 gauge theory is also sometimes referred to as topological Z_2 gauge theory, because it is identical to Kitaev's "Toric Code," which produces four-fold topologically degenerate ground states [18]. Kitaev's honeycomb model, which is solved via a combination of parton physics and gauge theory, is an example of a Z_2 model which supports gapless excitations [19].

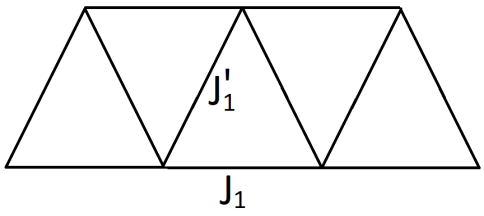

Figure 1.3: Intra-chain interaction J_1 vs Inter-chain interaction J_1'.

1.2.4 QSL Models on a Triangular Lattice

The reader should now be familiar enough with the minimal knowledge required to understand the basis of each model in this section as well as the implications of the predictions made by the models. I will summarize the main assumptions of each approach and what kind of QSL they predict.

1.2.4.1 Heisenberg $^{++}$

Although the NN AFMHTL orders in a 120^o ground state, it is reasonable to ask whether modifications to the couplings might suppress the long range order. It turns out, with slight modifications to the Heisenberg Hamiltonian, one *can* find states with QSL-like properties. The QSLs in these models are identified as areas where there is little to no magnetic moment per lattice site.

Two of the most common modifications include adding weak but non-negligible NNN interactions and spatial anisotropy of the NN. The complete Hamiltonian, including both of these terms, is of the form:

$$\mathcal{H} = J_1 \sum_{\langle \boldsymbol{i},\boldsymbol{j} \rangle} \boldsymbol{S_i} \cdot \boldsymbol{S_j} + J_1' \sum_{\langle \boldsymbol{i},\boldsymbol{j} \rangle} \boldsymbol{S_i} \cdot \boldsymbol{S_j} + J_2 \sum_{\langle\langle \boldsymbol{i},\boldsymbol{j} \rangle\rangle} \boldsymbol{S_i} \cdot \boldsymbol{S_j} \tag{1.5}$$

where J_1 and J_1' denote NN intra-chain and inter-chain interaction strengths, respectively (see Fig. 1.3). Note, the definitions of J_1 and J_1' are usually switched in the literature for κ-$(\mathrm{ET})_2X$ materials. J_2 is the NNN interaction.

Monte Carlo calculations, which neglected NNN interactions, but included spatial anisotropy

between NN, found QSL states in the regime $J'/J < 0.8$ (subscripts dropped) [20, 21]. Above 0.8, in the $J'/J \sim 1$ range, is the 120^o Néel state, as expected, while the $J'/J \gg 1$ limit, which approaches a square lattice, produces the collinear Néel state. The study, which looked closer at the $J'/J < 0.8$ region, found a gapless, fractionalized QSL for $J'/J \lesssim 0.65$ and a gapped, topological Z_2 QSL in the intermediate $J'/J \lesssim 0.65 \lesssim 0.8$ range [21].

The case where anisotropies are ignored, but NNN interactions are included, has also been examined using variational Monte Carlo [22, 23] and density matrix renormalization group (DMRG) [24, 25]. QSL states are stable in the region $0.06 \lesssim J_2/J_1 \lesssim 0.17$. Similar to the above studies, which only included anisotropy, the 120^o Néel state and collinear Néel state are sitting nearby, with the 120^o state directly below the QSL region and the collinear state above.

Unlike the anisotropy-only case, it is less clear which QSL state is produced by this model. The most recent suggestion is a Z_2-type QSL, possibly with a chiral (time reversal symmetry breaking) QSL nearby. Hu *et al.*, who studied the $J_1 - J_2$ case using DMRG, added anisotropy to the nearest-neighbors and concluded that the Z_2 state becomes more stable with a weaker J_1' while the chiral correlations are more "enhanced" with larger J_1' [25].

1.2.4.2 Hubbard

As mentioned in section 1.2.2, when the on-site Coulomb interaction is not strong enough relative to the hopping constant, the Heisenberg Hamiltonian is not valid, and it is necessary to use the Hubbard Model. Most theorists now believe this to be the case with κ-$(ET)_2$ salts, which are the materials studied in this dissertation.

One very notable study which analyzes this Hamiltonian was done by Morita *et al.*, who tackled the case of the anisotropic triangular lattice, which they dubbed the t-t'TH model [26]. The Hamiltonian took the form:

$$\mathcal{H} = -t \sum_{\langle \boldsymbol{i},\boldsymbol{j}\rangle\sigma} \left(\hat{c}^\dagger_{\boldsymbol{i},\sigma}\hat{c}_{\boldsymbol{j},\sigma} + \hat{c}^\dagger_{\boldsymbol{j},\sigma}\hat{c}_{\boldsymbol{i},\sigma}\right) + t' \sum_{\langle \boldsymbol{k},\boldsymbol{l}\rangle\sigma} \left(\hat{c}^\dagger_{\boldsymbol{k},\sigma}\hat{c}_{\boldsymbol{l},\sigma} + \hat{c}^\dagger_{\boldsymbol{l},\sigma}\hat{c}_{\boldsymbol{k},\sigma}\right) + U \sum_{\boldsymbol{i}} \hat{n}_{\boldsymbol{i}\uparrow}\hat{n}_{\boldsymbol{i}\downarrow} \tag{1.6}$$

which should be interpreted as usual, except with two nearest-neighbor hopping terms of dif-

ferent magnitude (t' representing the intra-chain hopping term, t the inter-chain). Applying a fairly new technique at the time called the path integral renormalization group (PIRG), Morita *et al.* found a "non-magnetic insulator" state in the range $4 < U/t < 10$ with no sign of any symmetry breaking. This range of U/t can be interpreted as "Mott insulators nearby the Mott metal insulator transition." This was a very early study, and the type of QSL was not specified, but later studies of this model have converged upon a gapless U(1) QSL with fermionic spinon excitations [27].

1.2.4.3 Permutations and Projections

The approaches listed below focus on summations of permutation or projection operators over all possible dimers or plaquettes in a lattice.

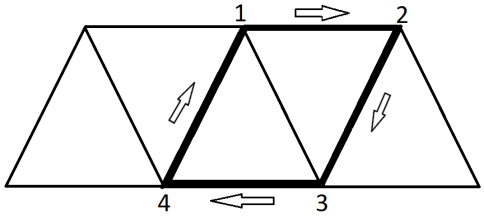

Figure 1.4: Four-site rhombus plaquette on a triangular lattice with arrows indicating the direction in which spins would be swapped by the P_{1234} operator.

The first of the two models which I will discuss is called the Ring Exchange model and was developed as a way to bypass some problems that stemmed from the Hubbard approach [28]. This model is technically a Heisenberg model with the addition of a so-called "ring exchange." The Hamiltonian is:

$$\mathcal{H}_{\mathrm{RE}} = J_2 \sum_{\text{⚊}} P_{12} + J_4 \sum_{\square} (P_{1234} + P_{1234}^{\dagger}) \tag{1.7}$$

The first term sums over all possible dimer configurations in the lattice and swaps the spins with a strength denoted by J_2. This term is the Heisenberg interaction, since $P_{12} = P_{12}^{\dagger} = 2\boldsymbol{S_1} \cdot \boldsymbol{S_2} + 1/2$ using the $\hbar = 1$ notation. The P_{1234} operator in the second term sums

over all four-site rhombi plaquettes and permutates the spins in a clockwise direction, like musical chairs (see Fig. 1.4). $P^{\dagger}_{1234}$ does the same, but counter-clockwise. The tendency of this "ring exchange" to occur is denoted by J_4. Through a variational approach, trial wavefunctions for this Hamiltonian were compared, and, indeed, a QSL state was found for $J_4/J_2 \gtrsim 0.3$ of the same type obtained by the Hubbard approach.

The last model I will discuss is the Quantum-Dimer Model (QDM). Despite being the last mentioned approach, this is the original approach used by Anderson to describe the RVB state. In his original paper, Anderson deliberately constructed variational wavefunctions which were linear combinations of singlet (quantum-dimer) pairings on the spin-1/2 Heisenberg triangular lattice and showed that those wavefunctions produced a lower energy than the 120^o Néel state [6]. His calculations were limited to a railroad-trestle lattice and turned out to be incorrect for the larger 2D triangular lattice. Nonetheless, a new QDM model inspired by Anderson's RVB description was formulated with a Hamiltonian of a different form:

$$\mathcal{H}_{\mathrm{QDM}} = \sum_{i=1}^{\mathrm{N_p}} \Bigg\{ -t \sum_{\alpha=1}^{3} \left(|\,\rangle\langle\,| + |\,\rangle\langle\,| \right) + V \sum_{\alpha=1}^{3} \left(|\,\rangle\langle\,| + |\,\rangle\langle\,| \right) \Bigg\} \qquad (1.8)$$

The outer summation considers all possible 4-site rhombi plaquettes in the lattice while the two inner summations go over the three different types of plaquettes possible. Bold lines in the plaquette symbol indicate bonded pairs while dashed lines indicate no bond. Note, spins can only form a bond with one other, nearest-neighbor spin at a time in the QDM model. The first term in the Hamiltonian decreases the energy of the system any time a "flippable" plaquette (one containing parallel dimers) is encountered and flips the dimers in the plaquette. The second term increases the energy of the system whenever a flippable plaquette is encountered but otherwise leaves the system alone. This Hamiltonian was originally applied to the square lattice by Rokhsar and Kivelson [29] who found a QSL, a state described by the superposition of flippable plaquettes, that later turned out to be unstable. Moessner and Sondhi applied the same approach to the triangular lattice and found a stable QSL nearby $V \lesssim T$, which is described as short ranged (not forming pairs with far away neighbors), gapped, with spinon excitations [30].

1.3 Properties of κ-(BEDT-TTF)$_2X$

Several models on the triangular lattices have been shown to exhibit QSL ground states. This is a primary justification for investigation of κ-(ET)$_2X$ materials, which have a triangular lattice structure and properties that fall within the bounds of interest for QSL manifestation. This section summarizes the properties of these materials and elucidates why these materials are considered good candidates.

1.3.1 Crystal Structure

The 3D lattice groups for the κ-(ET)$_2X$ compounds are often debated, with the structure varying between different compounds. This is of little consequence, because the conducting properties of each depend primarily on the in-plane, 2D structure of the BEDT-TTF layer, which will be discussed later. It has been long thought that the structure of κ-CuCN is monoclinic [31, 32], but a recently proposed recalculation claims the actual structure is triclinic [33]. Similarly, when κ-HgCl and κ-HgBr first appeared in literature, their crystal structures were quoted as monoclinic [34], but authors in a later study on κ-HgBr cited the structure as unknown [35].

Regardless of what the actual crystal groups are, all κ-(ET)$_2X$ consist of alternating layers of organic donor molecules (BEDT-TTF or ET for short) and polymeric anion (X) sheets as shown in Fig. 1.5(a). The *mostly* planar structure of the ET molecules (Fig 1.5(c)) allows them to be stacked closely to each other, resulting in sufficient overlap of the ET molecular orbitals. Because of this, the bulk of the conduction occurs within the ET layers, and the κ-(ET)$_2X$ transfer salts are considered quasi-2D conductors. This makes the structure of the donor layer, which is rhombic or anisotropic triangular (Fig. 1.5(b)), much more important than the bulk 3D structure. The ET stacking is achieved through the joint donation of an electron from two ET molecules to one anion X. Ideally, each anion carries -1e charge, while each ET molecule carries +0.5e charge. However, inequivalencies do exist among the donor molecules resulting in charge disproportionation or charge ordering (CO).

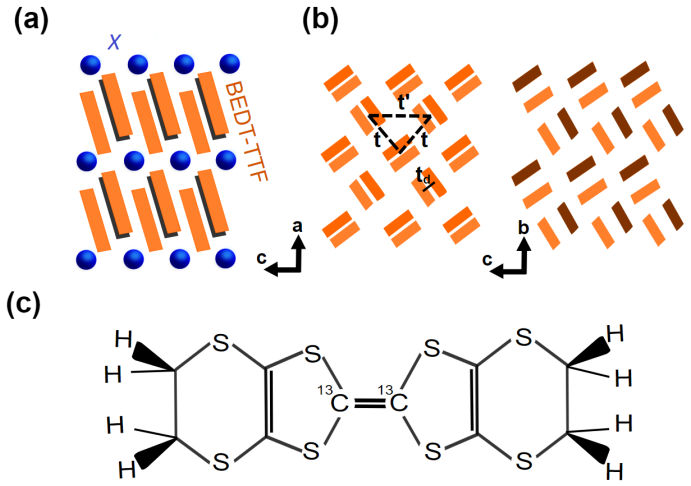

Figure 1.5: (a) Layered structure of κ-(BEDT-TTF)$_2X$ salts. (b) Within the conduction layer, dimers sit on a triangular lattice with varying degrees of dimerization. (c) Molecular structure of ET molecule with central carbons replaced by ^{13}C.

1.3.2 Band Structure

While all κ-(ET)$_2X$ transfer salts possess relatively strong intra-ET coulumb repulsion (U in Eq. 1.1), they have a range of electronic properties which depend greatly on temperature and the transfer integrals (t, t', t_d) between the ET molecules. Among the transfer integrals, the strength of dimerization, t_d/t, between pairs of ET molecules plays the biggest roll in whether or not the material will undergo a Mott metal insulator transition (MIT).

1.3.2.1 Weak Dimerization

At high enough temperatures or for weak levels of dimerization (right side of Fig. 1.5(b)), the quasi-2D band structure, obtained via tight binding methods, looks similar to the structure pictured in Fig. 1.6(a). There are a total of four distinguishable bands. The higher energy bands are composed of anti-bonding orbitals while the lower bands are composed of bonding orbitals. The lattice is 1/4 filled, and it is clear that the higher energy bands, which intersect E_F, form a 2D fermi surface.

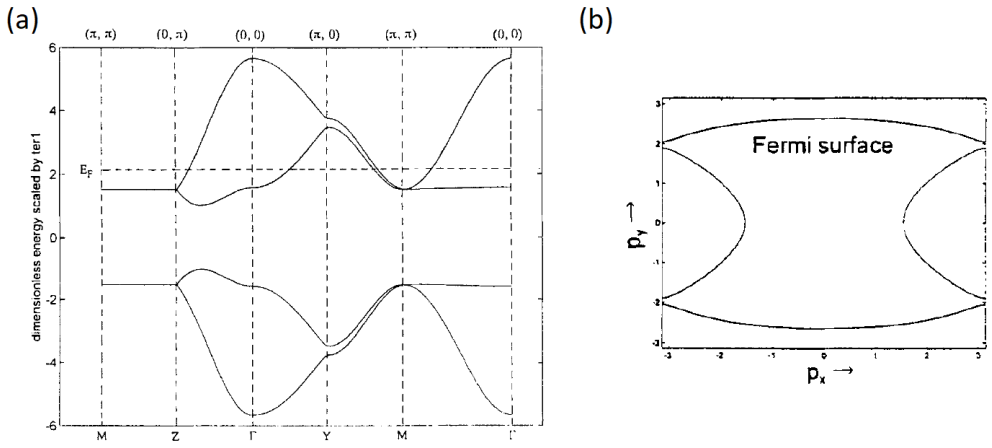

Figure 1.6: (a) Generic quasi-2D band structure of a κ-$(ET)_2X$ crystal in the metallic phase, calculated via tight binding methods. (b) Fermi surface associated with energy dispersion in (a). Figure adapted from Ref [36].

1.3.2.2 Strong Dimerization

In some κ-$(ET)_2X$ salts, low temperatures and/or strong dimerization can lead to a Mott-Insulating state. When the strength of dimerization is strong enough, one can transition from considering each ET molecule as a lattice site to instead considering each *dimer* as a lattice site (left side of Fig. 1.5(b)). The number of lattice sites per unit cell is effectively halved, and what was once a 1/4 filled lattice is now a half-filled lattice. As temperature decreases, the strength of t decreases relative to U, and the conditions for a Mott-Insulator are met. It has been shown that the strength of dimerization in κ-$(ET)_2X$ is positively correlated with the energy gap between the anti-bonding and bonding bands [37], and for strong enough dimerization, the anti-bonding bands are pushed completely above the Fermi energy as shown in Fig. 1.7.

A very important feature to note is that all κ-$(ET)_2X$ compounds are considered weak Mott-Insulators, with $U/t = 7.3$ for κ-CuCN [31, 38, 39] and 4.4 for κ-HgCl and κ-HgBr [39]. As a result, there is debate as to whether the Heisenberg or Hubbard Hamiltonian is the appropriate model to use when studying these materials. The current standard for weakly dimerized variants is to use the extended Hubbard Model which includes NNN Coulomb

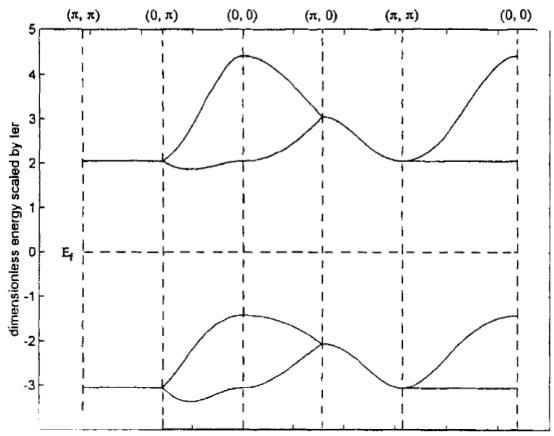

Figure 1.7: (a) Generic band structure of a κ-$(ET)_2X$ crystal in the insulating phase, calculated via tight binding methods. Figure from Ref [36].

interactions, allowing for the possibility of charge order. Nevertheless, as discussed in section 1.1.4.2, it has been proposed that frustrated magnets sitting nearby a Mott transition can host QSL states.

1.3.3 The ET Molecule and its HOMO

All of the models in section 1.2.4 begin at the Hamiltonian and do not specify any real materials. It is the job of experimentalists to connect the properties of their real crystal system to the relevant variables in each of these models. As previously described, one ET dimer pair is considered a single lattice site in κ-$(ET)_2X$ as long as the dimerization strength (t_d/t) is sufficiently large. It is also important to know that the strength of the transfer integrals, exchange interactions, and Coulomb repulsions depend on the shape, size, and overlap of the electron orbitals surrounding the ET molecules. Since the ET layer is the donor layer, the molecular orbital of importance is the *highest occupied molecular orbital* (HOMO).

I start with the physical structure of the ET molecule. ET is short for BEDT-TTF, which is short for bis(ethylenedithio)tetrathiafulvalene, and has the molecular formula $C_{10}H_8S_8$. While the chemical name is cumbersome, the structure of the molecule can be broken down

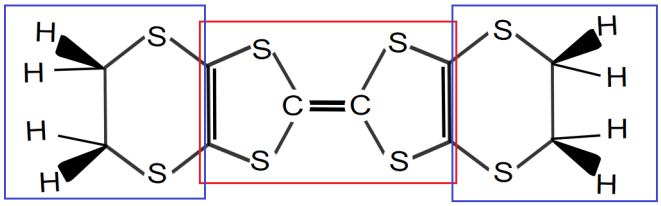

Figure 1.8: Molecular structure of BEDT-TTF, reused to show the important parts of the molecule. Red box is the center tetrathiafulvalene (TTF) while the blue boxes are the ethylenedithio (EDT) molecules.

into two parts. First, the center of the molecule is a tetrathiafulvalene (TTF) molecule, $(H_2C_2S_2C)_2$, without the hydrogen atoms at the end (red box in Fig. 1.8). Instead of hydrogens, the carbons at the end of TTF connect with an ethylene (C_2H_4) with 2 sulfurs, denoted in chemical nomenclature as ethylenedithio (EDT) (blue boxes in Fig. 1.8). The bis (B) in front of the EDT tells us that there are two EDT, one at each end of the TTF. Because the ethylenes are connected to two sulfur atoms via the carbon atoms, the carbon double bond in ethylene is instead a single bond in EDT. The ethylenes at the end of the molecule are often referred to as the *ethylene end groups* (EEG).

More important than the physical structure of the ET molecule is the HOMO, which is a measurement of the carrier density around each atom in the molecule, since the charge transfer to the counterion sublattice leads to unfilled states originating with the HOMO. The general structure of a neutral ET HOMO is shown in Fig. 1.9. In the neutral molecule, it is clear that the atomic orbitals which contribute the most to conductivity are located in the TTF center. The orbitals are p-type orbitals with the axes pointing almost perpendicularly out of the TTF plane.

It is also important to note that ET molecules are not perfectly planar and are not all equivalent in the lattice. The TTF part of BEDT-TTF is planar while the BEDT ends, owing to the different conformations of the EEGs, tilt slightly out of plane. ET molecules take one of two, eclipsed or staggered (Fig. 1.10), conformations. At higher temperatures, κ-$(ET)_2X$ often have some level of EEG disorder, possessing a mixed population of staggered and

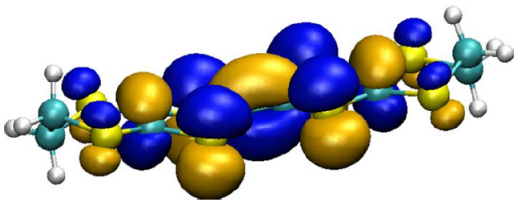

Figure 1.9: (a) Highest occupied molecular orbital (HOMO) of a neutral ET atom. Figure taken from Ref [40].

eclipsed ET without any clear pattern. While a naive examiner looking at the HOMO would conclude that the conformations, which differ only in the orientation of the EEGs, should have little effect on the electronic properties of κ-$(ET)_2X$, experimental studies have proven otherwise. For example, one study suggests EEG disorder may play a role in stabilizing a MIT [41], and the T_c dependence on cooling rates in some superconducting materials have also been linked to EEG disorder [42].

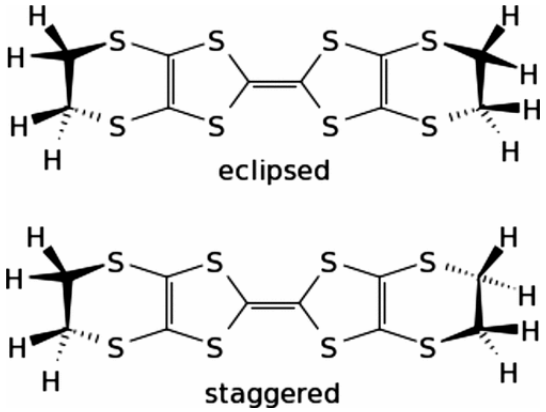

Figure 1.10: Comparison of eclipsed vs. staggered ET molecules. Figure from [43].

1.3.4 The Effects of Disorder

It has become clear in recent years that disorder has profound effects on the low temperature behavior of κ-$(ET)_2X$ materials. Disorder has been considered before in the literature [44–46], but cannot be described by a universal model because of its broad definition. Disorder can mean a couple of different things:

Quenched Disorder: Real materials are not perfectly clean, and κ-$(ET)_2X$ materials are known to be impure. Site disorders in the form of impurities, vacancies, and other defects are not unheard of, although the prevalence of these defects is unknown. Proposed effects range from the creation of unpaired spins, which destroy order in what otherwise would be an ordered lattice, to a random distribution of J, leading to a spin-glass state.

Entropy Disorder: Disorder can also refer to the symmetry of the state being described. This can lead to some confusion as the QSL is considered a disordered state, but in this context means a state with no broken symmetry. However, this type of disorder has also been discussed as a potential mechanism for QSL emergence. For example, it has been proposed that the presence of a fluctuating (disordered) electric dipole state could introduce frustration to a system and stabilize the QSL state [45].

Because there are too many particularities when it comes to disorder, I will reserve deeper discussions to the parts of the dissertation in which they arise.

1.3.5 Comparison of X = CuCN, HgCl, HgBr

1.3.5.1 QSL candidate or not?

Before any of the results in this dissertation were published, κ-CuCN was the only QSL candidate among the three materials studied. So far, the qualifying property for QSL candidacy is the absence of magnetic order at very low temperatures without symmetry breaking, since many QSL models do not agree on other behaviors. Early electron paramagnetic resonance (EPR) measurements on κ-HgCl saw a sharp increase in ΔH accompanied by a rising g-factor [34] at $T = 27$ K. This behavior was tentatively linked with AFM ordering and, if true, disqualified κ-HgCl as a QSL candidate. However, the NMR experiments detailed in this dissertation detected no magnetic order down to 25 mK, making κ-HgCl a QSL candidate. To date there has not been any evidence for long range order in κ-HgBr but comparison of zero-field-cooled (ZFC) and field-cooled (FC) EPR measurements revealed a possible glassy-state transition at $T = 40$ K [47], also disqualifying κ-HgBr as a QSL candidate. The

same authors also saw signatures of weak ferromagnetism below 20 K. More recent magnetic susceptibility and magnetic torque measurements support the ferromagnetism claim while disputing the glassy-state [48].

1.3.5.2 The Current Status of κ-CuCN as a QSL

It has been 20 years since κ-CuCN became the first known 2D triangular QSL candidate, but the list of questions related to its ground state continues to grow. For example, it is still disputed exactly what type of QSL κ-CuCN hosts, if any at all.

The Gap Problem:

Perhaps one of the biggest road blocks toward identification of the QSL is the uncertainty surrounding the low energy excitation spectrum of the material. It is crucial to determine whether the ground state is gapped or ungapped in order to narrow down the number of models with which the QSL can be described by. However, early attempts at doing this returned mixed results. Specific heat measurements by S. Yamashita *et al.* showed a field-independent, linear term, γT, where $\gamma \approx 15$ mJ/K^2 mol [49]. The presence of this term suggests the existence of low energy excitations attributed to fermi-like quasiparticles. Just a year later, M. Yamashita *et al.* conducted thermal conductivity measurements which showed a vanishing κ/T, where κ is the thermal conductivity. Their results were interpreted as evidence for a spin-gap of 0.46 K [50]. However, there are additional results which are interpreted as consistent with a gapless state, such as NMR relaxation and magnetic susceptibility [11, 51]. Furthermore, another organic triangular QSL candidate, M[Pd[dmit]$_2$]$_2$, consistently exhibits gapless behavior [52, 53], and it was assumed that κ-CuCN was gapless as well. However, very recently, Miksch *et al.* published results in which the EPR response was interpreted as evidence for the opening of a spin gap $\Delta \simeq 12$ K that onsets at $T \simeq 6$ K [54]. In response to the renewed challenge of the gapless state, high field NMR experiments were performed and are discussed in chapter 5 of this dissertation.

The 6 K Anomaly:

Miksch *et al.* were motivated by a particular phenomenon well known to occur in κ-CuCN. In almost every low energy measurement performed on κ-CuCN, there exists a "6 K Anomaly". Inverse spin-lattice relaxation, spin susceptibility, and thermal conductivity (see Fig. 1.11) are a few examples where an anomalous dip occurs at 6 K, followed by a peak which falls off as $T \to 0$ [11, 50, 51].

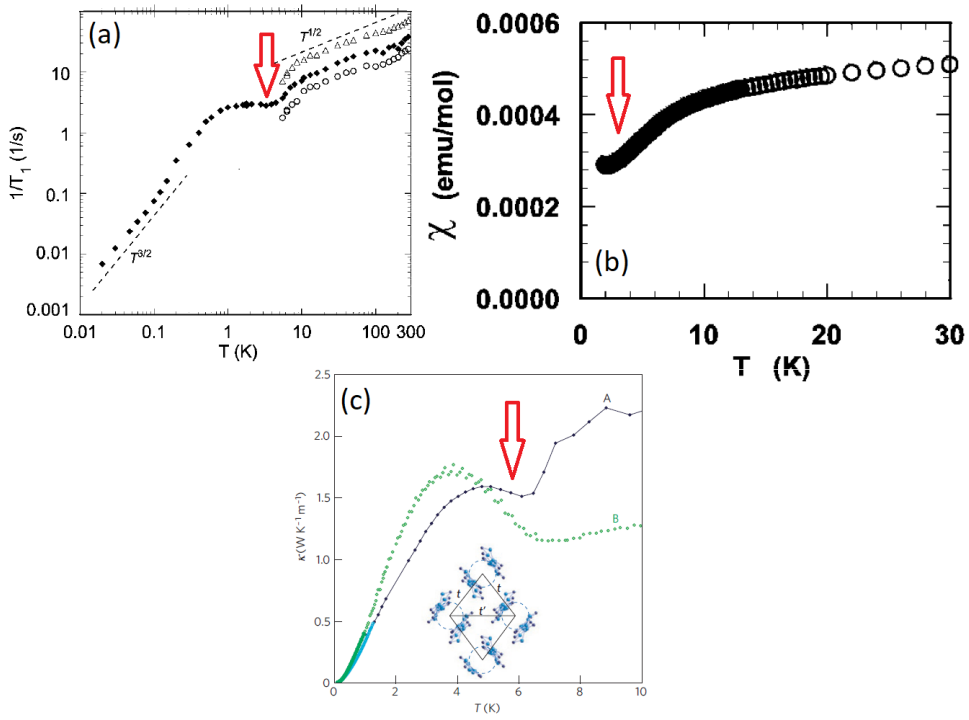

Figure 1.11: Examples of 6K anomaly in measurements of κ-CuCN with red arrow pointing at anomaly. (a) ^{13}C $1/T_1$ [51]. (b) Susceptiility [11]. (c) Thermal conductivity [50]

The true origin and/or nature of this anomaly is still unknown, but many in the QSL community now believe it to be associated with a second-order phase transition that is also coupled with a structural change in the crystal [55, 56]. It is currently a topic of debate whether or not this second-order phase transition can be consistent with a QSL state. If the broken symmetry implied by the transition is related to the spin degrees of freedom, then κ-CuCN cannot be a QSL. Some believe the anomaly marks the appearance of coexisting quantum electric dipoles, which may help stabilize the spin liquid [45], while others believe

it marks a transition into a Valence Bond state rather than a QSL [44]. A general and comprehensive discussion of the "6 K anomaly" is presented in Ref. [57].

1.3.5.3 κ-CuCN vs. κ-HgCl and κ-HgBr

In this dissertation, I conducted experiments on κ-CuCN with the intent of investigating the 6 K anomaly and its potential connection to a VBS transition or other states. The information learned from studying κ-HgCl and κ-HgBr were informative in that regard. However, studying κ-HgCl and κ-HgBr also allowed us to examine the interplay of charge and magnetic degrees of freedom in κ-$(ET)_2X$ insulators with specific emphasis on any roles the charge degrees of freedom might have in the stabilization of a spin liquid.

κ-HgCl and κ-HgBr differ from κ-CuCN and other previously studied κ-type compounds because their anion layers, $Hg(SCN)_2X$, are mercury based instead of copper based. There are still questions as to what exactly the difference entails, but one consequence appears to be a change in the strength of dimerization (t_d/t). The strength of dimerization in κ-HgCl, and κ-HgBr, is weaker than in κ-CuCN ($t_d/t' \approx 3$ vs 4, respectively) [11, 58]. They also have weaker Coulomb repulsion ($U/t \approx 7.3$ in κ-CuCN vs 4.4 in κ-HgCl and κ-HgBr) [31, 38, 39]. As a result, κ-HgCl and κ-HgBr are more likely to be charge-ordered, and it is important to keep observe their charge degrees of freedom, whereas the same attention has not been paid in κ-CuCN, due to its established status as a Mott insulator.

κ-CuCN does not have any MITs at ambient pressure. However, application of pressure at low temperatures pushes κ-CuCN through a MIT and into a superconducting state [59–61]. Both κ-HgCl and κ-HgBr are conductors at room temperature with metal insulator transitions occurring at 34 K [34] and 90 K [35], respectively. Because κ-HgCl and κ-HgBr sit in a more ambiguous regime, their MITs cannot be immediately classified as Mott insulator transitions. In fact, Raman Spectroscopy experiments detected a charge disproportionation of $\delta\rho = 0.2$ within the dimers in κ-HgCl, and the MIT transition was determined to be a charge-order transition rather than a Mott transition [39]. The same experiment on κ-HgBr did not return the same results. However, a different state, coined a "quantum dipole

liquid", was instead suggested, implying the existence of fluctuating electric dipole moments between the molecules in a dimer [62]. This interpretation was strongly motivated by the "quantum electric dipole" model that was introduced for κ-CuCN, suggesting κ-HgBr may have similar physics as κ-CuCN.

CHAPTER 2

Experimental Methods

2.1 Theory of Spin Dynamics

Nuclear Magnetic Resonance experiments take advantage of the well-known interactions between a spin and a magnetic field. Generally, a large, uniform magnetic field is applied to the sample, inducing a nonzero *net magnetization* that is aligned with the magnetic field. This state is considered the *equilibrium* state for all experiments. Then, a perturbation is applied in order to knock the net magnetization out of equilibrium. What the spins do after the perturbation depends heavily on the magnetic environment around them. Therefore, the information extracted during the *relaxation process* is extremely valuable and can reveal many things about the material being studied.

2.1.1 Uniform Magnetic Fields and Larmor Precession

In classical mechanics, a static magnetic moment, $\boldsymbol{\mu}$, in a uniform magnetic field, $\boldsymbol{H_o}$, interacts with the field through these two equations:

$$\boldsymbol{\tau} = \boldsymbol{\mu} \times \boldsymbol{H_o} \tag{2.1}$$

$$U = -\boldsymbol{\mu} \cdot \boldsymbol{H_o} \tag{2.2}$$

where τ is the torque experienced by the magnetic moment and U is the energy of the moment in the field. As suggested by these two equations, a classical moment will experience torque, which causes it to precess about the magnetic field. The spin prefers to be aligned with the field, but has no means to do so in an isolated environment.

Quantum mechanical spins behave equivalently. The source of magnetic moment in nuclei is their intrinsic *angular momentum*, and the magnetic moment originating from the spin angular momentum is given by

$$\boldsymbol{\mu_s} = \frac{gq}{2m}\boldsymbol{S} = \gamma \boldsymbol{S} \tag{2.3}$$

where g is the dimensionless g-factor, q is charge, m is mass, γ is the gyromagnetic ratio, and $\boldsymbol{S}$ is the spin angular momentum vector. When a magnetic moment with angular momentum is subject to a uniform magnetic field, the moment will precess about the field with frequency, $\boldsymbol{\omega_o} = -\gamma \boldsymbol{H}$. This is known as *Larmor Precession* and is illustrated in Fig. 2.1. Both γ and

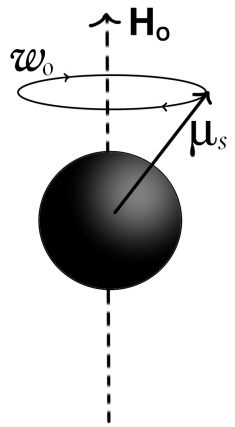

Figure 2.1: Larmor Precession of spin magnetic moment about a field.

$\boldsymbol{S}$ are particle/nuclei dependent, therefore different types of particles/nuclei will precess at different frequencies.

For a single, "classical" spin, the time averaged magnetic moment aligns along the field axis, and its magnitude is equal to the projection of $\boldsymbol{\mu_s}$ onto $\boldsymbol{H_o}$. The uniform field, $\boldsymbol{H_o}$, by convention, is aligned along the z-axis, therefore:

$$\langle \boldsymbol{\mu_s} \rangle = \mu_s \cos(\theta)\hat{z} \tag{2.4}$$

In quantum mechanics, the x and y components of the spin state oscillate while the z component remains the same. It is equivalent to write

$$\langle \boldsymbol{\mu_s} \rangle = \gamma S_z \hat{z} = \gamma(\hbar m_z)\hat{z} \tag{2.5}$$

where $\hbar$ is the reduced Plank constant and m_z is the spin quantum number of the spin in the z-basis at the time the field was applied. m_z ranges from $-s, -s+1, ..., s-1, s$ where s is total spin. It follows from Equation 2.2 that the energy of a spin in a uniform magnetic field oriented along $\hat{z}$, or the *Zeeman Energy*, is

$$U_{Zeeman} = -\hbar\gamma m_z H_o \tag{2.6}$$

The typical solid consists of many spins, all randomly oriented as in Fig. 2.2. Before a uniform magnetic field is applied, the net magnetization of the spins is zero. After a field is applied, *if all spins behaved independently, the net magnetization would still be zero*, because Larmor Precession does not change the distribution of spins oriented up versus down.

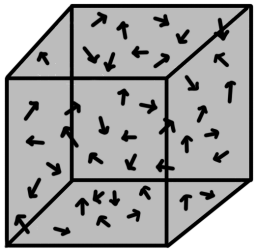

Figure 2.2: Random orientation of spins in a solid.

Thus, it is not possible to explain the theory of magnetic resonance without considering the picture of many, *interacting* spins in an environment with nonzero temperature. This requires the introduction of concepts from statistical mechanics.

2.1.2 Macroscopic Spin Picture and Thermal Equilibrium

Thermal fluctuations in the environment cause each spin to feel a field that is fluctuating in both magnitude and direction. This causes the spins to "wander", resulting in a change of orientation over time. Because it is a thermal environment, the wandering is not isotropic – meaning, the spins will prefer to be in a state of less energy.

For a single set of (same type) spins in thermal equilibrium at a temperature, T, the net

magnetic moment per volume along $\hat{z}$ is solved via statistical mechanics and is given by

$$\langle M \rangle = n\hbar\gamma\langle m \rangle \tag{2.7}$$

$$= n\hbar\gamma \frac{\sum_m e^{\hbar\gamma m H_o/k_B T} m}{e^{\beta\hbar\gamma m H_o/k_B T}} \tag{2.8}$$

$$= \frac{n\hbar\gamma}{2}\left[(2s+1)\coth\left((2s+1)\frac{\gamma\hbar H_o}{2k_B T}\right) - \coth\left(\frac{\gamma\hbar H_o}{2k_B T}\right)\right] \tag{2.9}$$

where n is the number of spins per volume, $\langle m \rangle$ is the average quantum number per spin, and k_B is the Boltzmann constant.

The above equation is quite ugly but can often be simplified due to the fact that NMR experiments typically operate in the regime where the Zeeman energy is much less than temperature. In this limit, Equation 2.9 reduces to

$$\langle M \rangle = \frac{n\hbar^2\gamma^2}{3k_B T} s(s+1) H_o \ (U_{Zeeman} \ll k_B T) \tag{2.10}$$

Equation 2.10 implies that the system has a net magnetization that is aligned with the field. NMR observes the behavior of the *macroscopic* (net) magnetization.

2.1.3 Rotating Field and Rabi Oscillations

A static, uniform magnetic field is what establishes the equilibrium condition of magnetic resonance experiments. In order to perturb the net magnetization away from equilibrium, a rotating field is often applied in addition to the uniform field.

Regardless of whether one solves the problem classically or quantum mechanically, the result is the same. If we apply a total field

$$\boldsymbol{H(t)} = H_o\hat{z} + H_1[\cos(\omega_z t)\hat{x} + \sin(\omega_z t)\hat{y}] \tag{2.11}$$

where H_o is the uniform field applied along $\hat{z}$ and H_1 is a field along the xy-plane rotating about $\hat{z}$ at a frequency of ω_z, the effective field in the rotating frame, F', where H_1 is static is given by

$$\boldsymbol{H_e} = \big(H_o + \frac{\omega_z}{\gamma}\big)\hat{z'} + H_1\hat{x'} \tag{2.12}$$

When the frequency of H_1 is chosen to match the resonant frequency, $\omega_z = -\gamma H_o$ and the $\hat{z}$ component of the applied field effectively vanishes. Equation 2.12 becomes

$$\boldsymbol{H}_{\boldsymbol{e\ (res)}} = H_1 \hat{x'} \tag{2.13}$$

In the rotating frame, the spins feel a static magnetic field along $\hat{x'}$ which results in the rotation of net magnetization about $\hat{x'}$ at a frequency of $\omega_1 = -\gamma H_1$. Although it may be tempting to call this a Larmor Precession, this phenomenon is actually called a *Rabi Oscillation*.

2.1.4 The Bloch Equations and Relaxation

In 1946, Felix Bloch published equations of motion combining both the thermal effect of alignment with H_o and the effects of an arbitrary alternating field H_1 on the components of net magnetization. These equations, expressed below, came to be known as the *Bloch Equations*.

$$\frac{dM_z}{dt} = \gamma(\boldsymbol{M} \times \boldsymbol{H})_z - \frac{M_z - M_o}{T_1} \tag{2.14}$$

$$\frac{dM_x}{dt} = \gamma(\boldsymbol{M} \times \boldsymbol{H})_x - \frac{M_x}{T_2} \tag{2.15}$$

$$\frac{dM_y}{dt} = \gamma(\boldsymbol{M} \times \boldsymbol{H})_y - \frac{M_y}{T_2} \tag{2.16}$$

Here, M_o is equal to the net magnetization along $\hat{z}$ when the system is in thermal equilibrium. $\boldsymbol{H}$ need not be restricted to applied fields and can include interactions. Exactly how to solve these equations and which limits to apply depends on the measurement being taken and the specifics of the experiment. Regardless of the situation, the expected behavior of the magnetization in the lab frame can be summarized like so: After perturbation, the moment will gradually return to full alignment with $\boldsymbol{B_o}$ while also precessing about $\boldsymbol{B_o}$ at a frequency of $\omega = -\gamma B_o$. This behavior is illustrated in Fig. 2.3.

Bloch also introduced constants, T_1 and T_2, which represent the *longitudinal* or *spin-lattice* relaxation time and *transverse* or *spin-spin* relaxation time of the magnetization, respectively.

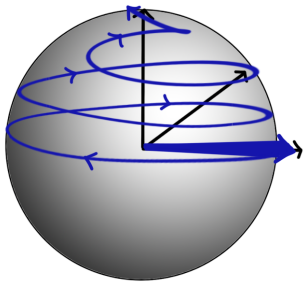

Figure 2.3: Trajectory of magnetization after perturbation.

(Spin-Lattice Relaxation) T_1: a measure of the time it takes the magnetization to return to thermal equilibrium from a perturbed position. T_1 relaxation, by definition, is not energy conserving. This type of relaxation requires coupling to a thermal reservoir that is ready to absorb or emit the energy required for transitions between different spin states.

(Spin-Spin Relaxation) T_2: a measure of the time it takes for the xy-component of the magnetization to vanish. Unlike T_1 relaxation, T_2 relaxation does not require coupling to a thermal reservoir. The transverse magnetization often vanishes long before full relaxation of the longitudinal component due to field inhomogeneities as well as spin decoherence. Field inhomogeneity causes a reversible "spreading" of the spins along the xy-plane due to a distribution of resonance frequencies. On the other hand, spin decoherence is a result of spin flopping and other transitions in the spin states that are irreversible. In experiment, the observed decay rate of the NMR signal is denoted as T_2^*, which includes decay from both inhomogeneous spreading and decoherence. T_2 is reserved for irreversible spin decoherence processes.

2.2 Dominant Interactions

The energy levels of each individual spin are determined by the total *local* magnetic field felt by the spin. In general, the Hamiltonian for a single spin includes interaction with the applied field, $\boldsymbol{H_o}$, the field from nearby nuclei, $\boldsymbol{H}_n$, the field from nearby electrons, $\boldsymbol{H}_e$, and

the quadrupole moment, $\mathcal{H}_Q$, for any nuclei with $s > \frac{1}{2}$.

$$\mathcal{H} = \mathcal{H}_o + \mathcal{H}_{\text{int}} + \mathcal{H}_Q \tag{2.17}$$

$$= -\boldsymbol{\mu_s} \cdot (\boldsymbol{H_o} + \boldsymbol{H}_{\text{int}}) + \mathcal{H}_Q \tag{2.18}$$

$$= -\boldsymbol{\mu_s} \cdot (\boldsymbol{H_o} + \boldsymbol{H_e} + \boldsymbol{H_n}) + \mathcal{H}_Q \tag{2.19}$$

This dissertation only includes measurements probing ^1H and ^{13}C, both of which have spin $\frac{1}{2}$, therefore $\mathcal{H}_Q = 0$ and will no longer be considered.

Nuclear spins interact, typically, as a result of direct dipolar coupling. On the other hand, they interact with electrons indirectly through hyperfine coupling. Any proper attempt to solve for the energy levels of the spins generally treats the interactions as a perturbation to the Zeeman Hamiltonian ($\mathcal{H}_o$). This approach is called the *Secular Approximation*.

2.2.1 Dipolar Coupling

Dipolar coupling is the interaction of a nuclear moment with the magnetic field produced by another nuclear moment some distance, r, away. Basic electromagnetism dictates that the Hamiltonian representing this interaction is

$$\mathcal{H}_{\text{dip}} = -\boldsymbol{\mu_i} \cdot \boldsymbol{H_j}(\boldsymbol{r_{ij}}) \tag{2.20}$$

$$= \frac{\gamma_i \gamma_j}{4\pi} \frac{\boldsymbol{S_i} \cdot \boldsymbol{S_j} - 3(\boldsymbol{S_i} \cdot \hat{\boldsymbol{r}}_{\boldsymbol{ij}})(\boldsymbol{S_j} \cdot \hat{\boldsymbol{r}}_{\boldsymbol{ij}})}{r_{ij}^3} \tag{2.21}$$

where the subscripts i and j represent the values for nucleus i and nucleus j respectively. Between like nuclei, dipolar coupling results in broadening or splitting of the spectrum. Under the secular approximation, a splitting of order

$$D_{ij} \sim \frac{\gamma_i \gamma_j \hbar}{4\pi r^3} (3\cos^2\theta - 1) \tag{2.22}$$

is expected where θ is the angle between the vector $\boldsymbol{r}$ connecting the two nuclear spins and the magnetic field $\boldsymbol{B_o}$.

2.2.2 Hyperfine Coupling

Hyperfine coupling is the interaction between a nuclear spin and an electron spin. The complete Hamiltonian is shown below.

$$\mathcal{H}_{\text{hf}} = \left[\frac{\boldsymbol{\mu_S} \cdot \boldsymbol{\mu_L}}{4\pi r^3}\right] + \left[\frac{\boldsymbol{\mu_S} \cdot \boldsymbol{\mu_I} - 3(\boldsymbol{\mu_S} \cdot \hat{\boldsymbol{r}})(\boldsymbol{\mu_I} \cdot \hat{\boldsymbol{r}})}{4\pi r^3}\right] - \left[\frac{2}{3}\boldsymbol{\mu_S} \cdot \boldsymbol{\mu_I}\delta(r)\right] \tag{2.23}$$

Orbital Term: The first term represents the coupling between the nuclear spin moment $\boldsymbol{\mu_S}$, and the electron moment due to its orbital angular momentum, $\boldsymbol{\mu_L}$. In a crystal, the orbital motion of electrons is typically quenched until application of a field [63]. Once a field is applied, the orbital term results in a shift of the magnetic resonance frequency that scales with the applied field, known as the *chemical shift*.

Anisotropic Term: The second term is the dipolar interaction between the nuclear spin and an electron spin, $\boldsymbol{I}$. All contributions from the electron wavefunction which do not sit exactly at the site of the nucleus are included here. In NMR, this term typically leads to an orientation-dependent shift in the resonance frequency, but can evolve into splitting or broadening of the spectra at lower temperatures.

Isotropic Term: The last term in the Hamiltonian is necessary for s-orbital electrons whose wavefunctions allow for the possibility of the electron and nucleus to occupy the same position in space. This isotropic term is a correction to the previous term, which fails in the limit that $r \to 0$. The main effect is the same, except the shift is not affected by the orientation of the sample. This term is formally called the *Fermi Contact Interaction*.

The Hyperfine Shift: All three above contributions make up what is known as the *Hyperfine Shift*:

$$\Delta H/H_o = \delta = \sigma + \kappa \tag{2.24}$$

where σ represents the chemical shift from the spin-orbit coupling, and κ is the *paramagnetic shift* or Knight shift (as it is called in metals) from both the anisotropic and isotropic dipolar contributions. In solid state NMR, the Hyperfine shift is of considerable interest because it holds a direct relationship to the spin susceptibility of the material, since

$$\kappa = \langle A \rangle \chi_s \tag{2.25}$$

where $\langle A \rangle$ is the hyperfine coupling constant and is normally experimentally determined for a specific crystal orientation.

2.3 Pulsed NMR Spectroscopy

2.3.1 Technique

The technique used in an NMR experiment is not very different from what was explained in section 2.1. The steps for a pulsed NMR experiment are detailed below:

1. Apply a fixed, uniform magnetic field, $\boldsymbol{B_o}$, to the sample to achieve a net magnetization aligned with $\hat{z}$.

2. Send in a sequence of short, square wave *pulses* of alternating current at a precise radio frequency, ω_{RF}. The pulses do two things. First, they produce the alternating field, $\boldsymbol{B_1}$, that perturbs the magnetization to the desired orientation via Rabi Oscillation. A pulse which rotates the magnetization 90^o is called a "$\pi/2$-pulse", while a pulse which rotates 180^o is called a "π-pulse". Square waves excite a *range* of transitions about energy $\hbar\omega_{RF}$. The bandwidth (BW) of excitation is equal to the inverse of the pulse length, τ_P.
$$\text{Pulse BW} = \frac{\hbar}{\tau_P} \tag{2.26}$$

3. Detect and record the induced Electromotive Force (EMF) from the relaxing magnetization. This is considered the raw, real time NMR signal and is often further processed to analyze spectra in the frequency domain, T_1, T_2, or any other relevant observable.

2.3.2 NMR Spectrum

The NMR spectrum is obtained via a Fast Fourier Transform (FFT) of the real time signal. The real time signal is proportional to the time varying transverse net magnetization of the sample after a pulse. For spin-1/2 systems, it is easiest to consider the NMR spectrum a histogram of the resonance conditions felt by each individual spin in the system.

In general, the real time NMR signal produced by a group of spins with a *single* resonance frequency, ω_i, relaxing from the xy-plane is expected to produce a signal of the form

$$S_i(t) = S_{io} \exp[i(\omega_i - \omega_{REF})t] \exp(-t/T_2) \tag{2.27}$$

where S_{io} represents the weight of the spins with resonance frequency ω_i relative to spins with other resonance conditions. ω_{REF} is the frequency generated by the source and is also referred to as the reference frequency. Applying a Fourier transform to the real time signal yields

$$\mathrm{Re}[S_i(\omega)] = S_{io} \frac{1/T_2}{(1/T_2)^2 + [(\omega_i - \omega_{REF}) - \omega]^2} \tag{2.28}$$

which is a Lorentzian centered about the difference between the resonance and reference frequencies. The real part FT of magnetization is referred to as the "absorption" Lorentzian. The full width half maximum (FWHM) of the *homogeneously broadened* peak is given by

$$\mathrm{FWHM} = \frac{1}{\pi T_2} \tag{2.29}$$

A homogeneously broadened peak implies that the linewidth of the peak is not due to an inhomogeneous distribution of magnetic fields in the sample, which would result in a distribution of resonance frequencies. In a solid, a T_2 dominated linewidth is on the kHz scale.

In most solids, however, the NMR peaks are *inhomogeneously broadened*. Instead of a Lorentzian shape, the peak takes on the shape of a Gaussian (or something else) corresponding to the distribution of local magnetic fields. In this case, T_2 is replaced by T_2^* in Eqs. 2.27-2.29, which includes the loss of spin along the xy-plane due to inhomogeneous spreading as well as decoherence.

2.3.3 T_1 Measurements

The most simple T_1 measurement involves applying what is called an FID pulse sequence: $\frac{\pi}{2} - \tau -$ ACQUIRE. This pulse sequence first perturbs the net magnetization onto the xy-plane, waits some time τ, and then measures $M_z(\tau)$. For a spin starting on the xy-plane,

the Bloch equations predict

$$M_z(\tau) = M_o[1 - \exp(-\tau/T_1)] \tag{2.30}$$

By measuring $M_z(\tau)$ at several different τ values, one can obtain a complete recovery curve which can then be used to extract T_1.

2.3.4 T_2 Measurements

A measurement of the T_2 constant due to irreversible processes requires a spin-echo sequence: $\frac{\pi}{2} - \tau - \beta - \tau -$ ACQUIRE. The spin-echo sequence brings the magnetization to the xy-plane, allows spreading of the spin due to field inhomogeneity, reverses the spreading, and then measures the net magnetization along the xy-plane. The pulse length, β, required for maximal reversal of spreading depends on the details of the experiment. Even with full reversal, the magnetization is still expected to decay exponentially to zero over time due to irreversible processes. The decaying magnetization due to T_2 processes can be expressed by

$$M_\perp(2\tau) = M_o \exp(-2\tau/T_2) \tag{2.31}$$

2.4 Experimental Setup

Magnet:

All NMR experiments utilize a magnet to supply the uniform, homogenous magnetic field, $\boldsymbol{B_o}$. The magnet is often superconducting and has a bore large enough to house an entire probe as well as a cryostat for temperature control.

Transmitter:

The transmitter generates and processes the wave that will act as $\boldsymbol{B_1}$. The components of a transmitter are listed below.

1. A frequency *generator* or *synthesizer* produces a continuous wave at a well defined frequency. The frequency is easily tuned in an NMR experiment.

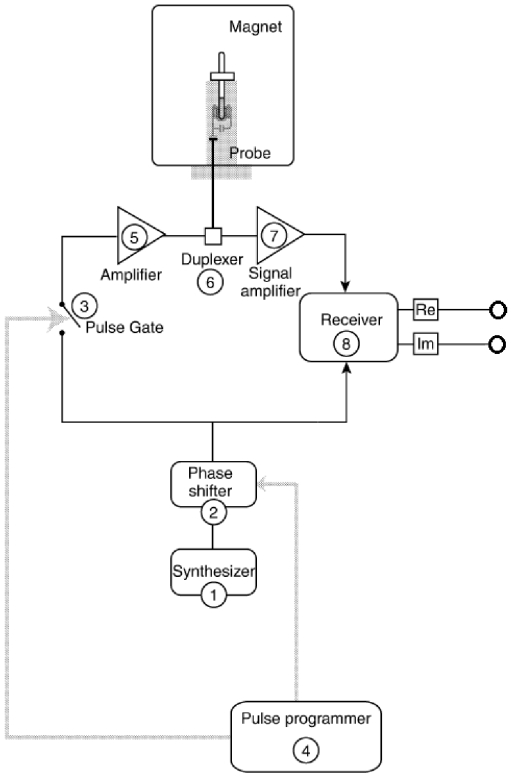

Figure 2.4: (a) Schematic of a Pulsed NMR Experiment. Figure from [64].

2. In a pulsed NMR experiment, the wave is then sent through a *phase shifter*, where its phase is changed in order to suit experiment needs. From the phase shifter, it passes trough a *pulse gate*, controlled by a *pulse programmer*, where it is transformed into short pulses.

3. An *amplifier* adjusts the the power of the wave before it is sent to a duplexer.

Duplexer:

In a normal setup, the transmitted wave and returning signal travel through the same line. This is a problem, because the strength of the transmitted wave is drastically larger than that of the signal and would overpower the signal if not removed before reaching the receiver. The purpose of the *duplexer* is to direct the transmitted wave into the sample space and ensure that only the resonance response from the sample enters the receiver.

Probe:

The probe houses the sample and ensures that it sits at the center of the magnet, where the field is most uniform. The probe also makes up the bulk of the resonance circuit. The resonance circuit is a transmission line, composed of resistors, an inductor, and a capacitor, tuned to have the same resonance, $\gamma_n B_o$, as the nucleus to be probed. The sample is located inside the inductance coil which doubles as the solenoid carrying the transmitted alternating RF current. The current in the coil produces the $\boldsymbol{B_1}$ required for perturbation of the magnetization and the coil is oriented such that $\boldsymbol{B_1} \perp \boldsymbol{B_o}$. The same coil also detects the induced electromotive force (EMF) from the changing magnetization in the sample.

Receiver:

Once a resonance condition has been met and the response signal has been properly routed by the duplexer, the signal is sent, first, to an amplifier and then to a *quadrature receiver*. All modern day experimentalists process and analyze their data digitally. This requires the signal to go through an *analogue-to-digital* (ADC) converter. However, because the real time NMR signal is oscillating at frequencies on the hundreds of MHz scale, ADC converters cannot keep up. The quadrature receiver mixes the sample signal with the reference wave (fed in by the generator) and returns a signal with frequency equal to the difference between the two, $\omega_{\text{new}} = \omega_o - \omega_{\text{RF}}$. The receiver also splits the signal into an in-phase (real) component and 90^o out-of-phase (imaginary) component.

CHAPTER 3

Effects of Impurity Spins on Low-T Behavior of κ-HgCl

It was mentioned in sections 1.1 and 1.3.5.3 that there is considerable interest in the interplay of charge degrees of freedom and magnetic degrees of freedom in κ-$(ET)_2X$ materials. Comparison of κ-CuCN and κ-CuCl reveal that exchange interaction, J, and dimerization strength, t_d/t, are not enough to explain differences in magnetic behavior as κ-CuCN is a QSL candidate and κ-CuCl is antiferromagnetic below $T = 26$ K despite having similar J and t_d/t [11, 65]. Thus, it became necessary to look for other factors, including frustration and how charge degrees of freedom might affect it. κ-HgCl and κ-HgBr emerged as prime materials for the study of such interactions. With dimerization strengths weaker than other κ-$(ET)_2X$ materials, these two compounds have a stronger tendency toward charge order [11, 58, 66].

This chapter of the dissertation covers ^1H NMR experiments performed on κ-HgCl. At the time the experiments were done, a lot was known about the charge degrees of freedom of κ-HgCl, including a CO MIT at $T \approx 30$ K and an inter-dimer charge disproportionation $\delta = 0.2e$ [39, 58], while information on the magnetic degrees of freedom was lacking.

The conclusion from this study is that there is no signature for magnetic order in this material down to as low as 25 mK, as evidenced by a roughly temperature independent NMR spectrum. This is in contrast to a previously proposed AFM transition at $T_{AFM} = 27$ K [34]. $1/T_1T$ measurements confirm a MIT at T_{CO}, and the $1/T_1$ behavior is qualitatively similar to those of current κ-$(ET)_2X$ QSL candidates such as κ-CuCN and κ-AgCN. However, instead of interpreting the power law behavior of $1/T_1$ vs T as evidence of gapless spin excitations as with the case for κ-CuCN and κ-AgCN, the possibility of a low T response due to proton

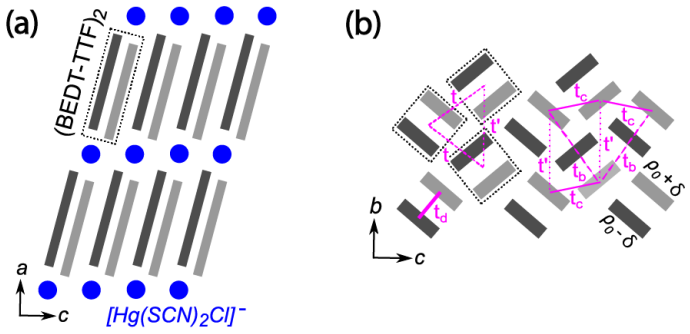

Figure 3.1: (a) Illustration of layered structure along the a axis of κ-(BEDT-TTF)$_2$Hg(SCN)$_2$Cl. Alternating layers of (BEDT-TTF)$_2^+$ molecules (grayscale) stacked side by side and [Hg(SCN)$_2$Cl]$^-$ anion sheets (blue). (b) Along the b/c conducting plane, BEDT-TTF molecules form a triangular lattice. Important transfer integrals, t, are marked for reference.

dipolar coupling to S=1/2, g=2 spin degrees of freedom is considered. Subsequent arguments are made to support the theory of impurity-spin dominated low-temperature relaxation.

3.1 Methods

κ-(BEDT-TTF)$_2$Hg(SCN)$_2$Cl single crystals with typical dimensions of $1 \times 0.5 \times 0.3$ mm^3 were grown by electrochemical methods reported in previous studies of the material [58]. NMR experiments were performed with custom made spectrometers used in conjunction with a superconducting, Oxford Instruments magnet with the ability to vary field between 0 T and 12 T. For sample 1, measurements were taken at a fixed frequency $\nu_o = 112.575$ MHz and magnetic field $B_o = 2.6447$ T aligned close to $\mathbf{B_o} \parallel c$ (see Fig. 3.1 for crystal axes). Field dependent measurements were performed on sample 2 with the field aligned perpendicular to the plane of the crystal ($\mathbf{B_o} \parallel a$). Standard ^{4}He flow cryostats were employed above 1.6 K, whereas a ^{3}He/^{4}He dilution refrigerator was used to cool down to 25 mK. The spin-lattice relaxation rate was determined via free-induction decay following saturation, and analyzed using stretched-exponential fits.

3.2 NMR Spectra

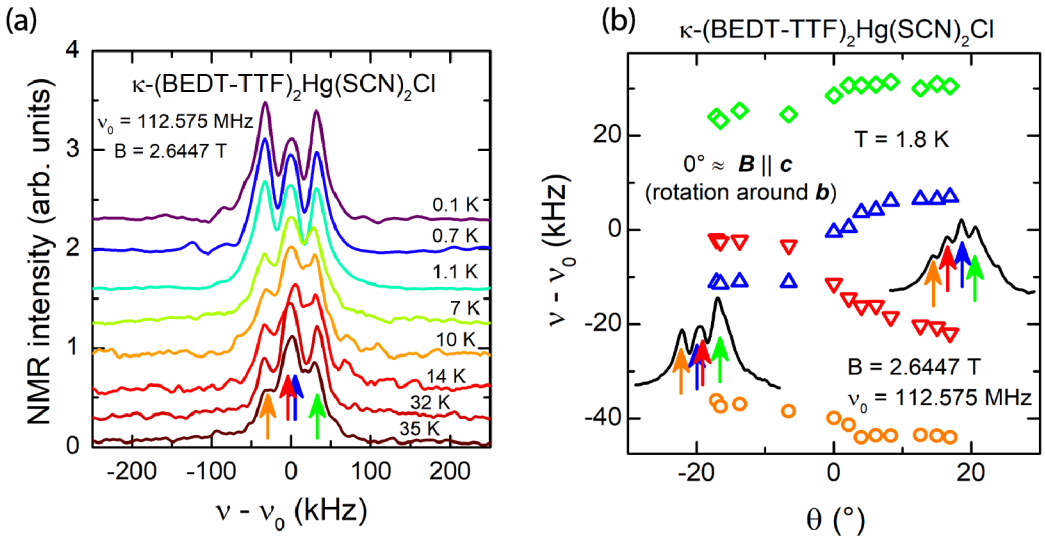

Figure 3.2: (a) Temperature dependence of ^{1}H NMR spectra for sample 1. Spectra above 2 K were obtained in a ^{4}He cryostat while temperatures below 2 K were obtained in the dilution refrigerator. A small difference in crystal orientation between setups is expected. (b) The frequency of the four resolved peaks (colored open shapes) is tracked across different angles.

The ^{1}H NMR spectra for sample 1 were taken from just above the supposed CO transition temperature $T_{CO} = 30$ K to well below 1 K. The spectral lineshape in Fig. 3.2 (a) consists of four distinct peaks, three of which are visible at the angle measured. Angle dependent measurements of the spectrum is plotted in Fig. 3.2 (b). Given the amount of inequivalent protons in the EEGs, the expected number of peaks is actually eight. However, the smallest splitting (which would turn four peaks into eight) is too small to be resolved. No significant change in the lineshape is observed upon cooling below T_{CO}. Should a phase transition into a magnetically ordered state occur, specifically AFM, obvious splitting of the peaks, like that shown in Fig. 3.3, would be observed. Thus, the NMR spectra of κ-HgCl show no indications of magnetic order throughout the CO phase.

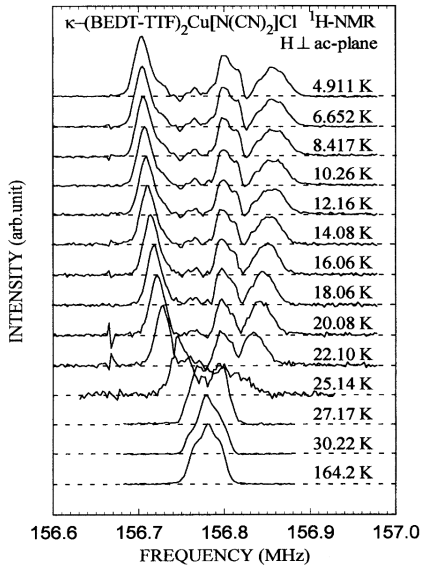

Figure 3.3: Temperature dependence of ^{1}H NMR spectra for κ-(BEDT-TTF)$_2$Cu[N(CN)$_2$]Cl. Very obvious splitting of the lineshape upon transition into an AFM state is seen between 27 K and 25 K. Figure borrowed from [65].

3.3 Spin-Lattice Relaxation

3.3.1 $1/T_1T$ vs T

In NMR, $1/T_1T$ is often used to gauge the dynamic spin susceptibility of a material. For paramagnetic materials, $\chi \propto 1/T_1T$, and in fermi-liquids, or metals, this quantity is expected to be constant. The latter is a well known phenomenon called Korringa Relaxation [63].

$1/T_1T$ measurements for sample 1 plotted across temperature reveals temperature independent behavior above $T \approx 30$ K, and an abrupt, discontinuous jump right at 30 K. At the jump, the energy scale changes from the fermi energy scale, $E_F \sim 10^3 - 10^4$ K, to the exchange interaction energy, $J \sim 10^2$ K, of the insulating state. Overall, the $1/T_1T$ behavior shown confirms a metal insulator transition (MIT) at $T_{CO} \approx 30$ K.

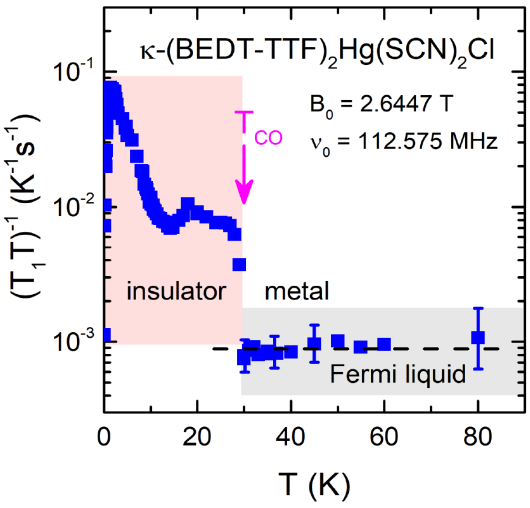

Figure 3.4: $1/T_1T$ measurements for sample 1 vs. temperature.

3.3.2 $1/T_1$ vs T

The behavior of κ-HgCl below the transition temperature is examined in further detail via typical $1/T_1$ vs temperature plots. In Fig. 3.5 (a), $1/T_1$ is roughly constant immediately below T_{CO} before it begins to fall off at 20 K. At $T \sim 10$ K, $1/T_1$ rises again peaking at $T \sim 5$ K and then falling off indefinitely. Below 5 K, the fall off is predominantly Arrhenius, obeying a $1/T_1 \propto e^{-\Delta/k_BT}$ relationship. However, at temperatures much below 1 K, it deviates from activated behavior to a power law relationship. Along the entire temperature range measured, the exponential spin-lattice relaxation becomes increasingly stretched (described by $e^{(-t/T_1)^\alpha}$), down to a value of $\alpha \approx 0.6$.

The most notable characteristic of the κ-HgCl relaxation is its remarkable resemblance to the relaxation of other κ-$(ET)_2X$ materials, specifically ones considered QSL candidates like κ-CuCN (see Fig. 1.11 (a) for an example). In those materials, the low-temperature power law behavior has been attributed to a gapless continuum of spin excitations [11, 51, 53, 67]. However, there is enough evidence in the κ-HgCl measurements to show that the low-temperature relaxation behavior can be attributed to something else: dipolar coupling of the protons to localized S=1/2, g=2 spin degrees of freedom originating from impurities. Low-temperature effects from disorder-induced spin defects has been considered before in

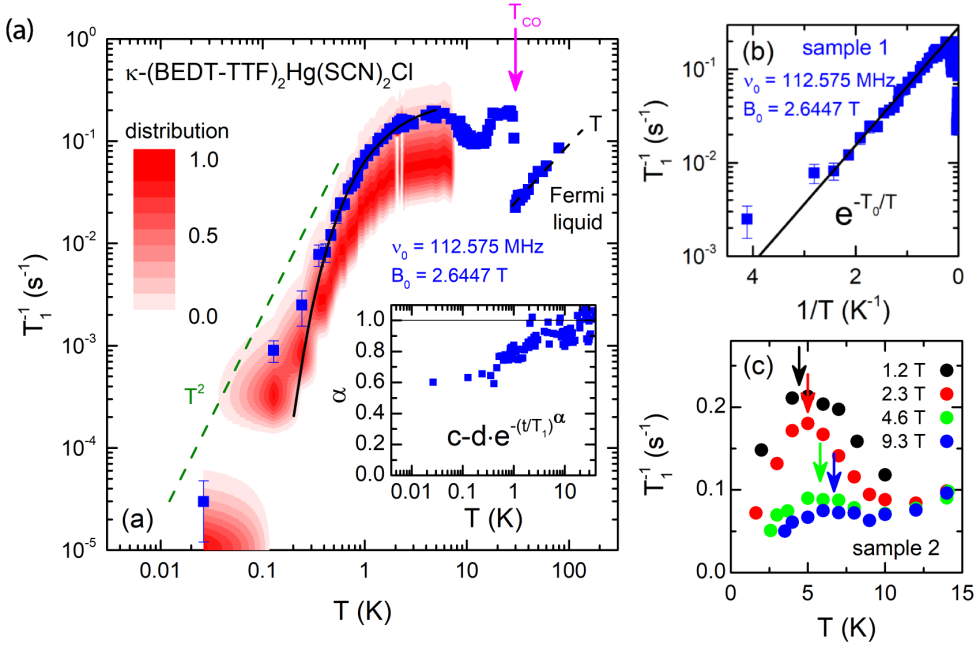

Figure 3.5: (a) $1/T_1$ measurements for sample 1 vs. temperature plotted on a log-log scale. Inlet, as well as red distribution map, plots the stretched exponential constant, α, across temperature. (b) $1/T_1$ plotted against $1/T$ on a log-lin scale to show partial Arrhenius behavior below 5 K. (c) Field dependence of $1/T_1$ in the temperature range about the peak. Field dependent measurements were performed on sample 2.

Ref. [44].

The nuclear relaxation by dipolar coupling to magnetic impurities implies certain behaviors that can be compared to experiment. For example, $1/T_1$ of κ-AgCN is strongly reduced with increasing B_o [67]; similar behavior is seen for κ-HgCl in Fig. 3.5 (c). Here, the field dependence is pronounced at temperatures close to the 5 K maximum while the relaxation for $T \simeq 10$ K remains rather unaffected. At a semiquantitative level, this is precisely the temperature range corresponding to the Zeeman energy of a free spin. More specifically, the peak and low-temperature suppression of $1/T_1$ is modeled for a single proton as

$$\frac{1}{T_1} = \frac{2}{5}\mu_o^2\gamma_S^2\gamma_I^2\hbar^2[S(S+1)]r^{-6}\frac{\tau}{1+\omega^2\tau^2} \tag{3.1}$$

where $1/\tau$ is the bandwidth of longitudinal field fluctuations, taken to be of the form $\tau = \tau_o \exp\frac{E_z}{k_BT}$, and $E_z = g\mu_B S B_o$ is the Zeeman energy splitting of the impurity spin levels, using

$g = 2$ and $S = 1/2$. The activated behavior arises from the polarization of the impurity spins in the applied magnetic field. The dipolar coupling depends on the distance, r, between the impurity spin and the nuclear site. The random arrangement of the impurities is related to a distribution of local fields which results in the stretched-exponential recovery.

Looking at the plot in Fig. 3.5 (b), the behavior on the low-temperature side of the maximum closely follows the associated thermal activation with $k_B T_o \approx \mu_B B_o$ down to 0.2 K. The peak value in Fig. 3.5 (c) roughly follows the expected $(1/T_1)_{\max} \propto 1/B_o$ dependence, and $\tau = \omega^{-1}$ at the maximum yields τ_o in the nanosecond range, in agreement with the EPR linewidth $\Delta H \approx 3$ mT in the insulating state [58]. Plugging this into Eq. 3.1, together with the experimental values of $1/T_1$, yields $r \approx 6 - 7$ nm.

Using susceptibility measurements obtained via EPR [58], the impurity concentration in κ-HgCl can be estimated via extrapolation of the Curie constant. In Fig. 3.6, χ_{EPR}, originally plotted in arbitrary units, is scaled such that χ at higher temperatures matches that of κ-CuCN. From the Curie law, $C = \chi T$, $C_{\text{mol}} = 0.006$ emuK/mol is extrapolated. A more detailed version of the Curie law,

$$C = \frac{\mu_o \mu_B^2}{3k_B} N g^2 (S(S+1)) = \chi T \tag{3.2}$$

allows extrapolation of the impurity concentration

$$N = \frac{k_B C_{\text{mol}}}{\mu_o \mu_B^2 N_A} \tag{3.3}$$

Assuming a unit cell volume $V_{UC} = 3500$ Å^3 [39], an impurity concentration of order 10^{-2} per unit cell is obtained, implying r is of order a few nm. This value agrees with r estimated from the $1/T_1$ measurement.

3.4 Comparison with other κ-$(ET)_2X$

In Fig. 3.7, $1/T_1$ of κ-HgCl is compared with κ-$(ET)_2X$ QSL candidates κ-CuCN [11] and κ-AgCN [67] on common scales and across varying B_o as indicated. Although occurring at different temperatures and not necessarily of the same origin, all of these compounds have

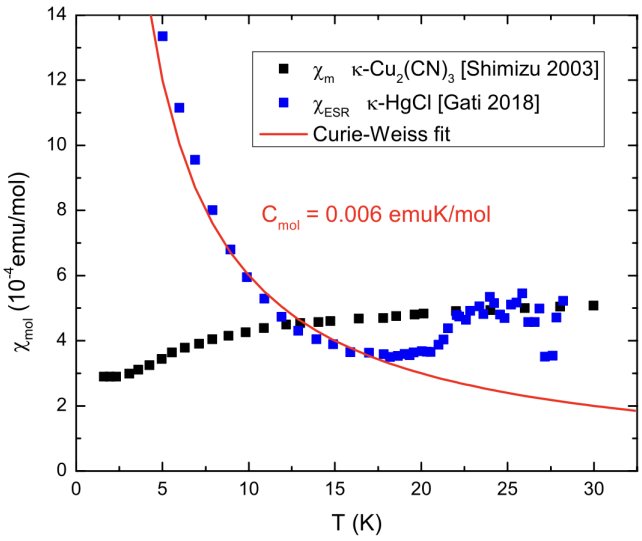

Figure 3.6: The absolute values of the spin susceptibility of κ-(BEDT-TTF)$_2$Cu[N(CN)$_2$]Cl (determined by EPR measurements in Ref. [58]) was approximated by $\chi_{\rm mol}$ of κ-(BEDT-TTF)$_2$Cu$_2$(CN)$_3$ [11].

a dynamic contribution with similar characteristics as that elaborated above for κ-HgCl. Above the low-temperature maximum, 10 K $\leq T \leq$ 30 K, the data are similar in magnitude. In the case of κ-CuCN and κ-AgCN, the behavior is attributed to gapless spinons. Generally, however, the quantitative similarity across compounds is not surprising considering they all have comparable exchange energies. Because the low-temperature relaxation is dominated by the dynamic maximum, no clear conclusion on whether or not there is a spin gap can be made. High field experiments, which will be discussed in later chapters, could possibly disclose the intrinsic magnetic properties.

The overall suppression of the $g = 2$, $S = 1/2$ peak with increasing B_o is similar for κ-HgCl and κ-AgCN as summarized in Figs. 3.7 (b) and (d). The published $1/T_1$ [67] on ^{1}H and ^{13}C (after renormalization of the gyromagnetic ratios and local charge density) show pronounced field dependence around the maximum, while the intrinsic response at higher T remains unaffected. A similar feature is also seen in the magnetic susceptibility: χT is plotted in the insets of 3.7 (b) and (c) in order to compare with $1/T_1$ [58, 68]. Similar to κ-HgCl and κ-AgCN, the ^{1}H and ^{1}3C data of κ-CuCN acquired at 2 and 8.5 T [11, 51],

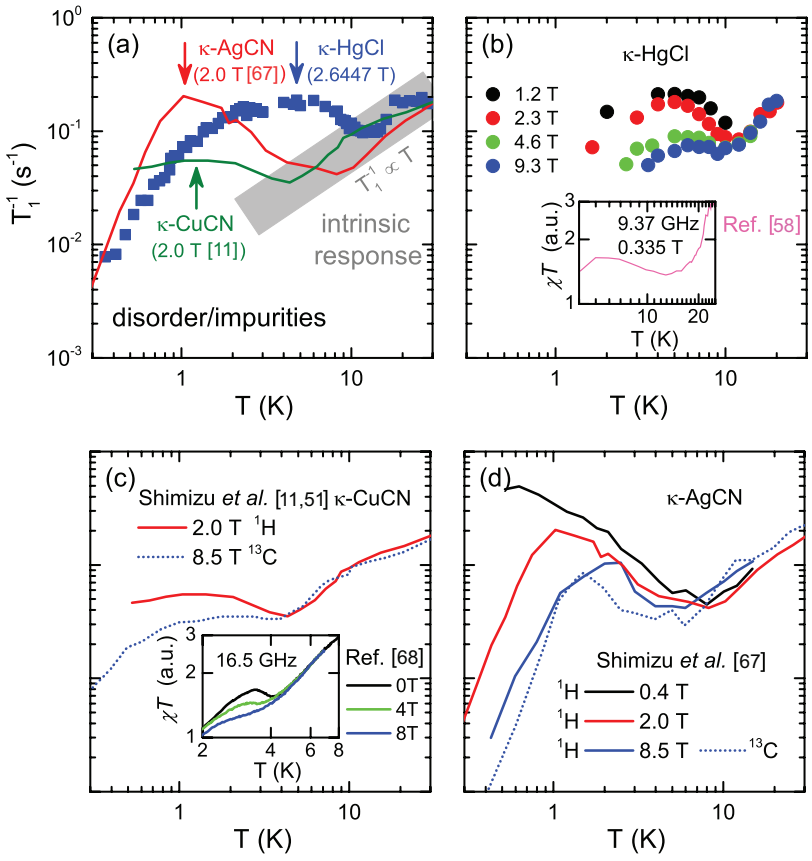

Figure 3.7: (a) ^{1}H $1/T_1$ data in the insulating state of κ-HgCl plotted alongside paradigmatic QSL candidates κ-CuCN and κ-AgCN. Here, $1/T_1$ in the shaded region follows a field-independent approximately linear T dependence suggesting that this is the intrinsic response with $J/k_B \approx 200$ K. (b)–(d) While peaked at different $T_{\rm max}$, the low-temperature contribution exhibits a similar suppression with higher B_o for all three compounds; ^{13}C data (scaled by γ_n) match well with the ^{1}H results acquired at the same B_o [11, 51, 67]. A similar field-dependent contribution is observed in high-frequency susceptibility data plotted as χT (inset of (b) at 9.37 GHz [58]; inset of (c) at 16.5 GHz [68]).

respectively, coincide above 4 K but deviate near the maximum at lower T (Fig. 3.7 (c), where appreciable field dependence is also seen by different probes [68–70]. Due to the lack of consistent $1/T_1(T)$ data upon varying B_o, other contributions below 4 K cannot be excluded in κ-CuCN.

Even though the NMR characteristics of κ-HgCl resemble the response of various QSL

candidates in minute detail, its thermodynamic properties clearly indicate the absence of itinerant spin and charge excitations. That is, extrapolating C/T down to $T = 0$ yields a Sommerfield coefficient indistinguishable from zero [62], much smaller than that of κ-CuCN and κ-AgCN where $\gamma \approx 10 - 20$ mJ/K^{2}mol [49, 67]. Note that the sister compound κ-HgBr, for which fluctuating CO has been suggested [62], exhibits γ comparable to the QSL candidates, and will be discussed next chapter. Thus, the reduced entropy in κ-HgCl is consistent with gapped charge and spin degrees of freedom (for instance if the latter resulted from a valence bond solid state below 20 K). Similar to κ-CuCN [49], C_p/T from Ref. [62] reveals a Schottky-like increase towards lower temperatures observed at a few hundred mK, coincident with the power law in $1/T_1$. It remains to be elucidated to what extent disorder is relevant for the material under study, particularly in view of the stretched exponential relaxation at low temperatures that suggests a continuum of low-energy decay channels.

It should be mentioned that a similar "hump-like" behavior in $1/T_1$ with pronounced field dependence has been seen in several disordered quantum systems [71–73] other than the κ-(ET)$_2X$ materials mentioned here. In Fig. 3.7, the absolute values and temperature of the maximum in $1/T_1$ differ from compound to compound. If the origins are similar, this could be associated with differing impurity concentrations (affecting r) as well as timescales, τ. Performing a similar dipolar relaxation for κ-CuCN and κ-AgCN as that in the previous subsection yields slightly lower impurity densities than in κ-HgCl, but of similar order of magnitude. The results are plotted in Table 3.4.

Compound	$1/T_{1_{min}}$ (1/s)	C (emu*K/mol)	V_{cell} ($\AA^3$)	N (per unit cell)
κ-Hg-Cl	0.1	0.006	3500 [39]	0.016
κ-Ag-CN	0.04	0.0024	1756 [67]	0.0064
κ-Cu-CN	0.03	0.0018	1695 [31]	0.0048

Table 3.1: Impurity spin densities for $\kappa-$(BEDT-TTF)$_2$Hg(SCN)$_2$, κ-(BEDT-TTF)$_2$Cu(CN)$_3$ [31], and κ-(BEDT-TTF)$_2$Ag$_2$(CN)$_3$.

Lastly, the origin of the magnetic impurities in κ-HgCl is briefly discussed. The clear

evidence for a discontinuous phase transition at 30 K allows for the possibility of multiple CO domains and accompanying domain walls, as recently observed in $(TMTTF)_2X$ by Raman spectroscopy [74]. One possible explanation is that the impurity states are located at domain walls. If that were the case, the absence of CO in κ-CuCN and κ-AgCN would point to a different origin of the dynamic contribution, likely linked to the anion layers [75–77].

3.5 Conclusion

In this chapter, ^{1}H NMR experiments on κ-(BEDT-TTF)$_2$Hg(SCN)$_2$Cl were presented, with a focus on the low-energy spin dynamics of κ-HgCl up through the metal-insulator transition. The spin-lattice relaxation rate indicates a Fermi-liquid metal at elevated temperatures and exhibits a pronounced, discontinuous increase upon cooling through $T_{CO} = 30$ K into the charge-ordered phase. Based on the unaltered NMR spectra (Fig. 3.2) and the smooth temperature dependence of $1/T_1$ upon $T \to 0$ (Fig. 3.5), we conclude that there is an absence of long-range magnetic order. Furthermore, the magnetic response of κ-HgCl is essentially identical to other κ-$(ET)_2X$ QSL candidates [11, 51, 67], including the stretched-exponential recovery and a power-law-like tail well below 1 K as well as a pronounced maximum in $1/T_1$ (peaked around 5 K in κ-HgCl). This low-temperature contribution exhibits a strong field dependence, similar to κ-AgCN and possibly κ-CuCN, consistent with a process originating from coupling to impurity spins. Taken together, these results imply that the low-temperature NMR properties in all three of these magnetically frustrated materials [11, 51, 53, 67] are dominated by extrinsic magnetic contributions. Suppressing the dynamic relaxation channels with high fields ($B_o \geq 10$ T) may recover the intrinsic electronic response, providing a promising route to answer the question about a spin gap in the triangular systems. Given the lack of a nonzero fermionic contribution to the low-temperature specific heat [62], the case for a spin-gapped ground state, with the gap opening at $T \approx 20$ K, is stronger for κ-HgCl than it is for κ-CuCN and κ-AgCN.

CHAPTER 4

Slowing Spin Dynamics in κ-HgBr

Studying κ-HgBr can provide some additional information on how the charge degrees of freedom in κ-$(ET)_2X$ materials affect their magnetic ground state. As mentioned in the previous chapter as well as in Chapter 1, κ-HgCl and κ-HgBr both differ from other κ-$(ET)_2X$ compounds in the sense that their anion layers are mercury based instead of copper based, resulting in weaker dimerization strengths [11, 58]. A consequence of the weaker dimerization is a larger tendency toward charge order than other κ-$(ET)_2X$ materials studied thus far [66, 78]. While κ-HgCl has been confirmed to have a MIT corresponding with a CO state [39], κ-HgBr does not have any confirmed charge order. Furthermore, while the case for a gapped low-energy excitation spectrum was made for κ-HgCl in the previous chapter, thermodynamic measurements reveal κ-HgBr to have a Sommerfield coefficient $\gamma > 0$, similar to those of κ-CuCN and κ-AgCN, making it harder to argue the same for κ-HgBr.

Examining the differences between κ-HgCl and κ-HgBr may shed some light on the interaction between charge and magnetic degrees of freedom in frustrated magnets. Interestingly, in spite of the MIT and the expectation for reduced frustration from charge order [58], a proposed ground state for κ-HgBr is a gapless QSL [62], similar to that discussed for κ-CuCN and κ-AgCN. As described, a key element for stabilization of a QSL in κ-HgBr is that it emerges from a highly frustrated intermediate phase, the quantum dipole liquid (QDL) [45]. The QDL is described as an insulating phase exhibiting short-range, fluctuating charge order for $T \to 0$. In this picture, the magnetic frustration is maintained if the temporal charge correlations are sufficiently short so as to suppress an associated reduced frustration.

This chapter of the dissertation presents the results of ^{13}C NMR experiments performed

on κ-HgBr with a focus on the nature of the MIT, and the emergent low-temperature magnetic properties. The results challenge the QDL interpretation for κ-HgBr finding evidence for charge disproportionation (CD) in the ^{13}C NMR spectra at $T < T_{MI}$. On cooling to $T < 40$ K, there is enormous line broadening, i.e. an increase in full width half maximum (FWHM), which is associated with short-range magnetic correlations. Thus, the ^{13}C NMR results indicate that κ-HgBr is not a QDL, and whether the magnetic ground state is quantum disordered remains an open question. However, the findings include inhomogeneous line widths one order of magnitude greater than for κ-CuCN [51], and spin-lattice relaxation rates two orders of magnitude greater. It is proposed that both are linked to substantial exchange disorder in κ-HgBr, which results from the strongly inhomogeneous short-range CD. Since the freezing of ethylene end groups (EEG) in related κ-phase compounds occurs around $T^* \approx 60$ K [62], which is below T_{MI}, the evidence suggests that charge order is strongly affected by the associated quenched disorder.

4.1 Methods

Single crystals of κ-HgBr used in this study were synthesized by standard electrochemical method, as previously reported [79]. BEDT-TTF with the ^{13}C central atoms labeled was obtained from Aldrich. The electrolyte consisted of a mixture of $Hg(SCN)_2$ and $[P(C_6H_5)_4]Br$ in a 90/10 1,1,2-trichloroethane/ethanol solvent. As is usual, the relevant hyperfine fields are associated with 100% ^{13}C spin labeling of the two bridging central carbon sites of the BEDT-TTF molecules, see Fig. 4.1(c). A full crystal structure determination was performed (for crystals with a natural isotopic abundance) with a more complete x-ray diffraction data set and refinement than previously reported [79][1].

[1]Crystallographic data for κ-(BEDT-TTF)$_2$Hg(SCN)$_2$Cl: $C_2 2H_1 6BrHgN_2S_1 8$, $M = 1165.95$, monoclinic, space group $C2/c$, $a = 37.0923(6)$, $b = 8.32780(10)$, $c = 11.7296(1)$ Å, $V = 3623.18(10)$ Å^3. $T = 300$K, $Z = 4$, $\mu(\mathrm{MoK}_\alpha) = 6.412$ mm^{-1}, 34713 reflections measured, 50000 unique ($R_{\mathrm{int}} = 0.0296$), which were used in all calculations. The final agreement factors were $R_1 = 0.0390$, $\omega R_2 = 0.0774$, GoF = 1.025. CCDC number 2000969. These data can be obtained free of charge via www.ccdc.cam.ac.uk/data request/cif, or by emailing data request ccdc.cam.ac.uk, or by contacting The Cambridge Crystallographic Data Centre, 12 Union Road, Cambridge CB2 1EZ, UK; fax: +44 1223 336033.

NMR measurements on a crystal with approximate dimensions $1.5 \times 1.5 \times 0.10$ mm^3 were performed using a home-built homodyne spectrometer at magnetic field strengths of $B = 9.50$ T and 6.54 T, orientated parallel to the a* axis, to an uncertainty of 10°. The relaxation rates, $1/T_1$ and $1/T_2$, approach extrema when $B \parallel a^*$, thus are not expected to change significantly within the stated range of variation. A variable-temperature helium gas flow cryostat provided the necessary cooling for measurements covering the range $2\text{K} < T < 115\text{K}$.

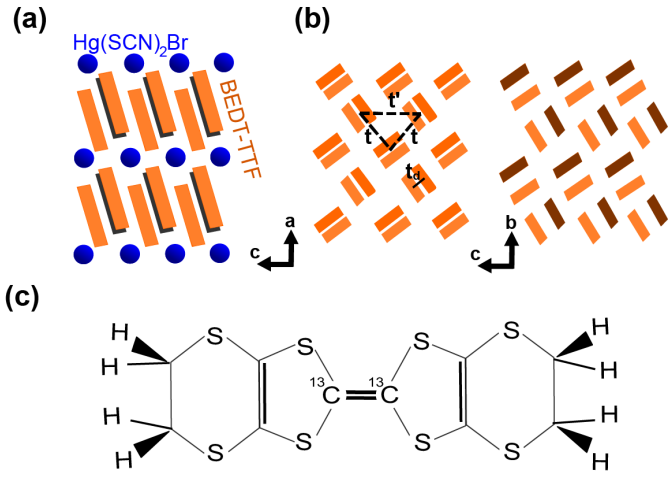

Figure 4.1: (a) Layered structure of κ-HgBr, identical to that of κ-HgCl. (b) Intralayer arrangement of cations in the bc plane with the respective transfer integrals, as indicated. While the left side depicts a strongly dimerized structure ($t_d \gg t, t'$), giving rise to Mott-insulating behavior, weakly bound dimers (right) pronounce intersite Coulomb interaction, with a tendency to charge order. Charge-rich and -poor molecules are distinguished by light and dark colors, respectively. (c) The two central carbon atoms of BEDT-TTF have been spin labeled by ^{13}C for NMR investigations.

4.2 Spin-Lattice Relaxation

As shown in Fig. 4.2 panel (c), metallic behavior with temperature-independent $1/T_1T$ occurs for $T > T_{MI}$. The discontinuous increase at $T_{\text{MIT}} = 90$ K is consistent with the previously

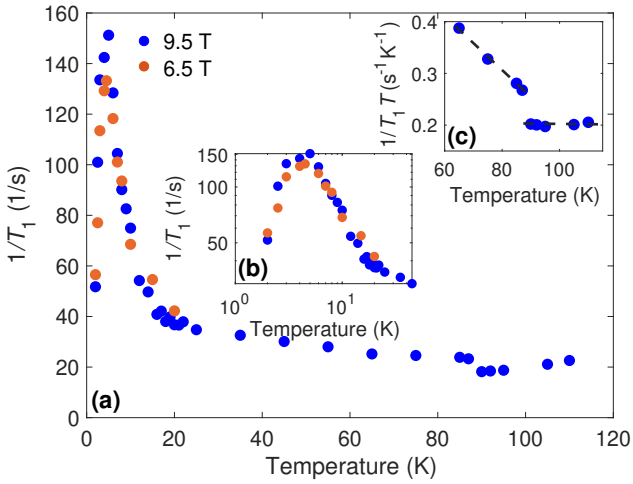

Figure 4.2: (a) The spin lattice relaxation rate, acquired at 6.5 T and 9.5 T, as a function of temperature. At higher temperatures, the pulse excitations are non-selective. However, a result of large inhomogeneous line widths and a fixed spectrometer bandwidth, the results below 40 K correspond only to the center of the spectrum. (b) The maximum in T_1^{-1} is highlighted on a logarithmic scale. (c) $(T_1T)^{-1}$ emphasizes the metal-insulator transition at $T_{\mathrm{MI}} = 90$ K.

reported first-order MIT [35, 47], very similar to the abrupt jump of $1/T_1$ seen in the last chapter in κ-HgCl when charge order sets in. Upon cooling to $T < T_{\mathrm{MI}}$, a weak temperature dependence is observed, characteristic of paramagnetic behavior. A notable increase in $1/T_1$ occurs at $T \lesssim 20$ K, forming a maximum at $T \simeq 5$ K. There are only weak variations between the two field strengths, 6.54 and 9.50 T, although some care should be taken as the pulse excitations are selective as a consequence of the increasingly large and field-dependent line widths.

4.3 NMR Spectra

While spectra in Fig. 4.3 (a) exhibit no appreciable temperature dependence in the metallic state, a small but distinct increase of the line width sets in below T_{MI} and the spectral features are seen to broaden. A much stronger inhomogeneous broadening develops below

$T = 40$ K (Fig. 4.3 (b)), in the same temperature range as the strong increase in $1/T_1$ as shown in Fig. 4.3 (c). At the lowest temperature measured here ($T = 2$ K, $B = 9.5$ T), the field-swept line width is 4320 ppm.

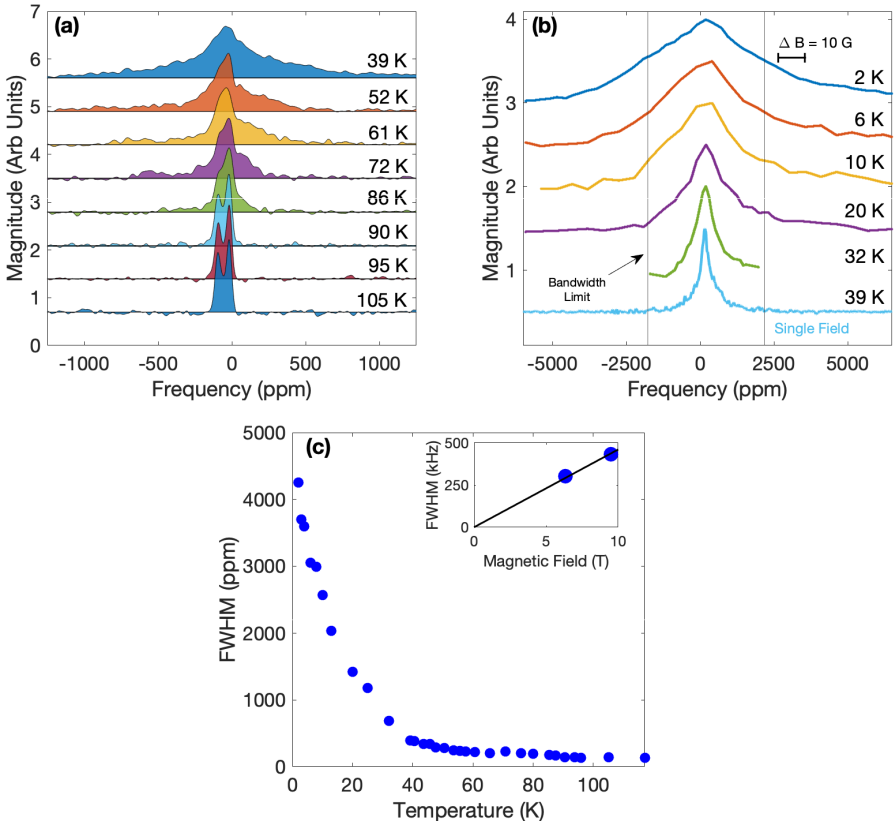

Figure 4.3: (a) Temperature-dependent evolution of ^{13}C NMR spectra at 9.5 T (101.660 MHz). (b) Due to excessive line broadening, the spectra below 39 K were acquired via magnetic field sweeps. The 39 K spectrum from single field acquisition is included for comparison. (c) Full width half maximum (FWHM) of the 9.5 T spectra as a function of temperature. FWHM were obtained from the entire, broad spectrum. Inset: Field dependence at 2 K of FWHM.

4.4 Spin-Spin Relaxation

$1/T_2$ decreases down to $T \simeq 60$ K, as shown in Fig. 4.4, and remains roughly constant down to 20 K, setting at $(1/T_2)_{\min} \simeq 0.3$ ms^{-1}. The temperature-independent $1/T_2$, combined with the considerably larger, steadily changing line widths in the insulating state, suggests the spectra are inhomogenously broadened from a distribution of hyperfine fields, which will be interpreted below as a signature of CD for $T < T_{\mathrm{MI}}$. An increase in $1/T_2$ accompanies the steep rise of $1/T_1$ below 20 K.

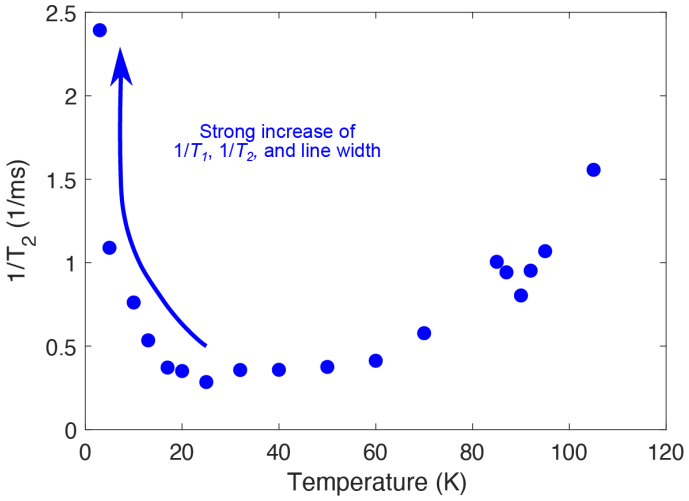

Figure 4.4: $1/T_2$ between 2.5 K and 110 K. $1/T_2$ was determined by a measure of the echo decau on varying the pulse separation. At higher temperatures, the pulse excitations are nonselective. However, as a result of large inhomogenous line widths and a fixed spectrometer bandwidth, the results below 40 K corrrespond only to the center of the spectrum.

4.5 On the NMR Collective Behavior

The behavior of the homogenous and inhomogeneous line width, as well as $1/T_1$ in the metallic regime $T > T_{\mathrm{MIT}}$, is typical of conducting (BEDT-TTF)X compounds. That is, $1/T_1T$ changes only weakly with temperature, and the decreasing $1/T_2$ upon cooling is tentatively attributed to fluctuating hyperfine fields, which are modulated by an electronic coupling to

thermally activated conformational fluctuations of the EEGs [80]. In the range 20-60 K, $1/T_2$ acquires a temperature-independent value, which is similar to that from internuclear dipolar coupling [51], indicating that the EEGs are frozen below $T \simeq 60$ K similar to related compounds [58]. An important consequence of this thermally activated process is quenched disorder in the molecular conformations (eclipsed and staggered) [81, 82], a phenomenon well known to influence the electronic properties (See Ref. [41] and references therein).

Thus it is possible for quenched conformational disorder to influence the details of a CO transition that could be underlying broken symmetry associated with the MIT. The coexistence of sharp and broad peaks that persist to $T \simeq 40$ K can be taken as evidence for a macroscopic and temperature-dependent phase segregation below a discontinuous phase transition. Note that the temperature range of metal-insulator coexistence at the first-order CO transition of α-(BEDT-TTF)I_3 is considerably extended by internal strain [83]. Disorder may have an even stronger effect on locally modulating the electronic correlation strength, thus generating a random variation of transition temperatures on the nanoscale. Some caution is warranted, however, since apart from spectra shown in Fig. 4.3 (a), there is no known independent evidence for metallic regions persisting down to $T \simeq 40$ K in κ-HgBr.

The spectral features of the inhomogeneously broadened NMR lines, due to short-range charge order on a strongly disordered lattice, are consistent with all results. It is reasonable to suggest that a broad distribution of spatial and temporal magnetic correlations is indirectly linked to the quenched structural conformations of the BEDT-TTF molecules, since the conformations first suppress long-range order in the charge disproportionation, which onsets at T_{MI}. Furthermore, note that the inhomogeneous and homogenous line broadening at low temperatures, as well as the increase in spin-lattice relaxation below $T = 20$ K, are all naturally associated with slowing of magnetic correlations, an observation consistent with the anomalous magnetic response reported in Ref. [35]. One possible explanation for why the effects are seen first in the spectra is the fact that $1/T_1$ and $1/T_2$ below 40 K measure only the spins at the center of the spectra, a consequence of large, inhomogeneous line widths. The spectra at low temperature were measured via field sweeps, and so the entire spectra

are accounted for in the FWHM measurements. The proposed charge, spin, and structural degrees of freedom of κ-HgBr upon cooling in mapped in Fig. 4.5.

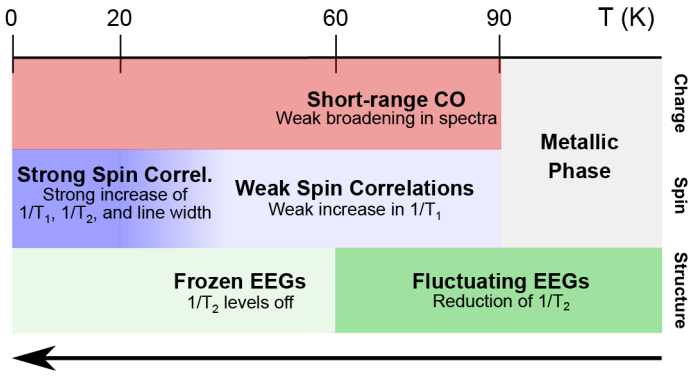

Figure 4.5: Chart of the proposed charge, spin, and structural degrees of freedom for κ-HgBr versus temperature upon cooling.

The pronounced maximum in relaxation rate at $T \simeq 5$ K is consistent with a dynamical slowing of magnetic fluctuations, which can be modeled as producing a nuclear relaxation rate given by

$$\frac{1}{T_1} \sim \gamma^2 h^2 \frac{\tau}{1 + (\omega\tau)^2} \tag{4.1}$$

where h^2 is the mean square fluctuating transverse hyperfine field, τ a temperature-dependent characteristic correlation time, and ω the nuclear Larmor frequency. Such a slowing process, when coupled with the substantial increase in the line widths, is naturally attributed to an increase in antiferromagnetic correlations.

The increase in $1/T_2$ can also be associated with the slowing of magnetic correlations. The magnitude of T_2 reveals that the ^{13}C NMR spectra remain dominated by inhomogeneous broadening. The observed FWHM at low temperatures is two orders of magnitude larger than the homogenous line width expected from $1/(\pi T_2)$. Indeed, the data presented here exhibit no sharply defined peaks, consistent with a broad onset of short-range magnetic correlations. At the lowest temperature measured, the field-swept line width (432 kHz at 9 T) corresponds to an on-site field induced moment of $\sim 0.4\mu_B$. In other words, there is strong evidence that spectral broadening below 40 K is the result of nuclear spin coupling to

field-induced and slowly fluctuating magnetic moments, possibly approaching a glassy state [47].

4.6 Discussion

In relation to the expectations for the QDL scenario, the manifestation of broad, featureless spectra in ^{13}C NMR suggests the presence of nonzero CD that is static relative to the time scale of the intrinsic homogenous line broadening associated with internuclear spin coupling, $\simeq 1$ ms or longer. If electric dipoles associated with CD were fluctuating faster than this, the spectral impact of CD would be motionally narrowed such that extensive broadening of the NMR lines would not occur. In this respect, it is not clear how to reconcile these results with the QDL state proposed for κ-HgBr in Ref. [62].

Thus, there is an apparently unresolved experimental discrepancy. The prior suggestion for the QDL state was based on a Raman study of the ν_2 intramolecular vibrational mode [62] whereby the resonance frequency is sensitive to the molecular charge of the BEDT-TTF sites [84], and therefore a probe of CD. The crucial finding was the lack of evidence for distinct molecular environment over a temperature range spanning widely on either side of T_{MI}. While it is unclear how to account for the difference, for the moment simply note that the optical spectra reported in Ref. [35] *do* provide evidence for at least two molecular environments. That is, the resolved splitting of the optically active ν_{27} vibrational mode is consistent with a finite CD of $0.13e$ [84].

For the sake of completeness, it is worthwhile to compare and contrast the observations reported here to comparable measurements of ^{13}C line broadening (FWHM), $1/T_2$, $1/T_1$ on κ-CuCN and κ-AgCN [51, 67], see Table 4.6. For each of these quantities, the values are far greater for κ-HgBr. The significance is that while the relatively small line broadening observed for κ-CuCN and κ-AgCN was reasonably attributed to a small number of magnetic impurities [51, 67], the results for κ-HgBr indicate a far greater magnetic response. When converted to an effective scale, the magnetic moment of κ-HgBris of order $0.4\mu_B$ and keeps

	κ-HgBr	κ-CuCN	κ-AgCN
${T_1^{-1}}_{max}$	150 s^{-1}	3 s^{-1}	1.5 s^{-1}
T_2^{-1}	2.5 ms^{-1}	1 ms^{-1}	
FWHM	500 kHz	50 kHz	40 kHz

Table 4.1: Comparison of ^{13}C NMR quantities for κ-HgBr, κ-CuCN and κ-AgCN [51, 67]. $1/T_2$ and FWHM are the $T \to 0$ saturated values for $B \simeq 8$ T for κ-CuCN and κ-AgCN.

increasing at the lowest temperatures.

From the very large quantitative differences in relaxation rates, as well as the line widths at comparable fields, it is natural to infer that the physical description of the low-temperature properties of κ-HgBr is likely also qualitatively different than for the QSL candidates κ-CuCN and κ-AgCN. In the present case, disorder effects are likely much more pronounced, likely related to the MIT and the resulting short-range charge order, leveraging the occurrence of microscopic imhomogenneities of the exchange interaction. While in the two related compounds, as well as in κ-HgCl, dilute impurities dominate the low-temperature relaxation consistent with a spin-gapped scenario [1], the NMR properties in κ-HgBr rule out a gap in the temperature range measured and strongly suggests fluctuations of intrinsic spin degrees of freedom. A remaining question is whether the present system exhibits a glasslike state, with substantial static moments in the absence of an applied magnetic field in the limit $T \to 0$.

4.7 Conclusion

This chapter of the dissertation presented the results of ^{13}C experiments on κ-(BEDT-TTF)$_2$Hg(SCN)$_2$Br. The spin-lattice relaxation, spectra, and spin-spin relaxation are examined in the range $T = 2 - 115$ K. The sharp increase in $1/T_1$ and $1/T_2$ for $T \lesssim 20$ K as well as large line broadening of the spectra around the same temperature range suggests slowing magnetic fluctuations. The symmetric nature of the broadening and field-dependent

linewidths indicate that the slowing is driven dominantly by antiferromagnetic correlations. At the lowest temperature measured, the field dependence of the line width indicates that the system is still in a fluctuating disordered phase and, otherwise, the evidence for slowing dynamics could be a precursor for the onset of glassy behavior at lower temperatures. Altogether, the low-temperature spin degrees of freedom in κ-HgBr are best described by short-range antiferromagnetism. It is also highly frustrated, and additionally quenched disorder results in short-range static charge disproportionation and consequently also strongly varying nearest-neighbor exchange interaction. Strong quenched disorder in the electronic structure of this insulating material is evidently associated with disordered and gapless magnetic degrees of freedom. It remains to be explored whether a glassy state is stabilized at lower temperatures. In any case, the system is unlikely a host of propagating spinons.

CHAPTER 5

Searching for a Gap in κ-CuCN

The energy spectrum of κ-CuCN has been a topic of dispute. After the discovery of its QSL properties, measurements of the low energy excitation spectrum via specific heat, susceptibility, and NMR relaxation all failed to detect a gap [11, 49, 51]. Most notably, a field-indepedent, linear term in the specific heat as $T \to 0$ K, was interpreted as the signature of a spinon fermi surface [49], and models predicting a U(1) QSL with fermionic spinons in κ-CuCN emerged [27, 28]. However, empirical support for this model is not robust. There exists opposition to the gapless interpretation due to thermal conductivity measurements which were interpreted as evidence for a small energy gap of $\Delta = 0.46$ K [50]. If κ-CuCN is, in fact, gapped, a different QSL model must be considered.

Recently, there have been debates about whether or not κ-CuCN is a QSL, with one hypothesis being that the ground state is actually a VBS [54, 57]. The hypothesis stems from an earlier study by Manna *et al.*, which showed, after proper removal of background contributions, that the specific heat, gradient of susceptibility, and in-plane expansion coefficients of κ-CuCN all exhibit a sharp peak at 6 K [55]. For a while, this study has been interpreted as experimental evidence that the 6 K anomaly in κ-CuCN is associated with both a lattice distortion as well as a second-order phase transition [85], in which case there must also be a broken symmetry involved, although the symmetry is unknown. If the second-order phase transition involves the spin degrees of freedom, then the findings are not consistent with a QSL state. In this case, the VBS, which is a singlet state associated with broken spin rotational symmetry as well as a lattice distortion, is a strong contender. However, lack of evidence for a spin gap, which is also a requisite for the VBS state, has prevented the VBS hypothesis from gaining traction.

Now that missing evidence is emerging. Recent studies have provided good reason to believe that the ground state of κ-CuCN may truly be gapped, and the proposed reason why a gap has not been before detected is because impurities dominate and mask the intrinsic low temperature response [54, 57]. In 2020, Miksch *et al.* interpreted the EPR response of κ-CuCN as the signal of two components, one with a clear gap measuring $\Delta = 12$ K, and the other presumed to be the signature of impurity/defect spins (see Fig. 5.1). In addition to that, it was shown in Chapter 3 that, while the relaxation behavior of κ-HgCl appears to be ungapped, it is possible to model the low temperature behavior as the sum of an intrinsically gapped energy spectrum and an impurity spin response. The chapter also showed that the qualitative behavior of several κ-$(ET)_2X$ QSL candidates is similar to that of κ-HgCl, suggesting similar origins.

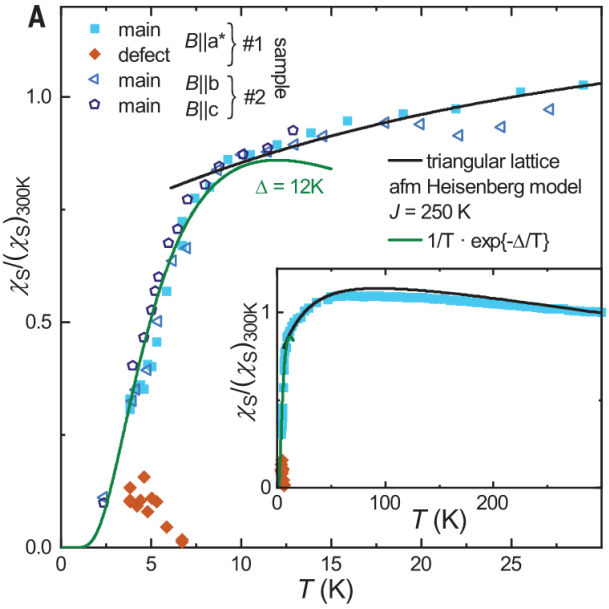

Figure 5.1: (a) Spin susceptibility extracted from the EPR spectra by Miksch *et al.* [54] shows one gapped component and a defect component which creeps in at the lower temperatures.

If the interpretations in the above two studies are correct and apply equally to κ-CuCN, high field NMR measurements would be very informative. Should the impurity spins be frozen out by sufficiently high fields, one can examine the intrinsic behavior of κ-CuCN unhindered by those spins, and possibly confirm a gapped energy spectrum. This chapter of

the dissertation presents the results of ^{13}C NMR experiments performed at high magnetic fields in light of such revelations. Conditions for frozen impurity moments are met when the Zeeman energy of the impurity spin, $E_z = g\mu_B S B_o$, is much larger than the thermal energy of the system, $k_B T$. Given that the study focuses on temperatures lower than 10 K, it was assumed that a 30 T field would be sufficient.

Remarkably, the results of this experiment show that κ-CuCN is gapped, but the gap does not appear as a result of high field. We find signatures for a gapped spectrum in fields as low as 12 T. Furthermore, the presence of a sharp peak in $1/T_1$, possibly marking the onset of a second-order phase transition, is detected. We discuss these results as well as their implications in comparison with previous measurements of ^{13}C.

5.1 Methods

^{13}C NMR data were obtained using spin-echo techniques at four different magnetic fields and were collected at two different facilities. Data taken at 6.7 T were obtained at the UCLA Brown lab using a custom made homodyne spectrometer at a frequency of 71.400 MHz. A single crystal, sample A, with dimensions approximately 2mm x 1.5mm x 0.1mm was used. Measurements at 12 T, 20 T, and 30 T (varying frequencies) were taken in the 32 T magnet at the Tallahassee NHMFL through remote collaboration with Arneil Reyes, Elizabeth Green, and Sanath Ramakrishna. A different sample, denoted sample B, with dimensions similar to sample A, was used. In all NMR experiments, the magnetic field, B_o, was oriented parallel to the a^* axis, perpendicular to the conducting plane of the crystal. Typical VTIs, which can access temperatures between 1.2 K and 300 K were used, however the experiments focused on temperatures lower than 20 K.

Numerical Inverse Laplace Transformations (ILT) were also performed on the recovery curves of κ-CuCN. The methodology and limitations of the method are detailed in Appendix A. The smoothing factor, α, was chosen to be 3, slightly larger than the average a_{opt} value of approximately 2 (see Appendix A for details on what this means). The allowed range for

$1/T_1$ consisted of $m = 150$ logarithmically spaced bins from 10^{-4} to 10^4.

5.2 Results

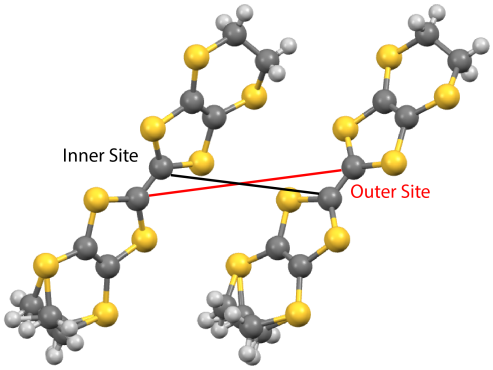

Figure 5.2: BEDT-TTF pair with the inner and outer ^{13}C atoms labeled.

Temperature dependence of the NMR spectra across four fields is plotted in Fig. 5.3. Within the $(BEDT\text{-}TTF)_2$ dimer, there are two inequivalent pairs of ^{13}C atoms, dubbed the "inner" and "outer" sites [51, 86] (See Fig. 5.2). Each pair is associated with a different hyperfine coupling constant, resulting in two peaks in the NMR spectrum. The two ^{13}C atoms in a single BEDT-TTF molecule also experience dipolar coupling bringing the expected number of peaks to four. However, the dipolar splitting is not resolvable in the temperature range covered in this experiment, and only the inner and outer peaks are visible. As the spin susceptibility drops, the distance between the peaks closes, until the two become indistinguishable at $T \sim 5$ K.

Below this temperature, the spectra begin to inhomogeneously broaden, at which point a frequency sweep is needed to obtain the full spectrum. A comparison of second moments is plotted in Fig. 5.4. Because the line shape is not Gaussian, the true relationship between the standard deviation (σ) and full width half maximum (FWHM) is not known, but a direct comparison suggests FWHM $= \sigma/2$. Except for the case of $T < 3.5$ K in 30 T, the second moment reveals that the linewidth scales linearly with field. In other words, it is

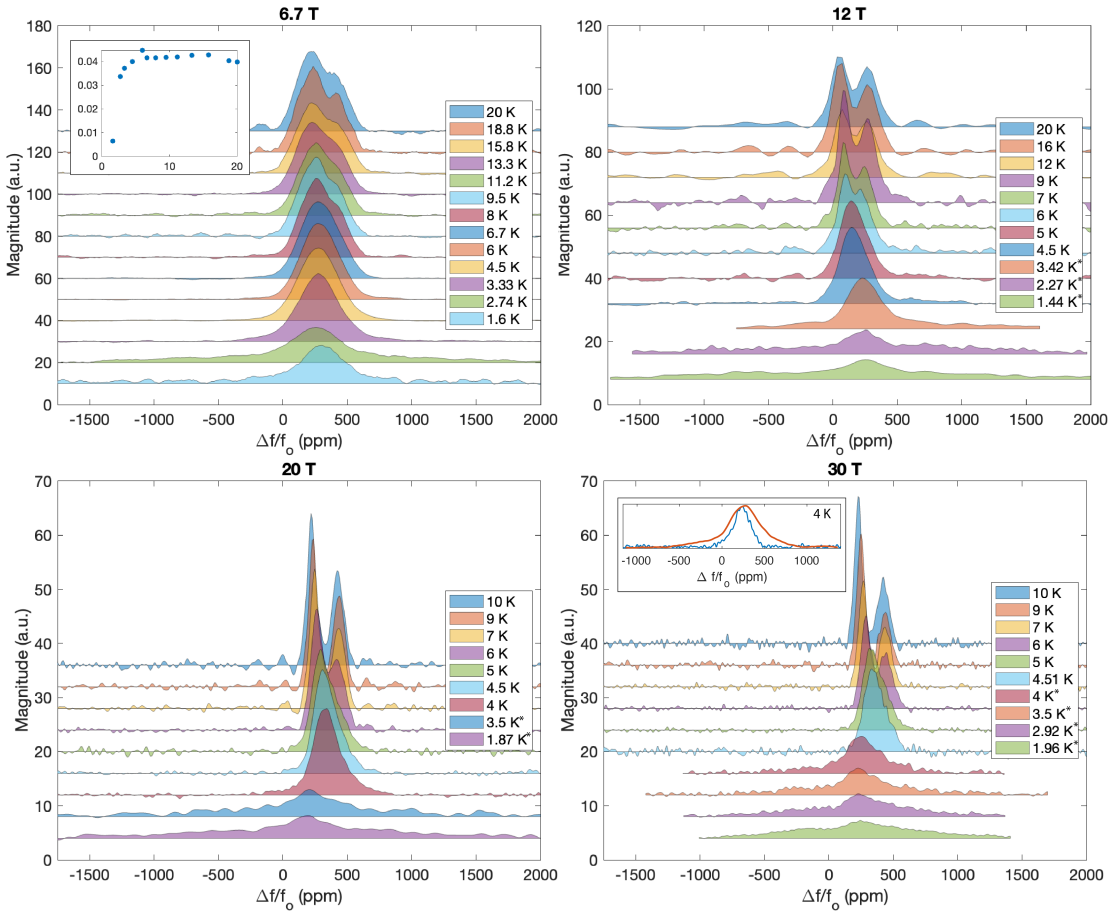

Figure 5.3: Temperature dependence of NMR spectra across four different fields. Asterisk implies spectrum obtained via frequency sweep. Sudden shifts at frequency swept temperatures likely systematic error due to field discrepancies. 6 T Inset: Spectral intensity * T vs T. 30 T Inset: Comparison of field swept spectrum and single acquisition at 4 K.

associated with inhomogeneous, paramagnetic moments. Saturation of the 30 T linewidth at a scaled value less than the other three fields can be interpreted as an indication that paramagnetic moments in the material have frozen. However, no obvious peaks in $1/T_1$ were detected (Fig. 5.5) at the temperature range in which the spins allegedly freeze, and no $1/T_2$ measurements were taken to confirm. Coincident with the onset of broadening is a spike followed by a dramatic drop in the spectral intensity of the NMR spectrum, which is plotted in the top-left inset of Fig. 5.3.

$1/T_1$ was measured from slightly above the 6 K anomaly down to as low as 1.78 K.

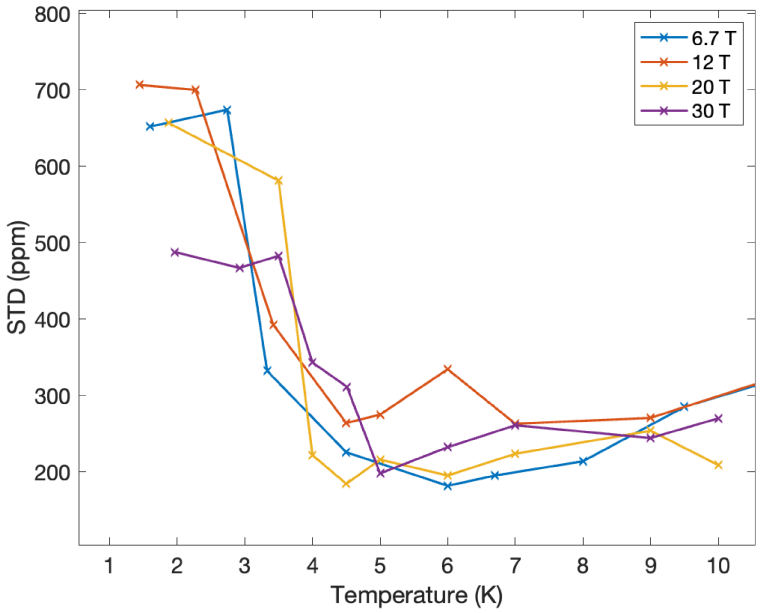

Figure 5.4: Standard deviation (STD, σ) of NMR spectra calculated from square root of the second moment.

As expected for κ-CuCN, stretched exponentials with very long relaxation times made it difficult to obtain fully relaxed saturation recovery (SR) curves in the low temperature regime. Nevertheless, T_1 was extrapolated by fitting the SR curves to a stretched exponential (Eq. 5.1). The results are shown in Fig. 5.5.

The relaxation behavior above 6 K for all fields follows closely the behavior of previous ^{13}C NMR measurements [51], but diverges quickly below that temperature. Unlike in previous ^{13}C measurements, the anomalous peak is much sharper and more reminiscent of a second-order phase transition. This behavior is observed across three different samples and in three different experimental setups. The peak is field-dependent increasing in temperature with increasing field. Note however, that although it may appear that the 12 T relaxation does not have a peak, this is the result of having no measurements in the temperature range where the peak would be expected. The presence of a peak at high fields casts doubt on the impurity spin interpretation, at least in the case of κ-CuCN, and reopens questions about the nature of the 6 K anomaly.

Another significant difference from previous ^{13}C measurements is that $1/T_1$ drops rapidly

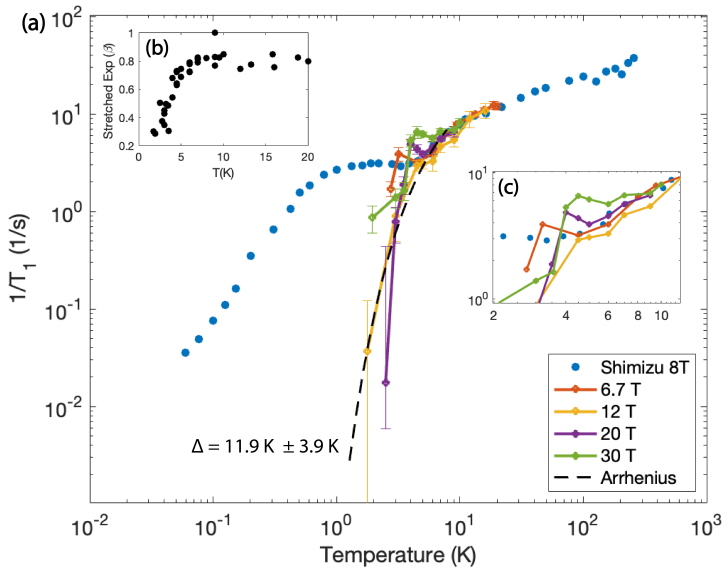

Figure 5.5: (a) $1/T_1$ vs. T from stretched exponential fits to saturation-recovery curves plotted alongside results from Shimizu *et al.* [51]. For temperatures above $\sim$ 4.5 K, T_1 is unbiased, otherwise T_1 is measured from center of spectra due to excess linewidth. (b) Variation of the stretching exponent, β, across temperature. (c) A closer look around the peaks in $1/T_1$ that appear right before a significant fall off.

below the sharp peak, and there is no contribution from a broad peak masking Arrhenius behavior. Although the gap appears to be field-dependent, the lack of data points and size of the error bars prevents us from making any solid conclusions. It is best to fit an Arrhenius curve over the entire set of data points, ignoring the peaks, to obtain an estimate of the average gap size. Such a fit returns an energy gap of $\Delta = 11.9$ K $\pm$ 3.9 K.

Consistent with the spectral measurements, the behavior of the 30 T relaxation at low-temperatures is different from the other three fields. Although the peak at higher temperatures is still present, $1/T_1$ does not fall off as dramatically as in 12 T and 20 T, possibly indicating the closing of a gap.

5.3 Analysis of T_1 Distributions

Discerning the behavior of the gap is crucial for correct interpretation of the ground state of κ-CuCN. While uncertainties in the form of the recovery prevent us from making conclusive statements regarding the field-dependence of the gap, a stretched exponential is usually interpreted as a signature of an inhomogeneous *distribution* of relaxation rates. Thus, examining the evolution of the $1/T_1$ distribution may to provide some insight into the general behavior of the gap (its distribution and strength) in relation to the magnetic field.

There are a couple of methods available to extract the distribution of relaxation times from a recovery "fit" to the so-called stretched recovery form. The first is through the parameters of the stretched exponential fit itself. The standard procedure when encountering a stretched exponential in NMR is to fit it to the equation

$$M(t) = M_o\left[1 - Be^{-(t/T_1^*)^\beta}\right] \tag{5.1}$$

where $M(t)$ is the magnetization of the nuclear spins along $\hat{z}$ as a function of time t after a pulse, M_o the fully recovered value of the magnetization, B a constant to account for incomplete saturation, T_1^* the recovery rate of the spins, and β the stretched exponential constant. The parameters $1/T_1^*$ and β returned from the fit are associated with a probability distribution of relaxation times which has been analyzed by D.C. Johnston [87]. The problem with this interpretation is that it assumes the recovery and associated distribution fits a purely mathematical equation, while the distribution of a real system can be much more complex.

Recently, others have been utilizing the Inverse Laplace Transform (ILT) method to decompose stretched exponential curves in order to extract information that cannot be learned from a stretched exponential fit alone [88–91]. The ILT computes the probability density of $1/T_1$ *without* any bias other than the assumption that the recovery curve is the discrete sum of single relaxation curves, each with their own weighting factor. This approach allows for the possibility of recovering distributions with physical significance, like the bimodal peaks seen in ref. [89]. However, the ILT fit comes with its own issues, described in detail in

Appendix A. In summary, it is extremely sensitive to noise and prone to producing artifacts when fed an incomplete recovery curve.

In this section, I compare and contrast the distributions implied from both the stretched exponential fit and the ILT fit in an attempt to find out what both appear to agree on and where they differ in interpretation.

5.3.1 Comparison of ILT and Johnston Distributions

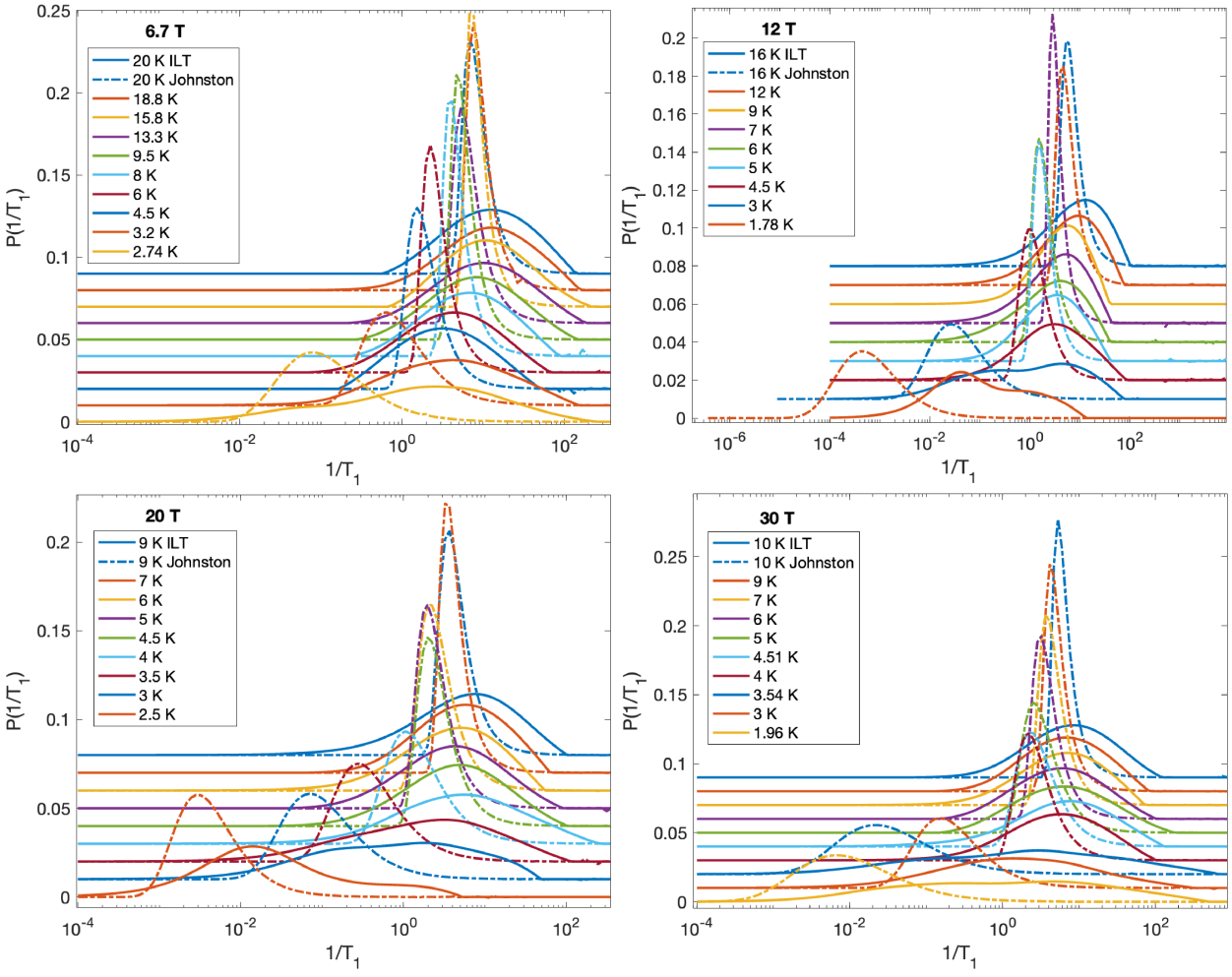

Figure 5.6: Distribution of $1/T_1$ in the ^{13}C NMR relaxation determined via ILT (solid lines) and the Johnston model (dashed lines) plotted across 6.7 T, 12 T, 20 T, and 30 T. $P(1/T_1)$ has been normalized so that $\sum P(1/T_1) = 1$.

The distributions of $1/T_1$ across temperature for κ-CuCN as determined by the ILT fit and Johnston model are plotted overlayed on top of each other in Fig. 5.6. There are three obvious differences seen here. The first is that the Johnston distributions are much sharper than the ILT distributions, especially at higher temperatures. This can be explained by the fact that the ILT distribution depends on both the "stretchedness", or perceived β, of the recovery as well as the α chosen for the calculation, whereas the broadness of the Johnston distribution depends solely on β. For the entire ILT calculation, α was fixed at 3 (for reasons explained in the Appendix), which is a larger value than the optimal alpha at higher temperatures. Had the optimal alpha been used, the ILT distributions at higher temperatures would be much narrower. The second point of contrast is the apparent location of the median. The median of the ILT distribution very consistently sits nearby $1/T_1^*$, while the median for the Johnston distribution seems to move toward smaller $1/T_1$ with decreasing β. The latter is not actually true, as there is quite a bit of invisible weight in the tail for the case of small β [87]. In fact, the median of the Johnston distribution *also* sits nearby $1/T_1^*$ for $\beta \geq 0.4$ and diverges quickly toward ∞ below that. Due to its divergent behavior, the Johnston distribution cannot be used as a measure of anything physical below $\beta \approx 0.4$. The last point of contrast, which will be discussed in more detail below, is the presence of features in the ILT distribution at low temperatures.

5.3.2 Analysis of ILT Distributions

The ILT fit seems to confirm that one part of the original hypothesis is true, namely that the low temperature relaxation of κ-CuCN is dominated by two contributions. A small peak separates from the left side of the main peak below 4.5 K and separates further with lower temperature and higher fields (see Fig. 5.7). The intensity of this second component simultaneously increases as it separates. The faster component, although much higher in magnitude, also decreases with lower temperature and higher field. In agreement with the behavior of the stretched exponentials, the 30 T relaxation is again sporadic, diverging away from the qualitative behavior of the other fields below 3.5 K.

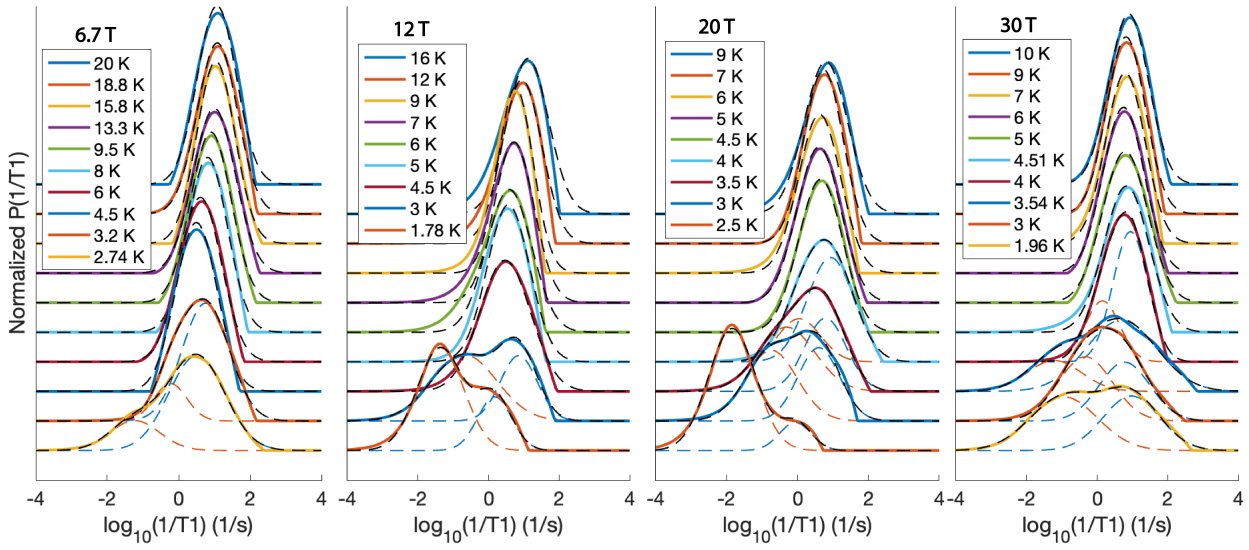

Figure 5.7: Distribution of $1/T_1$ in the ^{13}C NMR relaxation determined via ILT (solid lines) and the Gaussian fit of its compnents (dashed lines) plotted across 6.7 T, 12 T, 20 T, and 30 T. $P(1/T_1)$ has been normalized so that $\sum P(1/T_1)\Delta(1/T_1) = 1$.

The distributions at low-temperature were fitted to two Gaussian peaks, and the results of the fit are plotted in Fig. 5.7. The peak means are also plotted in Fig. 5.8. Due to bad resolution, the ILT fit cannot confirm a field-dependent gap any better than the stretched exponential fit, in this case. However, the 20 T relaxation, plotted in the inset of Fig. 5.8, does seem to imply that both components fall dramatically below the initial $1/T_1$ peak, and that fall off may be Arrhenius in nature.

A further issue is the identification of the two different relaxation mechanisms implied by the ILT fit. Superficially, the behavior of the distribution resembles that of another QSL candidate, herbertsmithsite [89], where ^{63}Cu NQR measurements were performed alongside an ILT fit. Just like in the case of ^{13}C κ-CuCN, a small peak associated with slower relaxation separates itself from a larger peak and grows in intensity as temperature decreases. The larger peak, which differs from κ-CuCN, sits at a roughly constant relaxation time. The behavior was explained using a model where spin singlets, whose relaxation times are dramatically suppressed, form alongside paramagnetic impurities, whose relaxation times are enhanced and constant. This model does not work for the case of κ-CuCN for a couple of reasons.

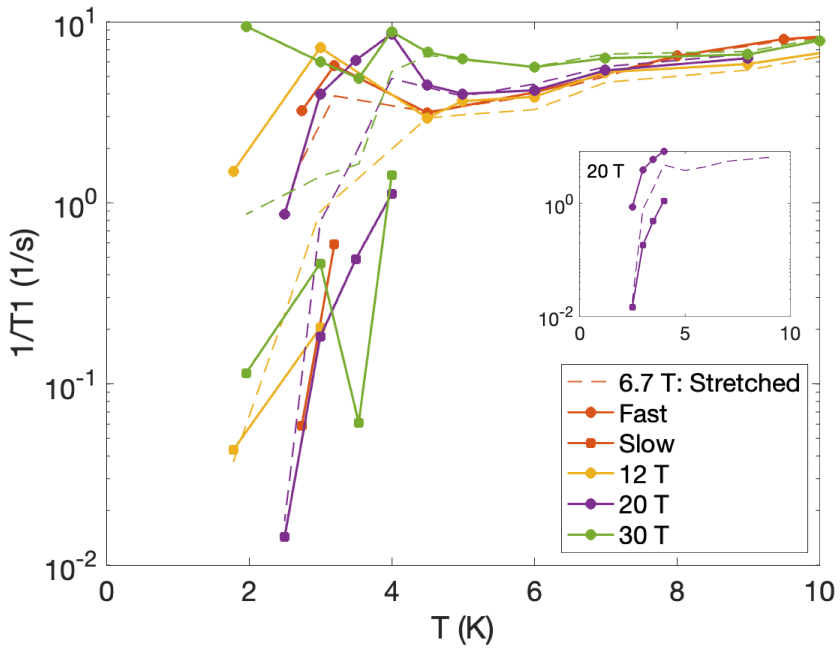

Figure 5.8: $1/T_1$ as determined by an ILT fit to saturation-recovery curves. Solid circles represent the faster relaxing component while squares represent the slower one. For comparison, the stretched exponential fits are plotted as dashed lines. An Arrhenius fit over all fields estimates a gap size of 16.7 K. Inset: 20 T relaxation is plotted to highlight the general behavior, per field, of the two components.

First, the faster relaxing component in κ-CuCN is not constant, and therefore cannot be explained by paramagnetic spins. Second, the intensity of the slower component appears to increase with field when temperature is held constant, a feature that is unexpected for singlet physics. One can also consider the model used to explain the relaxation behavior of κ-HgCl in Chapter 3 and find that it does not fit here, either. The response of ^{13}C nuclear spins coupled to paramagnetic impurities should be plateaued at 30 T. This is corroborated by the fact that the NMR linewidth below 3.5 K at 30 T is saturated, implying that the paramagnetic spins have reached full alignment and are therefore frozen out. The presence of the faster component in the ILT at 30 T confirms that it is not the response of paramagnetic impurities.

We should approach the interpretation of features in the ILT distribution carefully as

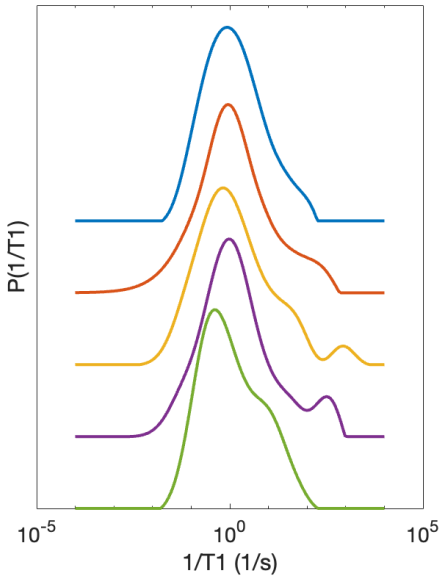

Figure 5.9: ILT fits of simulated pure stretched recoveries, which normally do not have any bumps or kinks. The parameters of the recovery curves are $\beta = 0.5$, $1/T_1 = 1$, $S/N = 35$, and $\alpha = 3$ was used in the ILT fit.

the recovery curves obtained in this experiment are not ideal candidates for ILT analysis. Low signal to noise ratio as well as incomplete recovery at low temperatures are expected to produce artifacts. As a result, it is imperative to consider the possibility that the peaks observed in the ILT are the result of noise in the stretched recovery curve. Stretched recoveries, where $\beta \leq 0.5$, naturally have long, prominent tails on the right side of the distribution. Coupled with a sufficient amount of noise, the distribution could contain artifact kinks that look like meaningful peaks. Fig. 5.9 illustrates the point. The distributions in the figure are ILT fits of simulated stretched recoveries with $\beta = 0.5$, $1/T_1 = 1$, $S/N = 35$, and $\alpha = 3$, values close to that of the 20 T 2.5 K data point. Within the 5 generated curves, there are 2-3 which have the same shape as the curve obtained from the experimental data. A more robust examination, which computes the difference between the cumulative distribution function of a generated stretched exponential ILT and the experimentally observed ILT, predicts that the experimental data is in the 70th percentile of the normal distribution of curves produced by noise. However, this test does not account for the possibility that the

intrinsic distribution may be quantitatively similar to a stretched exponential distribution, and a different approach may be required to determine the significance of the bimodal peaks.

If we resign ourselves to the notion that we cannot prove the authenticity of the kinks and therefore must ignore them, the picture is simplified. Now, we have a smooth distribution of $1/T_1$ which is collectively depressed as the temperature decreases and a field dependence that cannot be resolved. The endpoints of the ILT indicate that the distribution of relaxation times decreases sharply at temperatures below the second-order phase transition temperature. This allows us to classify κ-CuCN as a fully gapped material, even though the gap is inhomogeneous.

5.4 Discussion/Conclusion

The results from the ^{13}C NMR experiments on κ-CuCN in high magnetic fields highlighted in this chapter have answered some important questions regarding the ground state of κ-CuCN. First, both the relaxation from the stretched exponential and ILT fit agree that κ-CuCN is *fully* gapped. Although $1/T_1$ is inhomogeneous, the entire distribution decreases rapidly below a certain temperature, and that falloff can be fit to an Arrhenius curve. The findings do not support the U(1) QSL model with a spinon fermi surface. Second, $1/T_1$ measurements confirm that ^{13}C NMR is, indeed, sensitive to the second-order phase transition. Instead of a broad peak after the initial drop in $1/T_1$, as seen in previous ^{13}C NMR measurements [51], a short, sharp peak is observed. This peak is not the response of paramagnetic impurities, as originally thought, but is similar to the one observed in ^{63}Cu NQR experiments by Kobayashi *et al.* [92], which has also been linked to a second-order phase transition.

Given that a spin-gap appears very close to the location of the second-order phase transition, it is likely that the broken symmetry involves the spin degrees of freedom, and it is hard to make the case for a QSL ground state in κ-CuCN. Instead, future interpretations need to consider models that include a gapped, nonmagnetic state that is associated with a broken symmetry as well as a lattice distortion. This makes the recent VBS hypothesis a

strong contender. However, we cannot fully confirm or deny the validity of the hypothesis, due to a perceived field-dependence of the gap which is inconsistent with VBS behavior. The field dependence, which is speculative because of large uncertainty, suggests that the gap grows stronger with field, but is partially suppressed at 30 T.

Some effort to clarify the field dependence of the gap is necessary before the VBS ground state can be seriously considered. However, NMR spectroscopy, in its current state, may not be equipped for the task. Very long relaxation coupled with increasingly stretched recoveries in κ-CuCN makes it difficult to obtain $1/T_1$ to high certainty. It was determined that the Johnston approach fails in the case of very stretched exponentials, and ILT measurements require an prohibitively large amount of data acquisition time to reduce noise and obtain a fully recovered relaxation curve. It may be worthwhile to perform frequency dependent measurements of χ_s via EPR, since the issue of inhomogeneity is not as prevalent in such a probe.

APPENDIX A

Examination of ILT Method

A.1 Method

The implementation of the ILT follows closely what was outlined in the supplementary of Singer *et al.* [88], except modified for saturation recovery instead of inversion recovery. The interested reader should refer to Singer *et al.* for a more in depth explanation of the method. The user assumes that the saturation recovery curve is the discrete sum of single exponential recoveries:

$$M(t) = \sum_i P(1/T_{1,i})\left[1 - e^{-t(1/T_{1,i})}\right] \tag{A.1}$$

where $P(1/T_{1,i})$ is the weight of the single exponential component with inverse relaxation time $(1/T_{1,i})$. Tikhonov Regression (or Ridge Regression) [93] is implemented in order to solve for the distribution of $P(1/T_{1,i})$, since the problem is inherently ill-posed. A typical recovery curve will have somewhere on the order of 25-50 data points while the number of parameters $(1/T_{1,i})$ in the equation being fitted can be in the hundreds.

The equation, $\boldsymbol{M_{ILT}}$, which the experimental data, $\boldsymbol{M_{exp}}$, will be fit to is expressed as a vector:

$$\boldsymbol{M_{ILT}} = K\boldsymbol{P} + \boldsymbol{E} \tag{A.2}$$

where $K_{ij} = [1 + e^{-t_i(1/T_{1,j})}]$, $P_j = (1/T_{1,j})$, and $\boldsymbol{E}$ is a vector representing Gaussian noise. The problem, then, is to the find a non-negative $\boldsymbol{P}$ which minimizes the cost function

$$||\boldsymbol{M_{exp}} - K\boldsymbol{P}||^2 + \alpha||\boldsymbol{P}||^2 \tag{A.3}$$

The first term of the equation is the non-negative least squares cost function, but an additional second term increases cost when utilizing too much of the $\boldsymbol{P}$ vector, in other

words, overfitting. Via the methodology described in refs. [93, 94], the optimal solution for $\boldsymbol{P}$ is found by minimizing the function $f(\boldsymbol{c})$, defined in Eq. A.4, with respect to $\boldsymbol{c}$ using a quasi-Newton algorithm. This was done with MATLAB using the *fminunc* function with the quasi-Newton algorithm specified.

$$f(\boldsymbol{c}) = \frac{1}{2}\boldsymbol{c'}\big[G(\boldsymbol{c}) + \alpha I\big]\boldsymbol{c} - \boldsymbol{c'M_{exp}} \tag{A.4}$$

In this equation,

$$G(\boldsymbol{c}) = \begin{bmatrix} H(K_1'\boldsymbol{c}) & 0 & \dots & 0 \\ 0 & H(K_2'\boldsymbol{c}) & \dots & 0 \\ \vdots & \vdots & & \vdots \\ 0 & 0 & \dots & H(K_m'\boldsymbol{c}) \end{bmatrix}$$

H is the Heavyside function, K_j' is the transposed jth column of K, and I is the identity matrix. Once $\boldsymbol{c}(\alpha)$ is found, $\boldsymbol{P}$ is chosen so that $\boldsymbol{P} = \max\{0, K'\boldsymbol{c}\}$. Note that $\boldsymbol{c}$ is a function of α, which has yet to be determined.

According to Singer *et al.*, the optimal value for α, α_{opt}, is found in one of two ways. When experimental noise is dominant, under the Bulter-Reeds-Dawson (BRD) condition [93], α_1 is found when $\chi(\alpha) = \alpha||\boldsymbol{c}|| = \sigma_E\sqrt{n}$, where σ_E is the experimental noise and n is the number of data points. If systematic error is significant, α_1 from the BRD condition must be compared with the "heel" condition, $\mathrm{dln}\chi(\alpha)/\mathrm{dln}\alpha|_{\alpha_2} = 10^{-1}$, and $\max(\alpha_1, \alpha_2)$ is chosen. α_1 was solved numerically by minimizing $f(\boldsymbol{c}(\alpha_o))$ for 10 different values of α_o, logarithmically spaced from 10^{-3} to 10^2, and choosing the α where $\mathrm{abs}(\sigma_E\sqrt{n} - \alpha_o||\boldsymbol{c}||)$ was minimal. α_2 was solved by choosing the α where $\mathrm{abs}(\frac{\mathrm{d}\chi(\alpha_o)}{\mathrm{d}\alpha_o}\alpha_o - 10^{-1})$ was minimal. For reasons that will be explained in the next section, α_{opt} was not used. Instead, a fixed α was chosen for the entire data set based off the set of optimal α values.

Once $P(1/T_1)$ is found, it is initially returned such that $\sum_i P(1/T_{1,i}) = M_o$. However, for the purpose of performing Gaussian fits, it was normalized so that $\sum_i P(1/T_{1,i})\Delta P = 1$, where $\Delta P = \log_{10}(1/T_{1,i+1}) - \log_{10}(1/T_{1,i})$.

A.2 Choosing Alpha

Alpha (α) functions a smoothing factor. Larger alphas will produce a fit that ignores kinks and bumps in the experimental data while smaller alphas will try to fit to the data more precisely, capturing noise and all. Increasing alpha effectively reduces the resolution of the ILT fit, producing broader distributions, as shown in Fig. A.1.

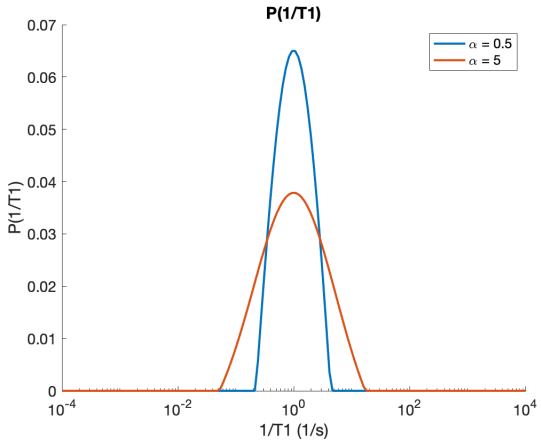

Figure A.1: ILT fits for a simulated recovery curve with $T_1 = 1$, Signal to Noise = 100, $\alpha = 0.5$ (blue) and $\alpha = 5$ (orange).

Signal to noise (S/N) was estimated from the time transients recorded, and checked for consistency against the recovery curves. S/N from the recovery curves were estimated by fitting a pure, stretched exponential curve over the experimental data and choosing the root mean square error (rmse) of the fit as the noise level, σ_E. Caution should be warranted here, as the fit will produce larger values of σ_E if the recovery is not a purely stretched exponential, but the sum of (for example) two main relaxation contributions.

The optimal α value per recovery curve is then calculated as described in A.1. However, α_{opt} would vary significantly across temperature, creating abrupt changes in the broadness of the ILT peaks that did not reflect true changes in the system, but rather reflected the level of noise for the measurement. An example, taken from κ-CuCN ILT fits, is shown in Fig. A.2. It was decided that it would be more appropriate to choose a *fixed* value for α close to the average of all the α_{opt} values across the data set, keeping in mind the risk of

losing information when $\alpha > \alpha_{\text{opt}}$ and picking up noise in the opposite case.

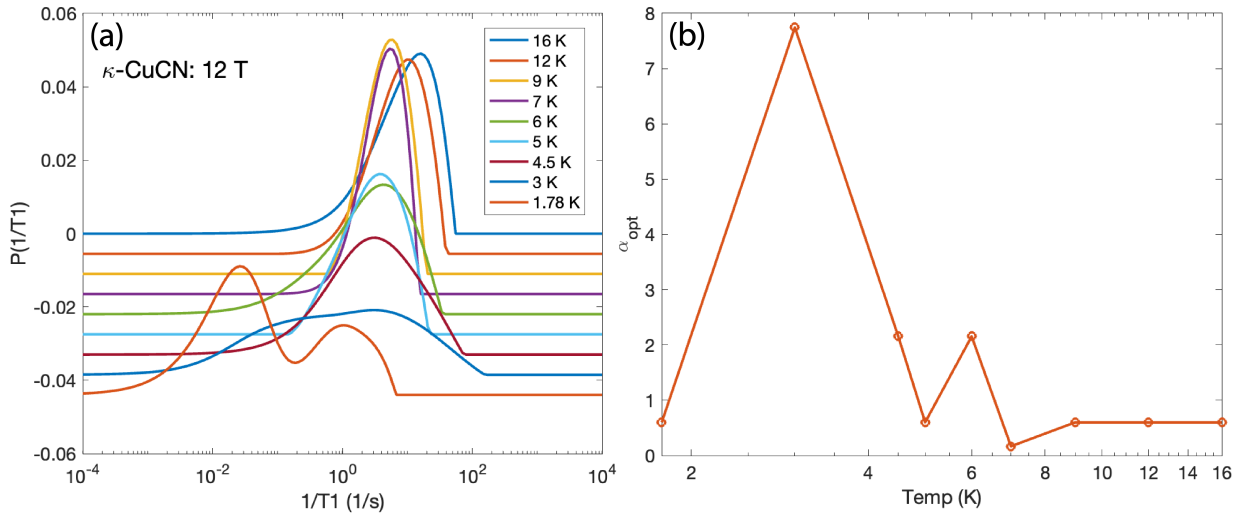

Figure A.2: (a) ILT fit of κ-CuCN 12 T relaxation using optimal α values (b) Optimal alpha values for 12 T.

A.3 Effectiveness at Finding Distributions

The effectiveness of the ILT at finding the true distribution of a recovery curve was tested by performing the ILT fit on simulated stretched exponentials and "dummy" recoveries where the distribution of $1/T_1$ is known. It was determined that the ILT is quite accurate at finding the distributions when the curve is fully recovered and the level of noise is low. If those two conditions are not met, artifacts are inevitable.

A.3.1 Complete Recovery

The ILT of several stretched exponentials with varying $1/T_1^*$ and β values is plotted in Fig. A.3. The plot shows that the ILT accurately estimates the $1/T_1^*$ value of the stretched exponential, as demonstrated by the center of gravity of the distribution. Furthermore, the shape of the distribution agrees with those calculated by Johnston [87] where a tail appears on the right side of the curve and becomes longer and more pronounced as the exponential

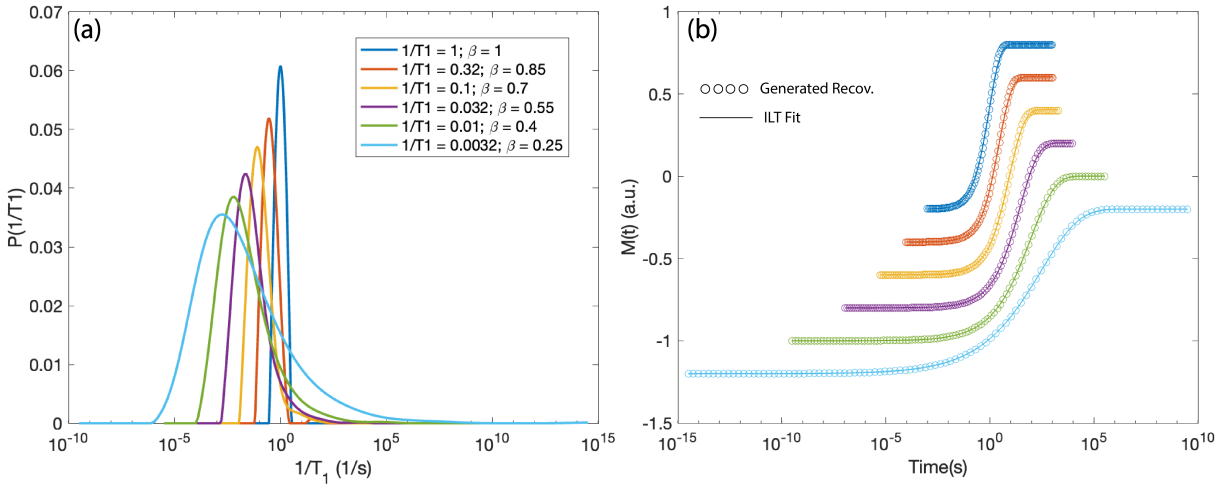

Figure A.3: (a) ILT fit to several stretched exponential recoveries with varying $1/T_1$ and β values. (b) The simulated stretched exponential (open circles) plotted alongside the calculated recovery curve from the ILT fit (solid line).

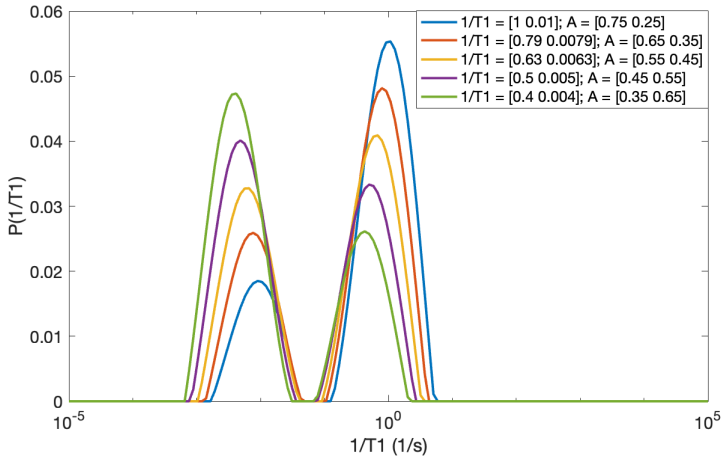

Figure A.4: ILT fit to several two-component recoveries with varying $1/T_1$ and amplitudes.

becomes increasingly stretched. However, the peak of the ILT distribution remains close to $1/T_1^*$, while Johnston's peaks shift to lower values of $1/T_1$ because the distribution's tails extend to $1/T_1 = \infty$. While such behavior is correct for a pure stretched exponential, it is not realistic, and the ILT method better adjusts for cutoffs in $1/T_1$ range. The ILT was also tested for several two-component recoveries with varying $1/T_1$ and amplitudes and it was able to capture the correct distributions fairly well. The results of that simulation are shown

in Fig. A.4.

A.3.2 Incomplete Recovery and Late Acquisitions

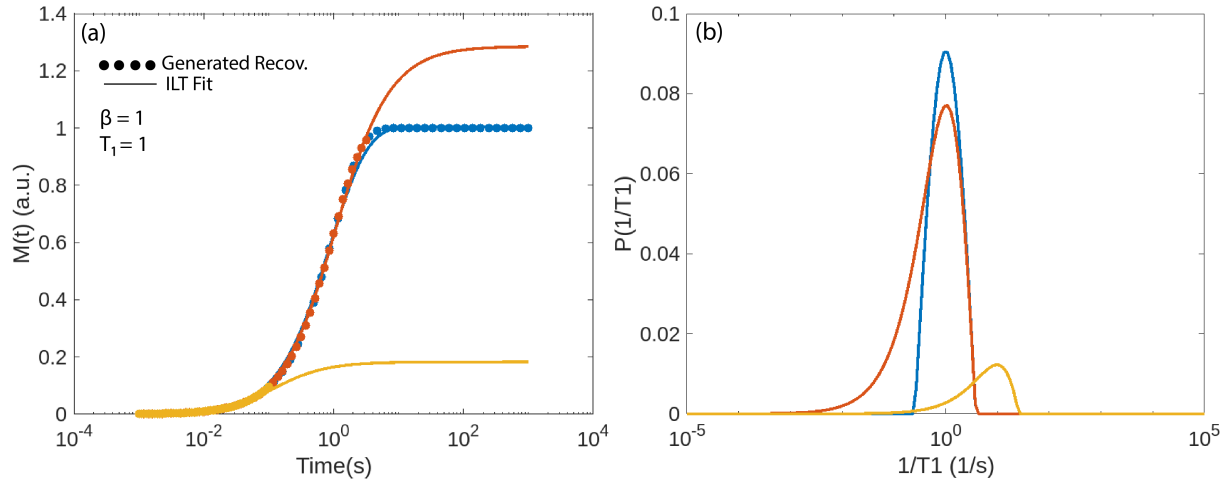

Figure A.5: (a) Generated stretched exponential curves with $\beta = 1$ and $1/T_1 = 1$. Blue is a complete recovery, orange is slightly incomplete at the top, and yellow is extremely incomplete. (b) ILT fit results on generated stretched exponentials. The fit for the incomplete recovery shows a tail which is not present when the ILT is given the full curve, and a greatly overestimated $1/T_1$ in the extreme case.

Tails can also appear in the ILT as a result of incomplete recovery, in other words, not a sufficient amount of flatness at the top of the recovery. Fig. A.5 shows the effects of performing an ILT fit on a recovery that is not fully recovered. For this simulation, $\beta = 1$, $1/T_1 = 1$, and the range of $1/T_1$ is fixed as 150 bins from 10^{-5} to 10^{5}. The true curve (in blue) does not have any tails on either side of the $P(1/T_1)$ distribution. However, when performing an ILT on a curve that is not fully recovered (orange), the ILT fit becomes unsure of where the recovery actually ends. As a result, it produces a tail on the left side of the $P(1/T_1)$ distribution, and the fitted recovery curve overshoots the true value of M_o. Despite this flaw, $1/T_1$ is still estimated correctly, at least for the values of β and $1/T_1$ chosen. However, for more extreme cases of incomplete saturation, $1/T_1$ is overestimated, and the tail becomes extreme.

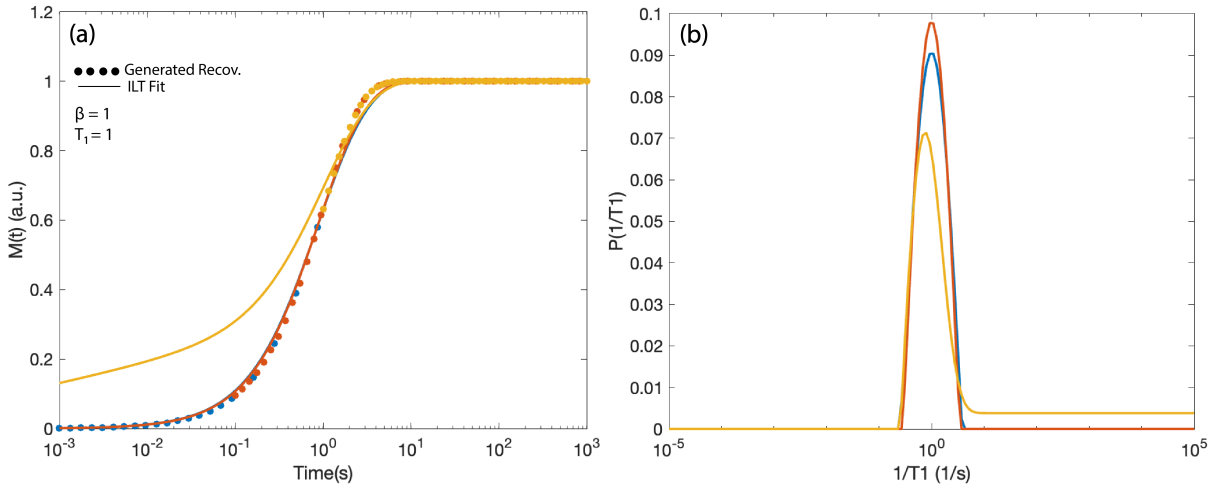

Figure A.6: (a) Generated stretched exponential curves with $\beta = 1$ and $1/T_1 = 1$. Blue is a complete recovery, orange is incomplete at the bottom, and yellow is extremely incomplete (b) ILT fit results on generated stretched exponentials. The fit for the incomplete recovery shows a constant artifact on the right only in the extreme case.

If the curve is incomplete at the early end of the recovery, the effect is not as catastrophic. The ILT can accurately predict where the true curve should begin, up to a certain limit. Fig. A.6 shows a complete recovery curve (blue) and a curve where the acquisition begins late (orange). For the orange curve, the fit correctly fills in the early end of the recovery, producing only a slight difference in amplitude in the $P(1/T_1)$ distribution. However, the ILT fails in the case of the yellow curve where less than half the recovery is captured. The low end is not fitted to correctly, and a constant artifact is produced on the right side of $P(1/T_1)$.

A.3.3 Incomplete Saturation

The issue of incomplete saturation was covered in Singer *et al.* [88], so it will not be discussed in detail here. If a recovery curve starts at a nonzero value due to incomplete saturation, the ILT will produce a constant peak in $P(1/T_1)$, similar to the one seen for late acquisitions, at approximately the same timescale as the time of the first acquired point in the recovery. Rather than setting a "cutoff" frequency, as was suggested by Singer *et al.*, it was found

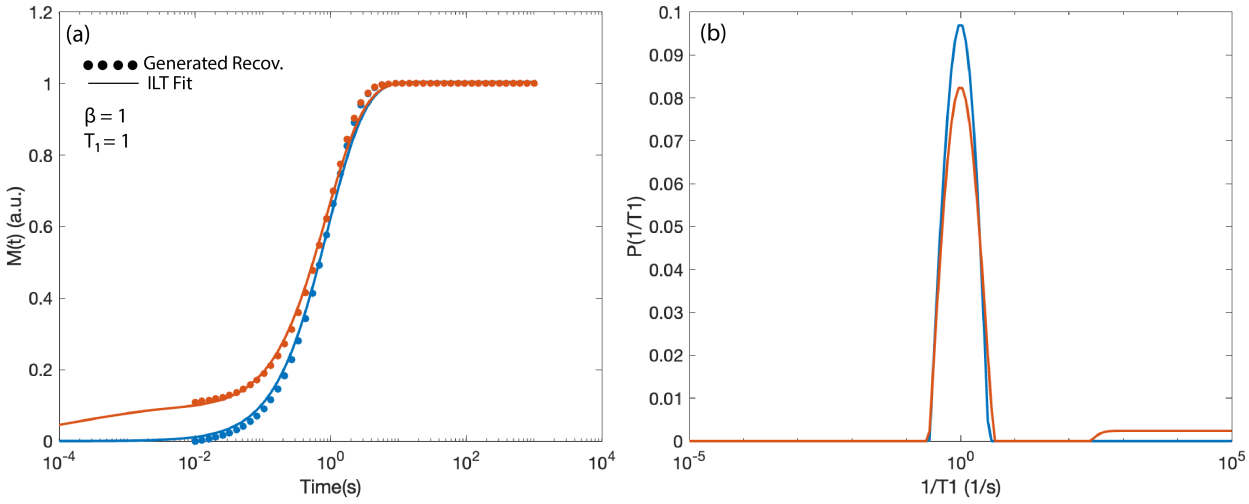

Figure A.7: (a) A recovery curve with incomplete saturation (orange) and the same curve shifted and normalized so that the first point starts at 0 and the last point ends at 1 (blue). (b) ILT fit for the two recoveries in plotted (a).

that shifting the recovery and renormalizing was sufficient enough to remove the artifact, as shown in Fig. A.7. Care should be taken to distinguish an incomplete saturation from a late acquisition, as the latter case can be left alone if not too extreme, and shifting the recovery curve may lead to incorrect interpretation of $1/T_1$ by the ILT. One can identify an incomplete saturation by a nonzero, flat line at the beginning of the recovery, but it may be more difficult to detect in the case of very stretched exponentials.

A.3.4 The Effect of Noise

The effect of noise on the ILT distribution needs to be considered. In general, noise will produce artificial bumps in the distribution that could be misinterpreted as physically significant peaks, as shown in Fig. A.8. The purpose of the smoothening factor, α, is to mitigate such effects, but there is a limit to how much it can do. Even at very high levels of S/N, α_{opt} does not fully eliminate artificial bumps, although it does a sufficient job at smoothening them. At S/N < 50, the effects of noise are significant. The effect of noise on the ILT distribution, and the inability of α_{opt} to fully remove noisy artifacts, highlights a need for experimentalists

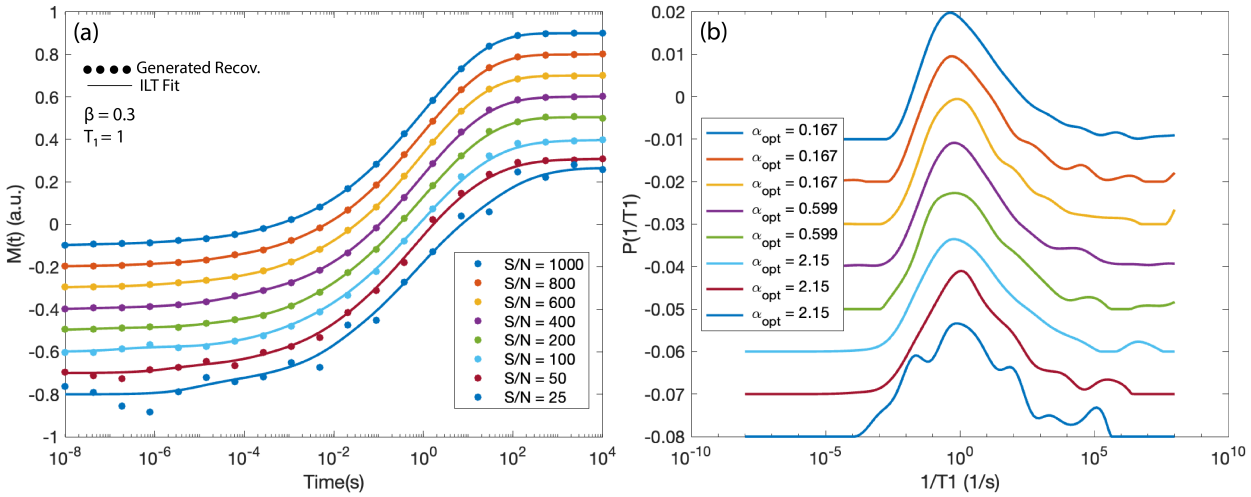

Figure A.8: (a) Generated stretched exponentials with $\beta = 0.3$ and $T_1 = 1$ with varying levels of signal to noise. (b) ILT fit to the stretched exponentials in (a) using the calculated α_{opt} as the smoothing factor.

using ILT to approach interpretation of small peaks carefully, making sure to take steps to distinguish real signal from noise.

A.3.5 Conclusion

The ILT is preferred over the Johnston model for purposes of obtaining $1/T_1$ distributions of real systems, especially in the case of stretched exponential recoveries. When fit to a purely mathematical stretched exponential, it returns the correct shape, as demonstrated by Fig. A.3. It can also estimate $1/T_1^*$ of the stretched exponential, since $1/T_1^*$ is equivalent to the center of gravity of the ILT distribution [88]. Since it is not restricted to an analytical form, it is also able to produce unique distributions, like bimodal peaks, which the Johnston model cannot.

However, as is the nature of any ill-posed problem, the ILT fits to the data *too* well. This makes it extremely sensitive to noise and prone to producing artificial bumps and peaks, even with smoothing factored in. In order to minimize artifacts, data taken for ILT purposes take much more time to acquire compared to the average T_1 measurement, as one needs

to obtain a full recovery as well as average over many acquisitions to achieve satisfactory results.

With these considerations in mind, the ILT is more suited for faster relaxation experiments where such recovery curves can be obtained within a reasonable amount of time. For cases of long relaxation, where some estimation of T_1 is needed despite having an incomplete recovery, it may not be worth the time and trouble, as the stretched exponential fit is actually *better* at predicting a recovery curve (assuming the curve fits a pure stretched exponential), and therefore better at estimating T_1. However, the distribution returned by a pure stretched exponential is unrealistic, and the ILT might still be a better way of extrapolating any fast relaxing features that might be present in the partial recovery, thus giving it some use in the case of long recoveries.

BIBLIOGRAPHY

[1] A. Pustogow, T. Le, H.-H. Wang, Y. Luo, E. Gati, H. Schubert, M. Lang, and S. E. Brown, "Impurity moments conceal low-energy relaxation of quantum spin liquids", Physical Review B **101**, 140401 (2020).

[2] T. Le, A. Pustogow, J. Wang, A. Henderson, T. Siegrist, J. A. Schlueter, and S. E. Brown, "Disorder and slowing magnetic dynamics in $\kappa-(\mathrm{BEDT-TTF})_2\mathrm{Hg(SCN)}_2\mathrm{Br}$", Physical Review B **102**, 184417 (2020).

[3] E. Ising, "Beitrag zur Theorie des Ferromagnetismus", Z. Physik **31**, 253–258 (1925).

[4] H. Bethe, "Zur Theorie der Metalle", Zeitschrift für Physik **71**, 205–226 (1931).

[5] G. H. Wannier, "The Triangular Ising Net", Physical Review **79**, 357–364 (1950).

[6] P. W. Anderson, "Resonating Valence Bonds: A New Kind of Insulator?", Materials Research Bulletin **8**, 153–160 (1973).

[7] P. W. Anderson, "The resonating valence bond state in La_2CuO_4 and superconductivity", Science **235**, 1196–1198 (1987).

[8] L. Capriotti, A. E. Trumper, and S. Sorella, "Long-range néel order in the triangular heisenberg model", Physical Review Letters **82**, 3899–3902 (1999).

[9] S. R. White and A. L. Chernyshev, "Neél order in square and triangular lattice heisenberg models", Physical Review Letters **99**, 2–5 (2007).

[10] B. Bernu, C. Lhuillier, and L. Pierre, "Signature of Néel order in exact spectra of quantum antiferromagnets on finite lattices", Physical Review Letters **69**, 2590–2593 (1992).

[11] Y. Shimizu, K. Miyagawa, K. Kanoda, M. Maesato, and G. Saito, "Spin Liquid State in an Organic Mott Insulator with a Triangular Lattice", Physical Review Letters **91**, 1–4 (2003).

[12] J. Wen, S.-L. Yu, S. Li, W. Yu, and J.-X. Li, "Experimental identification of quantum spin liquids", npj Quantum Materials **4**, 1–9 (2019).

[13] L. Savary and L. Balents, "Quantum spin liquids: A review", Reports on Progress in Physics **80**, 16502 (2017).

[14] L. Balents, "Spin liquids in frustrated magnets", Nature **464**, 199–208 (2010).

[15] C. Broholm, R. J. Cava, S. A. Kivelson, D. G. Nocera, M. R. Norman, and T. Senthil, "Quantum spin liquids", Science **367**, `10.1126/science.aay0668` (2020).

[16] Y. Zhou, K. Kanoda, and T. K. Ng, "Quantum spin liquid states", Reviews of Modern Physics **89**, 1–50 (2017).

[17] S. Florens and A. Georges, "Slave-rotor mean-field theories of strongly correlated systems and the Mott transition in finite dimensions", Physical Review B - Condensed Matter and Materials Physics **70**, 1–15 (2004).

[18] A.Yu. Kitaev, "Fault-tolerant quantum computation by anyons", Annals of Physics **303**, 2–30 (2002).

[19] A. Y. Kitaev, "Anyons in an exactly solved model and beyond", Annals of Physics **321**, 2–111 (2006).

[20] S. Yunoki and S. Sorella, "Two spin liquid phases in the spatially anisotropic triangular Heisenberg model", Physical Review B - Condensed Matter and Materials Physics **74**, 1–31 (2006).

[21] M. Q. Weng, D. N. Sheng, Z. Y. Weng, and R. J. Bursill, "Spin-liquid phase in an anisotropic triangular-lattice Heisenberg model: Exact diagonalization and density-matrix renormalization group calculations", Physical Review B - Condensed Matter and Materials Physics **74**, 2–5 (2006).

[22] R. Kaneko, S. Morita, and M. Imada, "Gapless spin-liquid phase in an extended spin-1/2 triangular Heisenberg model", Journal of the Physical Society of Japan **83**, 10–13 (2014).

[23] R. V. Mishmash, J. R. Garrison, S. Bieri, and C. Xu, "Theory of a competitive spin liquid state for weak mott insulators on the triangular lattice", Physical Review Letters **111**, 1–5 (2013).

[24] Z. Zhu and S. R. White, "Spin liquid phase of the S= 1/2 J_1-J_2 heisenberg model on the triangular lattice", Physical Review B - Condensed Matter and Materials Physics **92**, 4–7 (2015).

[25] W. J. Hu, S. S. Gong, W. Zhu, and D. N. Sheng, "Competing spin-liquid states in the spin-1/2 Heisenberg model on the triangular lattice", Physical Review B - Condensed Matter and Materials Physics **92**, 1–6 (2015).

[26] H. Morita, S. Watanabe, and M. Imada, "Nonmagnetic insulating states near the mott transitions on lattices with geometrical frustration and implications for κ-$(ET)_2Cu_2(CN)_3$", Journal of the Physical Society of Japan **71**, 2109–2112 (2002).

[27] S. S. Lee and P. A. Lee, "U(1) gauge theory of the hubbard model: spin liquid states and possible application to κ-(BEDT-TTF)$_2$Cu$_2$(CN)$_3$", Physical Review Letters **95**, 1–4 (2005).

[28] O. I. Motrunich, "Variational study of triangular lattice spin-1/2 model with ring exchanges and spin liquid state in κ-$(ET)_2Cu_2(CN)_3$", Physical Review B - Condensed Matter and Materials Physics **72**, 1–7 (2005).

[29] D. S. Rokhsar and S. A. Kivelson, "Superconductivity and the quantum hard-core dimer gas", Physical Review Letters **61**, 2376–2379 (1988).

[30] R. Moessner and S. L. Sondhi, "Resonating valence bond phase in the triangular lattice quantum dimer model", Physical Review Letters **86**, 1881–1884 (2001).

[31] H. O. Jeschke, M. De Souza, R. Valentí, R. S. Manna, M. Lang, and J. A. Schlueter, "Temperature dependence of structural and electronic properties of the spin-liquid candidate κ-(BEDT-TTF)$_2$Cu$_2$(CN)$_3$", Physical Review B - Condensed Matter and Materials Physics **85**, 1–7 (2012).

[32] M. De Souza and L. Bartosch, "Probing the mott physics in κ-(BEDT-TTF)$_2X$ salts via thermal expansion", Journal of Physics Condensed Matter **27**, 53203 (2015).

[33] P. Foury-Leylekian, V. Ilakovac-Casses, V. Balédent, P. Fertey, A. Arakcheeva, O. Milat, D. Petermann, G. Guillier, K. Miyagawa, K. Kanoda, P. Alemany, E. Canadell, S. Tomic, and J. P. Pouget, "κ-(BEDT-TTF)$_2$Cu$_2$(CN)$_3$ spin liquid: beyond the average structure", Crystals **8**, 1–17 (2018).

[34] S. Yasin, E. Rose, M. Dumm, N. Drichko, M. Dressel, J. A. Schlueter, E. I. Zhilyaeva, S. Torunova, and R. N. Lyubovskaya, "Electronic and magnetic studies of κ-(BEDT-TTF)$_2$Hg(SCN)$_2$Cl", Physica B: Condensed Matter **407**, 1689–1691 (2012).

[35] T. Ivek, R. Beyer, S. Badalov, M. Čulo, S. Tomić, J. A. Schlueter, E. I. Zhilyaeva, R. N. Lyubovskaya, and M. Dressel, "Metal-insulator transition in the dimerized organic conductor κ-(BEDT-TTF)$_2$Hg(SCN)$_2$Br", Physical Review B **96**, 1–8 (2017).

[36] V. Ivanov, "κ-(BEDT-TTF)$_2X$ organics (BEDT-TTF) $\equiv$ bis(ethylenedithio)-tetrathiafulvalene), as seen for hubbardists", Philosophical Magazine B: Physics of Condensed Matter; Statistical Mechanics, Electronic, Optical and Magnetic Properties **76**, 697–713 (1997).

[37] H. Kino and H. Fukuyama, "Phase diagram of two-dimensional organic conductors: (BEDT-TTF)$_2X$", Journal of the Physical Society of Japan **65**, 2158–2169 (1996).

[38] H. C. Kandpal, I. Opahle, Y.-Z. Zhang, H. O. Jeschke, and R. Valentí, "Revision of model parameters for κ-type charge transfer salts: an ab initio study", Physical Review Letters **103**, 067004 (2009).

[39] N. Drichko, R. Beyer, E. Rose, M. Dressel, J. A. Schlueter, S. A. Turunova, E. I. Zhilyaeva, and R. N. Lyubovskaya, "Metallic state and charge-order metal-insulator transition in the quasi-two-dimensional conductor κ-(BEDT-TTF)$_2$Hg(SCN)$_2$Cl", Physical Review B - Condensed Matter and Materials Physics **89**, 1–11 (2014).

[40] E. Scriven and B. J. Powell, "Effective Coulomb interactions within BEDT-TTF dimers", Physical Review B - Condensed Matter and Materials Physics **80**, 1–9 (2009).

[41] D. Guterding, R. Valentí, and H. O. Jeschke, "Influence of molecular conformations on the electronic structure of organic charge transfer salts", Physical Review B - Condensed Matter and Materials Physics **92**, 1–6 (2015).

[42] B. J. Powell and R. H. McKenzie, "Dependence of the superconducting transition temperature of organic molecular crystals on intrinsically nonmagnetic disorder: A signature of either unconventional superconductivity or the atypical formation of magnetic moments", Physical Review B - Condensed Matter and Materials Physics **69**, 1–17 (2004).

[43] R. H. McKenzie, *A minor detail that matters in organic charge transfer salts*, (2016)

[44] K. Riedl, R. Valentí, and S. M. Winter, "Critical spin liquid versus valence-bond glass in a triangular-lattice organic antiferromagnet", Nature Communications **10**, 2561 (2019).

[45] C. Hotta, "Quantum electric dipoles in spin-liquid dimer mott insulator κ-$(ET)_2Cu_2(CN)_3$", Physical Review B - Condensed Matter and Materials Physics **82**, 2–5 (2010).

[46] H. Kawamura and K. Uematsu, "Nature of the randomness-induced quantum spin liquids in two dimensions", Journal of Physics. Condensed Matter: An Institute of Physics Journal **31**, 504003 (2019).

[47] M. Hemmida, H. A. Von Nidda, B. Miksch, L. L. Samoilenko, A. Pustogow, S. Widmann, A. Henderson, T. Siegrist, J. A. Schlueter, A. Loidl, and M. Dressel, "Weak ferromagnetism and glassy state in κ-(BEDT-TTF)$_2$Hg(SCN)$_2$Br", Physical Review B **98**, 1–6 (2018).

[48] M. Yamashita, S. Sugiura, A. Ueda, S. Dekura, T. Terashima, S. Uji, Y. Sunairi, H. Mori, E. I. Zhilyaeva, S. A. Torunova, R. N. Lyubovskaya, N. Drichko, and C. Hotta, "Ferromagnetism out of charge fluctuation of strongly correlated electrons in κ-(BEDT-TTF)$_2$Hg(SCN)$_2$Br", npj Quantum Materials **6**, 10.1038/s41535-021-00387-6 (2021).

[49] S. Yamashita, Y. Nakazawa, M. Oguni, Y. Oshima, H. Nojiri, Y. Shimizu, K. Miyagawa, and K. Kanoda, "Thermodynamic properties of a spin-1/2 spin-liquid state in a κ-type organic salt", Nature Physics **4**, 459–462 (2008).

[50] M. Yamashita, N. Nakata, Y. Kasahara, T. Sasaki, N. Yoneyama, N. Kobayashi, S. Fujimoto, T. Shibauchi, and Y. Matsuda, "Thermal-transport measurements in a quantum spin-liquid state of the frustrated triangular magnet -κ-(BEDT-TTF)$_2$Cu$_2$(CN)$_3$", Nature Physics **5**, 44–47 (2009).

[51] Y. Shimizu, K. Miyagawa, K. Kanoda, M. Maesato, and G. Saito, "Emergence of inhomogeneous moments from spin liquid in the triangular-lattice mott insulator κ-(ET)$_2$Cu$_2$(CN)$_3$", Physical Review B - Condensed Matter and Materials Physics **73**, 2–5 (2006).

[52] M. Yamashita, N. Nakata, Y. Senshu, M. Nagata, H. M. Yamamoto, R. Kato, T. Shibauchi, and Y. Matsuda, "Highly mobile gapless excitations in a two-dimensional candidate quantum spin liquid", Science **328**, 1246–1248 (2010).

[53] T. Itou, A. Oyamada, S. Maegawa, and R. Kato, "Instability of a quantum spin liquid in an organic triangular-lattice antiferromagnet", Nature Physics **6**, 673–676 (2010).

[54] B. Miksch, A. Pustogow, M. J. Rahim, A. A. Bardin, K. Kanoda, J. A. Schlueter, R. Hübner, M. Scheffler, and M. Dressel, "Gapped magnetic ground state in quantum spin liquid candidate κ-(BEDT-TTF)$_2$Cu$_2$(CN)$_3$", Science **372**, 276–279 (2021).

[55] R. S. Manna, M. de Souza, A. Brühl, J. A. Schlueter, and M. Lang, "Lattice effects and entropy release at the low-temperature phase transition in the spin-liquid candidate $\kappa-$(BEDT$-$TTF)$_2$Cu$_2$(CN)$_3$", Physical Review Letters **104**, 016403 (2010).

[56] R. S. Manna, S. Hartmann, E. Gati, J. A. Schlueter, M. De Souza, and M. Lang, "Low-temperature lattice effects in the spin-liquid candidate κ-(BEDT-TTF)$_2$Cu$_2$(CN)$_3$", Crystals **8**, 87 (2018).

[57] A. Pustogow, "Thirty-year anniversary of κ-(BEDT-TTF)$_2$Cu$_2$(CN)$_3$: reconciling the spin gap in a spin-liquid candidate", Solids **3**, 93–110 (2022).

[58] E. Gati, J. K. Fischer, P. Lunkenheimer, D. Zielke, S. Köhler, F. Kolb, H. A. K. Von Nidda, S. M. Winter, H. Schubert, J. A. Schlueter, H. O. Jeschke, R. Valentí, and M. Lang, "Evidence for Electronically Driven Ferroelectricity in a Strongly Correlated Dimerized BEDT-TTF Molecular Conductor", Physical Review Letters **120**, 247601 (2018).

[59] T. Komatsu, N. Matsukawa, T. Inoue, and G. Saito, "Realization of superconductivity at ambient pressure by band-filling control in κ-(BEDT-TTF)$_2$Cu$_2$(CN)$_3$", Journal of the Physical Society of Japan **65**, 1340–1354 (1996).

[60] U. Geiser, H. H. Wang, K. D. Carlson, J. M. Williams, H. A. J. Charlier, J. E. Heindl, G. A. Yaconi, B. J. Love, and M. W. Lathrop, "Superconductivity at 2.8 k and 1.5 kbar in κ-(BEDT-TTF)$_2$Cu$_2$(CN)$_3$: the first organic superconductor containing a polymeric copper cyanide anion", Inorganic Chemistry **30**, 2586–2588 (1991).

[61] Y. Saito, A. Löhle, A. Kawamoto, A. Pustogow, and M. Dressel, "Pressure-tuned superconducting dome in chemically-substituted κ-(BEDT-TTF)$_2$Cu$_2$(CN)$_3$", Crystals **11**, 1–10 (2021).

[62] N. Hassan, S. Cunningham, M. Mourigal, E. I. Zhilyaeva, S. A. Torunova, R. N. Lyubovskaya, J. A. Schlueter, and N. Drichko, "Evidence for a quantum dipole liquid state in an organic quasi-two-dimensional material", Science **360**, 1101–1104 (2018).

[63] C. P. Slichter, *Principles of Magnetic Resonance* (Springer, Berlin, Germany, 1989).

[64] M. H. Levit, *Spin Dynamics - Basics of Nuclear Magnetic Resonance* (John Wiley & Sons, Ltd, 2008).

[65] K. Miyagawa, A. Kawamoto, Y. Nakazawa, and K. Kanoda, "Antiferromagnetic ordering and spin structure in the organic conductor, κ-(BEDT-TTF)$_2$Cu[N(CN)$_2$]Cl", Physical Review Letters **75**, 1174–1177 (1995).

[66] H. Seo, "Charge Ordering in Organic ET Compounds", Journal of the Physical Society of Japan **69**, 805–820 (2000).

[67] Y. Shimizu, T. Hiramatsu, M. Maesato, A. Otsuka, H. Yamochi, A. Ono, M. Itoh, M. Yoshida, M. Takigawa, Y. Yoshida, and G. Saito, "Pressure-tuned exchange coupling of a quantum spin liquid in the molecular triangular lattice κ-$(ET)_2Ag_2(CN)_3$", Phys. Rev. Lett. **117**, 6 (2016).

[68] M. Poirier, S. Parent, A. Côté, K. Miyagawa, K. Kanoda, and Y. Shimizu, "Magnetodielectric effects and spin-charge coupling in the spin-liquid candidate κ-(BEDT-TTF)$_2$Cu$_2$(CN)$_3$", Physical Review B - Condensed Matter and Materials Physics **85**, 1–8 (2012).

[69] F. L. Pratt, P. J. Baker, S. J. Blundell, T. Lancaster, S. Ohira-Kawamura, C. Baines, Y. Shimizu, K. Kanoda, I. Watanabe, and G. Saito, "Magnetic and non-magnetic phases of a quantum spin liquid", Nature **471**, 612–616 (2011).

[70] T. Isono, S. Sugiura, T. Terashima, K. Miyagawa, K. Kanoda, and S. Uji, "Spin-lattice decoupling in a triangular-lattice quantum spin liquid", Nature Communications **9**, 1509 (2018).

[71] B. J. Suh, P. C. Hammel, M. Hücker, B. Büchner, U. Ammerahl, and A. Revcolevschi, "Spin dynamics in the low-temperature tetragonal phase of $\cong \frac{1}{8}$ doped single crystal $La_{1.67}Eu_{0.2}Sr_{0.13}CuO_4$", Physical Review B **61**, R9265–R9268 (2000).

[72] M. Klanjšek, A. Zorko, R. Žitko, J. Mravlje, Z. Jagličić, P. K. Biswas, P. Prelovšek, D. Mihailovic, and D. Arčon, "A high-temperature quantum spin liquid with polaron spins", Nature Physics **13**, 1130–1134 (2017).

[73] F. Hammerath, R. Sarkar, S. Kamusella, C. Baines, H.-H. Klauss, T. Dey, A. Maljuk, S. Gaß, A. U. B. Wolter, H.-J. Grafe, S. Wurmehl, and B. Büchner, "Diluted paramagnetic impurities in nonmagnetic Ba_2YIrO_6", Physical Review B **96**, 165108 (2017).

[74] R. Świetlik, B. Barszcz, A. Pustogow, and M. Dressel, "Raman spectroscopy evidence of domain walls in the organic electronic ferroelectrics $(TMTTF)_2X\,(X = SbF_6, AsF_6, PF_6)$", Physical Review B **95**, 085205 (2017).

[75] M. Dressel, P. Lazić, A. Pustogow, E. Zhukova, B. Gorshunov, J. A. Schlueter, O. Milat, B. Gumhalter, and S. Tomić, "Lattice vibrations of the charge-transfer salt $\kappa-$(BEDT-TTF)$_2$Cu$_2$(CN)$_3$: comprehensive explanation of the electrodynamic response in a spin-liquid compound", Physical Review B **93**, 081201 (2016).

[76] M. Pinterić, D. Rivas Góngora, Ž. Rapljenović, T. Ivek, M. Čulo, B. Korin-Hamzić, O. Milat, B. Gumhalter, P. Lazić, M. Sanz Alonso, W. Li, A. Pustogow, G. Gorgen Lesseux, M. Dressel, and S. Tomić, "Electrodynamics in Organic Dimer Insulators Close to Mott Critical Point", Crystals **8**, 190 (2018).

[77] K. G. Padmalekha, M. Blankenhorn, T. Ivek, L. Bogani, J. A. Schlueter, and M. Dressel, "ESR studies on the spin-liquid candidate κ-(BEDT-TTF)$_2$Cu$_2$(CN)$_3$: Anomalous response below T=8K", Physica B: Condensed Matter, Special Issue on Electronic Crystals (ECRYS-2014) **460**, 211–213 (2015).

[78] A. C. Jacko, E. P. Kenny, and B. J. Powell, "Interplay of dipoles and spins in κ-(BEDT-TTF)$_2$X, where X=Hg(SCN)$_2$Cl, Hg(SCN)$_2$Br, Cu[N(CN)$_2$]Cl, Cu[N(CN)$_2$]Br, and Ag$_2$(CN)$_3$", Physical Review B **101**, 1–10 (2020).

[79] S. V. Konovalikhin, G. V. Shilov, O. A. D'yachenko, M. Z. Aldoshina, R. N. Lyubovskaya, and R. B. Lyubovskii, "Crystal structures of the organic metals (ET)$_2$[Hg(SCN)Cl$_2$] and (ET)$_2$[Hg(SCN)$_2$Br]", Bulletin of the Russian Academy of Sciences, Division of chemical science **41**, 1819–1826 (1992).

[80] M. Sawada, S. Fukuoka, and A. Kawamoto, "Coupling of molecular motion and electronic state in the organic molecular dimer mott insulator β'-(BEDT-TTF)$_2$ICl$_2$", Physical Review B **97**, 045136 (2018).

[81] P. C. W. Leung, T. J. Emge, M. A. Beno, H. H. Wang, J. M. Williams, V. Petricek, and P. Coppens, "Novel structural modulation in the first ambient-pressure sulfur-based organic superconductor (BEDT-TTF)$_2$I$_3$", Journal of the American Chemical Society **106**, 7644–7646 (1984).

[82] A. J. Schultz, H. H. Wang, J. M. Williams, and A. Filhol, "Effect of structural disorder on organic superconductors: a neutron diffraction body of "high-T_c" β^*-(BEDT-TTF)$_2$I$_3$ at 4.5 k and 1.5 kbar", Journal of the American Chemical Society **108**, 7853–7855 (1986).

[83] A. Pustogow, A. S. McLeod, Y. Saito, D. N. Basov, and M. Dressel, "Internal strain tunes electronic correlations on the nanoscale", Science Advances **4**, eaau9123 (2018).

[84] T. Yamamoto, M. Uruichi, K. Yamamoto, K. Yakushi, A. Kawamoto, and H. Taniguchi, "Examination of the Charge-Sensitive Vibrational Modes in Bis(ethylenedithio)tetrathiafulvalene", The Journal of Physical Chemistry B **109**, 15226–15235 (2005).

[85] M. E. Fisher, "Relation between the specific heat and susceptibility of an antiferromagnet", The Philosophical Magazine: A Journal of Theoretical Experimental and Applied Physics **7**, 1731–1743 (1962).

[86] Y. Saito and A. Kawamoto, "Determination of the hyperfine coupling tensor in organic conductors κ-(BEDT-TTF)$_2X$ (X=Cu[N(CN)$_2$]Br, Cu(NCS)$_2$) on central ^{13}C sites", Solid State Nuclear Magnetic Resonance **73**, 22–30 (2016).

[87] D. C. Johnston, "Stretched exponential relaxation arising from a continuous sum of exponential decays", Physical Review B **74**, 184430 (2006).

[88] P. M. Singer, A. Arsenault, T. Imai, and M. Fujita, "^{139}La Nmr investigation of the interplay between lattice, charge, and spin dynamics in the charge-ordered high-T_c cuprate $La_{1.875}Ba_{0.125}CuO_4$", Physical Review B **101**, 174508 (2020).

[89] J. Wang, W. Yuan, P. M. Singer, R. W. Smaha, W. He, J. Wen, Y. S. Lee, and T. Imai, "Emergence of spin singlets with inhomogeneous gaps in the kagome lattice Heisenberg antiferromagnets Zn-barlowite and herbertsmithite", Nature Physics **17**, 1109–1113 (2021).

[90] J. Wang, W. Yuan, T. Imai, P. M. Singer, F. Bahrami, and F. Tafti, "NMR investigation on the honeycomb iridate $Ag_3LiIr_2O_6$", Physical Review B **103**, 214405 (2021).

[91] W. Yuan, J. Wang, P. M. Singer, R. W. Smaha, J. Wen, Y. S. Lee, and T. Imai, "Emergence of the spin polarized domains in the kagome lattice Heisenberg antiferromagnet Zn-barlowite $(Zn_{0.95}Cu_{0.05})Cu_3(OD)_6FBr$", npj Quantum Materials **7**, 1–10 (2022).

[92] T. Kobayashi, Q.-P. Ding, H. Taniguchi, K. Satoh, A. Kawamoto, and Y. Furukawa, "Charge disproportionation in the spin-liquid candidate $\kappa - (ET)_2Cu_2(CN)_3$ at 6 K revealed by ^{63}Cu NQR measurements", Physical Review Research **2**, 042023 (2020).

[93] J. P. Butler, J. A. Reeds, and S. V. Dawson, "Estimating Solutions of First Kind Integral Equations with Nonnegative Constraints and Optimal Smoothing", SIAM Journal on Numerical Analysis **18**, 381–397 (1981).

[94] L. Venkataramanan, Y.-Q. Song, and M. Hurlimann, "Solving Fredholm integrals of the first kind with tensor product structure in 2 and 2.5 dimensions", IEEE Transactions on Signal Processing **50**, 1017–1026 (2002).